2019

Study of phase transformations in γ-based Ti-Al alloys by advanced in-situ diffraction techniques

Xi Li
University of Wollongong

UNIVERSITY OF WOLLONGONG AUSTRALIA

Study of phase transformations in γ-based Ti-Al alloys by advanced *in-situ* diffraction techniques

Xi Li

Supervisors:

Rian Dippenaar, Klaus-Dieter Liss, Mark Reid

This thesis is presented as part of the requirement for the conferral of the degree of Doctor Philosophy

University of Wollongong
School of Mechanical, Materials, Mechatronic and Biomedical Engineering
Faculty of Engineering & Information Sciences

Mar 2019

Abstract

Due to its low specific mass and high strength at high temperature, γ-based Ti-Al alloys are candidate materials for use in aerospace industries. Due to its simple structure, poly-synthetically twinned (PST) Ti-Al alloys are excellent candidates for in-depth studies. The superior properties of Ti-Al alloys render them more suitable for applications in the automobile and aerospace industries compared to conventional Ni based super-alloys. The potential of using these alloys for the manufacture and application of dedicated and advanced components in these industries provided the driving force for the present study.

Although advanced PST alloys have attracted significant attention in recent times, a comprehensive understanding of the microstructural evolution of these alloys is still in its infancy and it is fundamentally important to bridge the gap between microstructural development and mechanical performance. Here, we performed a thorough study of the microstructure and crystallography of a Ti-47.5Al (at. %) PST alloy by a combination of Electron Backscatter Diffraction, *in-situ* neutron diffraction and high-temperature laser-scanning confocal microscopy during heating cycles. It was found that Σ-3 <111> twins of the γ-phase are unlikely to form along the growth direction of a lath. The observable γ-crystal orientations (variants) along the lath belong to the same twin family and are related to each other by a 120° rotation along the <111> direction. Short-range-order structures persist in the disordered α-phase matrix at high temperature; it transforms to form a fully lamellar structure following appropriate heating treatment.

Knowledge of the key transition temperatures of γ-based Ti-Al alloys is a necessary pre-requisite for the design of heat treatments that would achieve the required mechanical properties if these alloys are to be employed in the automobile and areospace industries. For

the first time, a newly developed technique by which laser-scanning confocal microscopy is combined with *in-situ* differential thermal analysis was used to determine the pertaining phase transition temperatures in these Ti-Al alloys, while at the same time, nucleation and growth events could be observed. Different cooling rates were used to study the nucleation and grain growth kinetics and it was possible to predict the equilibrium α-transus temperature of Ti-45Al-7.5Nb-0.5C (at. %) alloy.

Lattice strain evolution during deformation in Ti-Al alloys at high temperature is critical with respect to its microstructural evolution and microstructural stability. It is shown here that careful evaluation of lattice parameters is important to a more comprehensive understanding of thermal expansion, crystallographic order and changes in chemical composition in response to applied pressure. The lattice parameters of Ti-45Al-7.5Nb-0.25/0.5C (at. %) alloys were calculated by using both Rietveld and single peak fitting methods from data obtained by *in-situ* synchrotron diffraction experiments at high temperature under atmospheric and high pressure, respectively. The lattice strain evolution as a function of temperature in a Ti-45Al-7.5Nb-0.25C (at. %) alloy under high hydrostatic pressure was compared to that of a Ti-45Al-7.5Nb-0.5C (at. %) alloy upon heating under atmospheric pressure. The contribution of each of the four lattice strain factors has semi-quantitatively been decomposed in the temperature range investigated and representative values of the respective strain contributions have been tabulated for the first time for the alloys investigated.

Intermetallic γ-based titanium aluminides of Ti-45Al-7.5Nb (at. %) have been subjected to high-pressure torsion processing and significant grain refinement was obtained by this experimental technique. These ultrafine-grained materials led to enhanced strength and ductility. Complimentary studies have been conducted in order to correlate microstructure,

phase transformation behavior and enhancement of mechanical properties. Neutron and X-ray diffraction studies revealed that order-disorder transformations occur during high-pressure torsion processing. Moreover, it has been demonstrated that there is a significant difference in behavior between the surface and median layers in a thin disk-shaped specimen. While the γ-phase essentially disappears in the surface region in the course of high-pressure torsion processing, the extent of this order/disorder phase transition decreases towards the median area of the thin disk. The low bulk texture index determined experimentally, is consistent with grain rolling and swirling rather than deformation by slip. Vickers micro-hardness indentations on the surface of the disk have shown that the hardness increased from 308 H_v to 605 H_v as a result of the application of high-pressure torsion. Moreover, large residual stresses, approaching the yield limit, develop between different regions of the specimen. For the first time, the present research demonstrates heterogeneity in structural transformation, such as displacive transformations and order/disorder transformations, which can possibly explain earlier reported inhomogeneities in mechanical properties and microstructure.

In summary, the phase transition temperatures and phase transformations of γ-based Ti-Al alloys are significantly altered under extreme processing conditions, such as high temperature, high pressure and severe plastic deformation.

Acknowledgements

I would not have been able to complete my thesis without the contributions and help from the following individuals and institutes.

First of all I want to express my sincere thanks to my supervisors, Prof Rian Dippenaar, Prof Klaus-Dieter Liss and Dr Mark Reid for their great guidance, continuous support and great encouragement in my PhD journey. I wish to thank my principal supervisor Prof Rian Dippenaar. I shall never forget how he comforted me and gave me suggestions when I was confronted with many difficulties and thought I would have to give up my studies in the first year of my PhD life. I also remembered deeply in my heart that he encouraged me and tried his best to comfort and encourage me when I became a new mum and needed to balance my PhD study and my life. It is him that told me that the life always comes first and tried to relax me. Prof Klaus-Dieter Liss gave me advice as well as wonderful and excellent time not only with respect to reciprocal spacing in diffraction, but also in the real life adventure. It is him that taught me how to drive an off-road vehicle. The 10 min running from Stanwell top to Stanwell Park, 4 hours hot car travelling from Wagga-Wagga to Wollongong, the beach viewing at Stanwell Park and the bush walking at ANSTO are all very impressive in my memories. Moreover, the coffee time and the discussions about academic matters with him are what I miss most.

I should like to acknowledge the Chinese Scholarship Council (CSC) for providing me a CSC scholarship and ANSTO for a top-up of my scholarship for my living expenses in the course of my PhD studies. I should also like to acknowledge the University of Wollongong for offering me an International Postgraduate Tuition Award (IPTA) and a matching scholarship

to cover my tuition during my PhD study as well as the support for living expenses in the last half year of my PhD.

I should like to express my appreciation to my collaborators and the professional staff that assisted me. Specifically, Dr Dhriti Bhattacharyya (ANSTO); Associate Prof Megumi Kawasaki and Mr Han, Jae-Kyung (Oregon State University); Dr Dominic Phelan (UOW); Dr Suk-Chun Moon(UOW); Prof Rui Yang and Mr Hao Jin (Institute of Metal Research, CAS, China); Mr Matthew Franklin and Mr Nick Mackie (UOW); who all provided important academic and technical assistance to me.

I also thank the administrative support staff, especially in the Faculty of Engineering and Information Sciences, Ms Rhondalee Cambareri (Research Manager) and Ms Julia Johnson (Research Administration Officer) for their kind assistance.

I especially wish to acknowledge help from Prof Garry McIntyre (Research Leader), at ANSTO during my PhD study and I wish to thank him.

Furthermore, I would like to thank my teammates and colleagues during my PhD study at UOW and ANSTO. I would like to express my appreciation to Dr Nageshwar Rao Yepuri, Ms Monika Wyszomirska, Ms Lisa Thoennessen, Mr Pragathi Dissanayaka, Mr Ali Hammadi, Mr Navjeet Singh and Mr Dasith Dodangoda Liyanage for their care and help during these four years.

I would like to thank my close friends, Dr Qiannan Liu, Mr Huzhe, Ms Weiping Hu, Dr Lin Li, and my relatives for their kind help and support. It is them that helped me a lot when I met difficulties abroad.

Last but not the least, I would like to express my special thanks to my family, especially my husband, Dr Xiaoming Yuan, who helped me to revise the drafts of my publications several times and encouraged me whenever I felt that it became impossible for me. I owe special thanks to my mother-in-law, who spent most of her time to care and accompany my daughter when I had limited time because of PhD study; and my precious little princess, Yiyi Yuan, who grows up and smiles. She is my sunshine all the time.

Certification

I, Xi Li, declare that this thesis submitted in fulfilment of the requirements for the conferral of the degree of Doctor of Philosophy, from the University of Wollongong, is wholly my own work unless otherwise referenced or acknowledged. This document has not been submitted for qualifications at any other academic institution.

_____

Xi Li

Mar 2019

Lists of Nomenclature

List of Abbreviations and Symbols

Abbreviations and symbols	Name
α	Alpha phase, disordered, hexagonal structure in Ti_3Al
α_2	Alpha2 phase, ordered, hexagonal structure in Ti_3Al
Al	Aluminium
Å	Angstrom units
at. %	Atom percent
β	Beta phase, disordered, body-centered cubic A2 structure in Ti
β_o	Beta-o phase, ordered, B2 structure
^oC	Degree Celsius
C	Carbon
DSC	Differential scanning calorimetry
EDX	Energy dispersive X-ray spectroscopy
EDM	Electrical Discharge Machining
γ	Gamma phase, face-centered tetragonal structure in TiAl
GPa	The unit of pressure, gigapascal

H_V	Unit of hardness, as the Vickers Pyramid Number
HEXRD	High energy X-ray diffraction
HIP	Hot isostatic pressing
HPT	High pressure torsion
HTLSCM	High temperature laser scanning confocal microscopy
K	Kelvin
λ	Wavelength
Mo	Molybdenum
min	Minute
mm	Millimeter
μm	Mircrometer
Nb	Niobium
N	Newton
PST	Polysynthetic twinned crystals
ϕ	Innermost sample rotation angle of four-circle
χ	Tilt angle of four-circle
η	Angle along diffraction ring
ω	Outermost four-circle sample orientation angle

rpm	Revolutions per minute
Q	Reciprocal lattice vector
SEM	Scanning electron microscopy
Ti	Titanium
Ti-Al	Titanium aluminides
2θ	The scattering angle
$\mathbf{T_{\gamma,solv}}$	Alpha transus temperature, equilibrium temperature between the (α + γ) and α- phase fields
$\mathbf{T_{eu}}$	Eutectoid temperature, the point where α phase transforms into the (α_2 + γ phases)
TNM	Ti-Al alloys containing Mo, which solidify via the β-phase and have a homogenous microstructure, lamellar γ/α_2-colonies and globular γ and β/β_o-grains
TNB	Ti-Al alloys containing Nb
TEM	Transmission electron microscopy

List of Organizations

Abbreviation	Full Name
CSC	Chinese Scholarship Council
ANSTO	Australian Nuclear Science and Technology Organisation
UOW	University of Wollongong
ESRF	European Synchrotron Radiation Facility
J-PARC	Japan Proton Accelerator Research Complex

Table of Contents

List of Figures

List of Tables

Chapter 1. Introduction

1.1 Background

It has been reported [1, 2] that γ-based Ti-Al alloys are more suitable materials for applications in the aerospace industry than conventional Ni based super-alloys, due to their low specific weight and high strength at elevated temperatures, thus providing superior fuel efficiencies. Worldwide research focus is given to the study of phase transformations and mechanical properties, with the aim of developing alloys for withstanding high-temperature creep and to make materials forgeable under near-conventional conditions. Most recently, *Rolls-Royce*, *General Electric* (GEnxTM engine) and *Pratt* & *Whitney* (P & W) have employed γ-based Ti-Al alloys as turbine blade materials in their aircraft engines [3]. In order to push for higher operating temperatures, longer operation times and simplified manufacturing processes, more advanced alloys have to be developed and their behavior understood under extreme conditions [4]. While high-pressure components play a major role in manufacturing, the in-situ evolution of the phase transformations, lattice parameter changes and microstructure of these alloys under extreme manufacturing and operating conditions are not well understood.

The microstructure, texture, phase composition and phase distribution in these Ti-Al alloys largely determine the mechanical properties. Most investigations have been limited to the use of traditional characterization techniques, such as X-ray diffraction (XRD), scanning electron microscopy (SEM) and transmission electron microscopy (TEM) [5, 6]. Recently, Liss *et al.* [2, 7-9] developed several *in-situ* characterization methods to study titanium aluminides in-situ, in real time and under extreme conditions, including plastic deformation at high temperature, equation of state under high pressure, lattice evolution and atomic order. In

particular, high energy X-ray and neutron diffraction deliver fully complementary information. In the case of neutrons, due to the opposite scattering contrasts, Ti has a negative scattering length, Al a positive scattering length, neutrons are sensitive to the study of the order parameter. X-rays on the other hand provide more conventional information such as texture and grain size effects though are much less sensitive to order/disorder effects. Order/disorder phase transformations play a key role in the mechanical stability and plastic deformation of titanium aluminides and hence triggered the design of the present study. More specifically, advanced diffraction methods, such as neutron and high-energy X-ray diffraction, have been used in this study in order to capitalize on the high penetration and time efficiency of these techniques in addition to the *in-situ* high temperature and high pressure capabilities that have recently been developed.

1.2 Objectives

The principal aims of the present project were to contribute to a better understanding of the microstructural evolution of selected titanium aluminides with a view to their behavior during advanced and extreme manufacturing processes. The scientific aims were to study experimentally, the evolution and structural changes of the selected Ti-Al intermetallics under extreme manufacturing and operating conditions, such as high-temperature, high-pressure and severe plastic deformation.

The specific objectives are:

1. To investigate phase transformations

2. To study microstructural evolution

3. To elucidate order-disorder transitions

4. To study the texture of deformed γ-based Ti-Al alloys

5. To correlate micro-structural with crystallographic/atomic structural evolution

6. To quantify long and short-range order and its stability

1.3 Thesis outline

The scope of this doctoral work is briefly summarized in Figure 1.1. Following the literature review and a description of the experimental procedures, the PhD thesis is divided into four parts: microstructural changes in single crystals of selected γ-based Ti-Al alloys during heating under atmospheric pressure; microstructural changes in the polycrystalline form thereof during heating under atmospheric pressure; upon heating at high pressure; and upon severe plastic deformation during high-pressure torsion.

The following detailed investigations were conducted:

(1) Investigation of order-disorder transformations in poly-synthetically twinned (PST) crystals as a function of temperature. In order to elucidate short-range-order in the α-phase, we study diffuse scattering of PST crystals. In an attempt to better understand the development of the lamellar structure, its microstructural evolution during heat treatment was characterized and recorded by the use of neutron-diffraction techniques and high-temperature laser-scanning confocal microscopy.

(2) Investigation of microstructural changes in selected Ti-Al polycrystalline alloys as a function of temperature, in addition to measuring the exact phase transformation temperatures under equilibrium conditions.

(3) Prior to commencing the present investigation, Liss *et al.* [2] conducted *in-situ* high-pressure studies on the alloys of concern in the present study. In addition Yeoh *et al.* studied

the microstructural response of a similar alloy under atmospheric pressure as a function of temperature [10]. The first step in the present investigation was to re-visit their experimental data and extract quantitatively (which they had not done), the lattice parameter evolution upon gradual heating, under ambient and 9.6 GPa high-pressure conditions respectively. For the first time, lattice strain evolution is separated into contributions from thermal expansion, atomic order, composition and hydrostatic pressure. Not only does lattice strain lead to inter-granular stresses but it also allows for the identification of phase transformations and an assessment of changes in the pertaining phase diagrams upon the application of high pressure.

(4) The phase distribution and the extent of order-disorder phase transformations have been determined of a selected titanium aluminide that has been subjected to high-pressure torsion. Upon the application of high-pressure torsion, the grain structure is observed by optical microscopy and deducted by the diffraction results. In order to investigate the mechanisms of plasticity under the influence of severe plastic deformation as imposed by high-pressure torsion, crystallographic texture was measured experimentally.

In summary, an assessment is made of the necessary developments that are required to develop γ-based Ti-Al alloys for advanced aerospace applications.

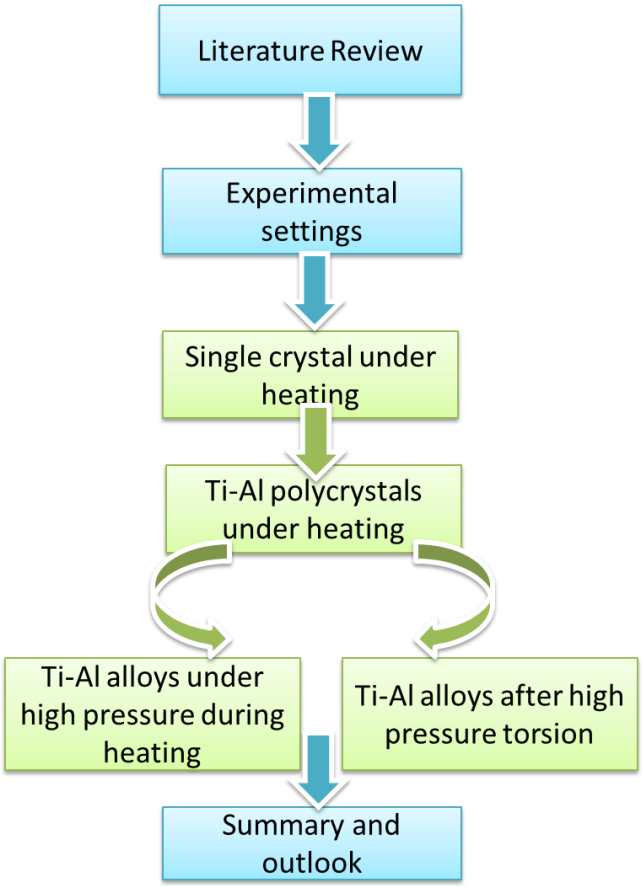

Figure 1.1 The flowchart of the thesis outline.

1.4 Reference

[1] F. Appel, J.D.H. Paul, M. Oehring, Gamma titanium aluminide alloys: science and technology, John Wiley & Sons, 2011.

[2] K.-D. Liss, K.-I. Funakoshi, R. Dippenaar, Y. Higo, A. Shiro, M. Reid, H. Suzuki, T. Shobu, K. Akita, Metals, vol. 6, pp.165, 2016.

[3] B.P. Bewlay, S. Nag, A. Suzuki, M.J. Weimer, Materials at High Temperatures, vol. 33 ,pp. 549-559, 2016.

[4] R.D. Flack, Fundamentals of jet propulsion with applications, Cambridge University Press, 2005.

[5] H.F. Chladil, H. Clemens, H. Leitner, A. Bartels, R. Gerling, W.T. Marketz, Advanced Engineering Materials, vol. 7, pp. 1131-1134, 2005.

[6] H. Chladil, H. Clemens, H. Leitner, A. Bartels, R. Gerling, F.-P. Schimansky, S. Kremmer, Intermetallics, vol. 14, pp. 1194-1198, 2006.

[7] K.-D. Liss, T. Schmoelzer, K. Yan, M. Reid, M. Peel, R. Dippenaar, H. Clemens, Journal of Applied Physics, vol. 106, pp. 113526, 2009.

[8] K.-D. Liss, A. Stark, A. Bartels, H. Clemens, T. Buslaps, D. Phelan, L.A. Yeoh, Advanced Engineering Materials, vol. 10, 2008

[9] K.-D. Liss, A. Bartels, H. Clemens, S. Bystrzanowski, A. Stark, T. Buslaps, F.-P. Schimansky, R. Gerling, C. Scheu, A. Schreyer, Acta Materialia, vol. 54, pp. 3721-3735, 2006

[10] L. A. Yeoh, K.-D. Liss, A. Bartels, H. Chladil, M. Avdeev, H. Clemens, et al., Scripta Materialia, vol. 57, pp. 1145-1148, 2007.

Chapter 2. Literature review

Titanium aluminides (Ti-Al) alloys have excellent mechanical properties, such as high strength, low density and good corrosion resistance. Selected titanium aluminides have been developed for applications in the aerospace industry in preference to conventional Ni-based alloys in order to reduce mass and thus gain fuel efficiencies. The γ-based Ti-Al alloys are all based on the intermetallic γ-TiAl phase in contrast to other Ti and Al intermetallic structures, usually in coexistence with a small amount of α_2-Ti_3Al or another minority phases. They are widely used for turbine engine manufacturing due to their attractive mechanic properties at high temperature [1-5]. The composition range and related phase relationships are shown in Figure 2.1 [6]. In the last decade, numerous efforts have been made by companies such as the *General Electric Company* (GE), *Rolls-Royce* and *Pratt* & *Whitney* (P & W) to further improve the properties of γ-based Ti-Al alloys so that they can effectively be utilized in the engineering market. However, processing of these alloys remains difficult owning to their poor formability [7]. It has been shown that additions of niobium (Nb) to these alloys can stabilize the highly isotropic β-phase, thus partially decreasing the difficulties encountered in the processing of these alloys [8, 9]. In addition niobium also improves the strength of γ-based Ti-Al alloys [10]. Therefore, the Ti-Al-Nb γ-based alloys pose great potential in engineering applications and have attracted a lot of interest. Polysynthetic twinned (PST) crystals of Ti-47.5Al (at. %), were selected for further study since it has one of the simplest microstructures of γ-based Ti-Al alloys, namely the lamellar, and diffractograms align as in a single crystal. Following information obtained on the microstructural evolution of this alloy, attention was given to a study of selected polycrystalline Ti-Al alloys in order to establish the link between mechanical properties and microstructure.

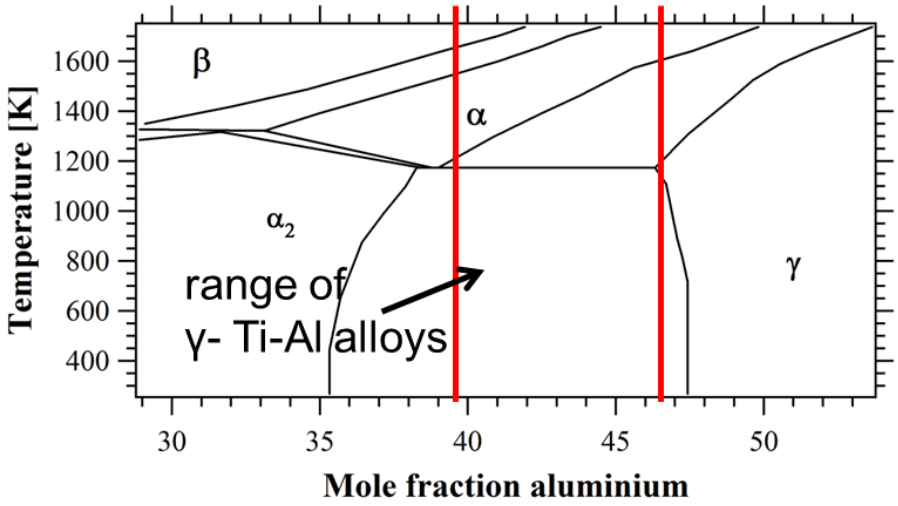

Figure 2.1 The composition range of the γ-based Ti-Al alloys [6].

The α (α_2)-, β (β_o)- and γ- phases are the possible phases present in engineering γ-based alloys during heat treatment and their crystal structures will be discussed in more detail in section 2.1.1. There are four major microstructures present in these alloys namely near-γ structure, duplex structure, nearly lamellar structure, and fully lamellar structure (for details see section 2.1.2). The microstructure of PST crystals consists of a fully lamellar colony and Ti-45Al-Nb alloys may have a near-lamellar structure.

There are contradictions between the phase diagrams of Ti-Al reported by Schuster and Palm [11] and Witusiewicz *et al.* [12]. Furthermore, with different niobium contents and different measuring methods, the versions of phase diagram for Ti-Al-Nb vary significantly. More detail is provided in section 2.1.3. However, it is necessary to determine with certainty, the exact Ti-Al-Nb phase diagram as a necessary pre-requisite for the design of γ-based Ti-Al alloys. Therefore, an attempt has been made in this thesis to provide experimental data to enable a partial reconstruction of the Ti-Al-Nb phase diagram. In addition, the crystallographic structure, the microstructure and phase evolution during heat treatment are important factors influencing the mechanical properties of γ-based Ti-Al alloys. Therefore,

the mechanical properties, such as hardness, yield strength, tensile strength and ductility of γ-based Ti-Al alloys are reviewed in section 2.1.4.

Neutron diffraction and *in-situ* X-ray diffraction, described in section 2.2, were the main experimental techniques used to study the Ti-Al alloys in this project. This is due to conventional microscopic methods having limitations for the characterization of γ-based Ti-Al alloys. For example, the spacing between the laths of the lamellar structure of Ti-Al alloys cannot be resolved in an optical microscope or even in a SEM since the inter-lamellar spacing can be as little as 10 nm after high pressure. Although it is possible to study the lamellar structure by TEM, it is difficult to obtain a representative sample. Traditional X-ray diffraction techniques have the advantage that grain size and phase fractions of Ti-Al alloys can be determined [13], but the drawback is that this kind of post mortem analysis does not provide information of the rate and mechanism of the pertaining phase changes at high temperature.

For these reasons, *in-situ* X-ray diffraction was conducted in the course of heating cycles [14, 15]. However, there are impediments to the use of conventional *in-situ* X-ray diffractometry. Due to the low penetrating power of conventional X-rays, they are sensitive to surface effects. For example, there is a possibility that the surface of a specimen can be depleted of aluminium at high temperature through vaporization or oxidation, and hence the phase fraction would not be representative of the bulk material. For this reason, *in-situ* X-ray diffraction was conducted in a synchrotron since the great attenuation length of the high-energy X-rays provides information from the bulk of the material (The attenuation length is defined as the distance into the material when the probability has dropped to 1/e that the beam particle has not been absorbed.). However as noted previously, X-rays are much less sensitive to the distinction between ordered and disordered phases, while neutron diffraction

is very responsive to it. Thus the two techniques were used to provide complimentary information.

2.1 γ-based Ti-Al alloys

Intermetallic γ-based Ti-Al alloys are widely applied in the automotive and aerospace industries due to their high strength at elevated temperatures, low density, good corrosion resistance and high melting point [16-18]. They are suitable for aerospace-components such as turbine blades in jet engines and turbocharger turbine wheels [19, 20]. With the increasing demand on engine efficiencies, new processing routes including casting, forging, compression and heat treatments need to be designed for these alloys [21, 22]. The final mechanical properties of the required products can be achieved by controlling the microstructure of γ-based Ti-Al alloys during processing. In order to simplify the initial analysis, PST crystals with a nominal composition of Ti-47.5Al were used, because it exhibits most of the desired properties of γ-based Ti-Al and it has a much simpler microstructure, consisting of a single lamellar colony which is produced using a direct solidification technique [23-25]. By arranging the alignment of the lamellae, superior elongation is achieved [26, 27] and due to its well defined microstructure it is easier to interpret the pertaining recrystallization and deformation mechanisms [2]. For these reasons, PST crystals have attracted much attention in recent research [23-25, 28] and these results provide an excellent reference base for the present investigation.

Niobium is one of the major β-stabilizing alloying elements [29] and it was once reported that the alloys, containing about 1 at. % Nb and more than 46 at. % Al , are easily processed by rolling and forging because of the presence of body-centered cubic β-phase at hot-working temperatures. However, more recent research has shown that by increasing the niobium content and decreasing the aluminium content leads to an improvement in strength of up to

1 GPa at room temperature [30]. The TiAl alloys with the content of Nb from 5 at. % to 10 at. % are so-called TNB alloys, which solidify via the β-phase. Following solidification, TNB alloys have a homogenous microstructure consisting of lamellar ($\gamma + \alpha_2$)-colonies and a globular γ-phase. Appel and coworkers [2] produced Ti-46Al-9Nb sheet material with increased strength and creep resistance, based on a powder metallurgy technique [31]. Further study [32] shows the mechanical anisotropy of the Ti-46Al-9Nb sheets perpendicular to and along the rolling direction is very low for material processed from room temperature to 1273 K, compared to Ti-47Al-4Nb sheets produced via the same technique. It is important to note that small additions of carbon (C) can result in further strengthening of Ti-Al alloys [33-35]. Therefore, Ti-45Al-7.5Nb-(0.25/0.5)C alloys processed by powder metallurgic techniques and hot-rolling have been used in this study.

2.1.1 Crystallography

The γ-based Ti-Al alloys, which contain large fractions of the γ-phase, have attracted more attention for engineering applications. Their microstructure is comprised of a lamellar structure consisting of α_2-Ti_3Al and γ-TiAl phases, with the space group of P 6_3/m m c and P 4/m m m, respectively.

Processing of this type of alloy in the ($\alpha_2/\alpha + \gamma$) phase-field remains a challenge due to crystalline anisotropy and the presence of covalent bond. Appel *et al*. [16] pointed out that: "The important difference with alloys that solidify completely through β and that subsequently precipitate α on further cooling, is that the α that forms from the β can do so with up to 12 different orientation variants". Thus, a large β grain with *bcc* structure, space group I m $\bar{3}$ m can be divided into lamellar colonies with up to 12 different orientations. This effect, termed "crystal partitioning" [36, 37], can therefore lead to significant grain

refinement and reduced texture formation during casting. The cubic β-phase has highly isotropic properties and independent slip systems can operate as experimentally confirmed by Liss *et al.* [38] in their *in-situ* synchrotron X-ray study. The β-solidifying alloys being studied in the present program have a fine and homogenous microstructure and are therefore easier to forge than conventional ($\alpha_2/\alpha + \gamma$) alloys [16, 39, 40]. It is possible to stabilize the β-phase by the addition of selected alloying elements, but it has recently been established that the β-phase can also be physically formed by the application of high hydrostatic pressure at high temperature. This finding opens a window for conventional hot-processing techniques to be utilized to produce these alloys [26, 38, 41]. Therefore, the disordered β-phase with a body-centered cubic structure and its ordered phase β_o, of CsCl structure P m $\bar{3}$ m, have engineering significance.

Crystallographic structures of the α (α_2)-, β (β_o)- and γ- phases, which exist in the γ-based Ti-Al alloys, are shown in Figure 2.2 and listed in Table 2.1.

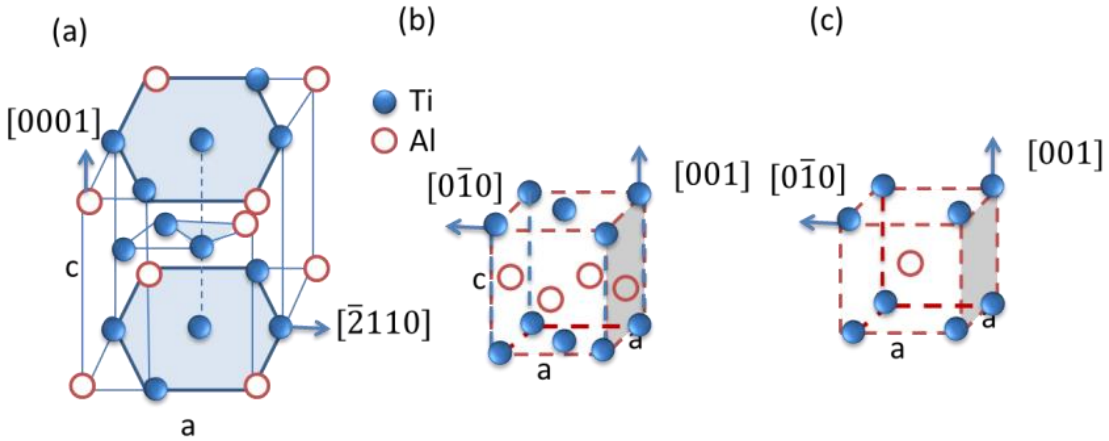

Figure 2.2 Crystal structure (a) Hexagonal α_2-phase (Ti_3Al), (b) Tetragonal γ-phase (TiAl), (c) Cubic β_o-phase [16].

The α_2-phase is an ordered Strukturbericht $D0_{19}$ structure (see Figure 2.2(a)), which is hexagonal close-packed with space group P 6_3 /m m c. It transforms to a disordered

α-structure at temperatures between 1398 and 1423 K [49] of same space group but half the lattice parameter *a*. The notation α_2/α refers to the ensemble of α_2- and α- phases if we do not distinguish there peculiarities, for which we use the larger unit cell of α_2.

The α_2-phase exhibits good strength, but has low ductility and is brittle at high temperature [50, 51]. The ordered phase implies that the aluminium and titanium atoms stay in their respective fixed sites according to the crystallographic structure. For instance, the structure of a fully ordered lattice α_2-Ti_3Al (Figure 2.2(a)) has aluminium atoms occupying 25% of the lattice positions. The disordered phase refers to the case where aluminium and titanium atoms in the crystal lattice randomly interchange sites. For example, titanium atoms have the possibility of residing in red positions (Figure 2.2) and their occupancy probability is just given by the average composition.

Table 2.1 Crystallographic information of phases of the γ-based Ti-Al alloys.

Phase	Space group (number)	Lattice parameter *a* (nm)	Lattice parameter *c* (nm)	Reference
γ-Ti-50Al	P 4/m m m (123)	0.4	0.4075	[42]
		0.4019	0.4065	[17]
		0.4012	0.4065	[43]
		0.402421	0.407335	[44]
		0.39973	0.40809	[45]
		0.39814	0.40803	[46]
		0.401867	0.406542	[17]
α_2 (Ti_3Al)	P 6_3/m m c (194)	0.5782	0.4629	[42]
		0.5764	0.4664	[47]
		0.5775	0.4638	[43]
		0.5768	0.4642	[17]
α_2-Ti-33.3Al		0.57763	0.46348	[48]
α_2		0.57372	0.46825	[46]
α/α_2		0.576803	0.464241	[17]
α_2		0.577568	0.465646	[44]
β	I m $\bar{3}$ m (229)	0.333065		[12]*
β_o	P m $\bar{3}$ m (221)			[12]

*at 1173K

The intermetallic compound γ-phase has an ordered Strukturbericht $L1_0$ structure (see Figure 2.2(b)) with the space group P 4/m m m [52]. It has been reported that *c*/*a* ratio of the *fcc*-based setting at its stoichiometric composition is approximately 1.02 [53]. The lattice parameters *a* and *c* have a linear dependence on titanium concentration and the substitution of titanium away from stoichiometry leads to more tetragonal distortion [54]. The γ-phase remains ordered up to 1723 K on heating and has excellent oxidation resistance. The prototype for the cubic β_o phase (Figure 2.2(c)) is CsCl with Strukturbericht B2 structure. Its Pearson symbol and space group are cP2 and P m $\bar{3}$ m respectively.

2.1.2 Microstructure

2.1.2.1 Microstructures of Ti-Al alloys

Generally, there are four main types of microstructure of γ-based Ti-Al alloys [55, 56], as presented in Figure 2.3.

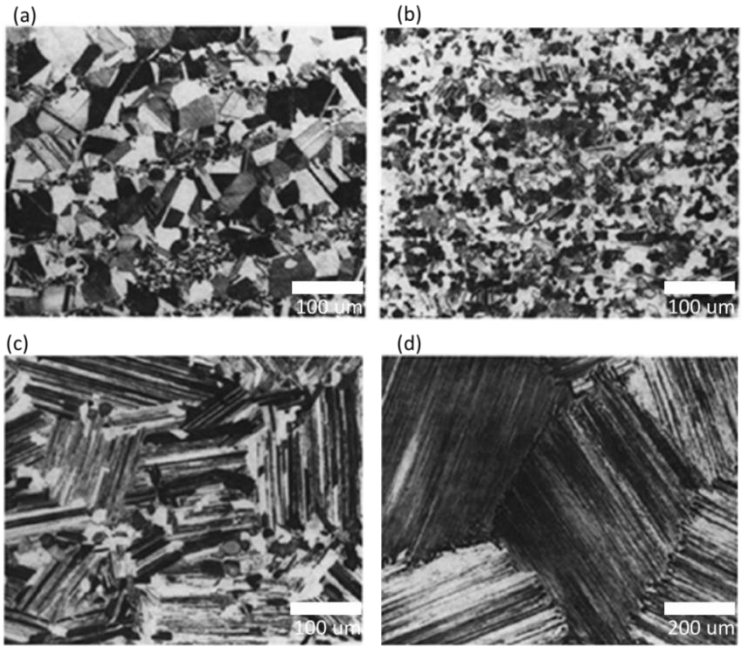

Figure 2.3 Four types of microstructures for the γ-TiAl based alloys after heat treatments, (a) Near-γ structure, (b) Duplex structure, (c) Nearly lamellar structure, and (d) Fully lamellar structure, based on and figures reproduced from [55, 56].

The first type is a near-γ-phase microstructure shown in Figure 2.3(a). These inhomogeneous microstructures consist of the dark, fine γ-phase, bulk γ and a small amount of bright α_2-phase. The second type is a duplex microstructure shown in Figure 2.3(b). The main features are the (α_2 + γ)-lamellar colonies and globular γ-phase. Their respective phase fractions are approximately one half. The third is the near-lamellar microstructure shown in Figure 2.3(c), for example, the microstructure of as-cast Ti-Al alloys usually belongs to this type [57]. The main feature of this type is the lamellar (α_2 + γ) phase and a small fraction of globular/monolithic γ-phase. The last type is the fully lamellar microstructure, which only comprise the (α_2 + γ) lamellar colonies, as shown in Figure 2.3(d).

Different cooling rates lead to different microstructures [57] in the as-cast Ti-Al alloy (near-lamellar structure). A schematic representation of the possible mechanisms of the different structures is shown in Figure 2.4. At very low cooling rates, for instance furnace cooling, it produces a fully lamellar structure, as shown in Figure 2.4(a). In 2009, Gebhard *et al.* have reported the lamellar spacing in Ti-Al alloys decreases with the increase of the cooling rate [58]. However, as far as I know, there is no reported information about the grain size and *in-situ* microstructural evolution at different cooling rates. The highest cooling rates (e.g. ice-water quenching) resulted in near-γ phase microstructures, shown in Figure 2.3(a). During cooling, massive γ-grains nucleate on prior α/α grain boundaries and the α_2-phase is ordered from the prior α-phase. This γ-phase nucleation is referred to as sympathetic nucleation/heterogeneous nucleation. An intermediate cooling rate (by air or cooling in a sand-mould) would produce Widmanstatten laths and feathery structures within lamellar grains, shown in Figure 2.4(b). The packets of lamellar structure with different orientations from the parent lamellar structure, as shown in Figure 2.4(b), are called Widmanstätten laths [59]. The feathery structure looks like an extension of the parent lamellar microstructure and

has less than 15^{o} miss-orientation compared with the surrounding colonies [60]. Higher cooling rates (such as oil or water quenching) produce feathery structures co-existing with γ-massive grains, as shown in Figure 2.4(c). At even higher cooling rates α-quenched material is obtained, or in surface near regions, where the α microstruture is retained, but orders to α_2-phase [53].

It has been reported that lamellar structures are formed by two different mechanisms: (1) formation of γ-lamellae from the disordered α-phase during cooling when the cooling rate is low; and (2) precipitation of ultrafine γ-lamellae within globular α_2-grains during heat treatment [2, 61-63]. *In-situ* synchrotron HEXRD of a Ti-43.5Al-4Nb-1Mo-0.1B alloy shows that the γ-lamellae form during appropriate heat treatments following fast cooling [64].

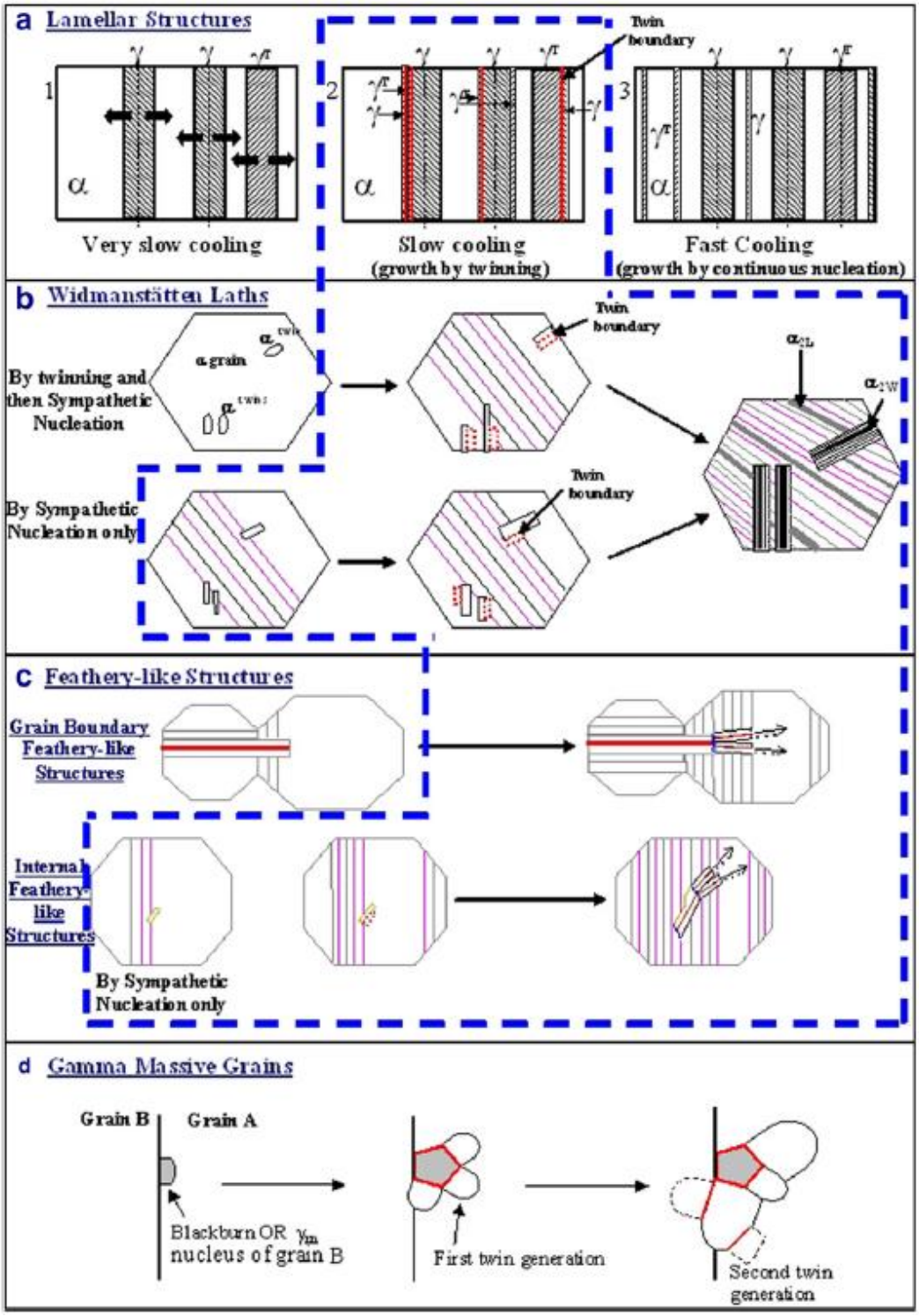

Figure 2.4 Possible mechanisms for microstructural development upon heat treatment of the (α_2 + γ) Ti-Al alloys from the high temperature α domain. The marked region (blue colour) shows the domain under the influence of sympathetic nucleation, based on and reproduced from [57].

2.1.2.2 Microstructures in PST crystals

The microstructure of PST is a single lamellar colony consisting of parallel platelets of the γ-

and α_2-phases. The orientation relationship between these α_2- and γ- phases are related by the Blackburn orientation correlation, which is $\{111\}\gamma \parallel \{0001\}\alpha_2$, $<1\bar{1}0>\gamma \parallel <11\bar{2}0>\alpha_2$. Therefore, all α_2 are parallel to each other, while γ-phase forms 3 domains and 3 twinned domains (6 variants). Because of this, corresponding domains are parallel to each other. Moreover, due to its lattice parameter *a* which is smaller than *c*, there are small misorientation angles. For example, the lamellar structures of well-aligned PST crystals of a Ti-45Al-8Nb alloy observed under TEM, is shown in Figure 2.5. Figure 2.5(a) is a bright-field image of a Ti-45Al-8Nb specimen, which shows the original ($\alpha_2 + \gamma$) lamellar structure before a tensile testing. Figure 2.5(b) is a high-resolution image of the specimen after deformation. It shows the ultrafine twinning of the PST specimen after tensile deformation. The deformed specimen shows multiple-twinned structures containing three twin boundaries γ_A/γ_B, γ_B/γ_C and γ_C/γ_D [28]. As reported in [28], the spacing between adjacent twin-boundaries is about 10 nm after tensile testing. The results indicate that the deformation twinning mechanism refined the twin spacing. The refined nano-twinned structures are important in PST since it has the potential to enhance the strength without the loss of ductility, improve the electrical conductivity and depress the formation of Kirkendall voids. Moreover, it has been reported that the ductility and mechanical strength improve with a decrease of twin thickness in PST crystals [65].

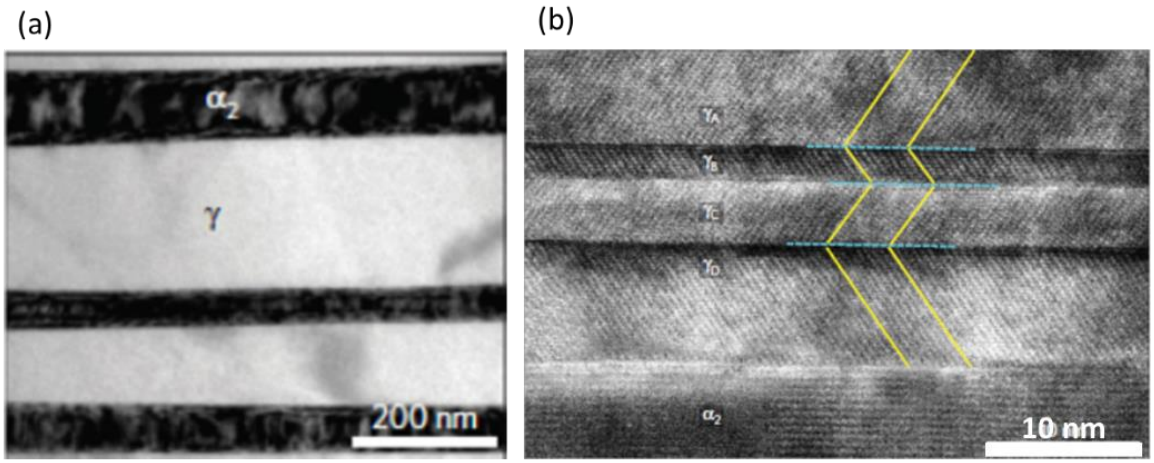

Figure 2.5 Microstructure of a Ti-45Al-8Nb PST crystals at room temperature: (a) Bright-field TEM image of the specimen before the tensile test. (b) A high-resolution TEM image of the specimen after the tensile test, reproduced from [28].

Generally, the lamellar structure is formed through a two-step phase transformation sequence $\alpha \rightarrow \alpha + \gamma \rightarrow \alpha_2 + \gamma$ or $\alpha \rightarrow \alpha_2 \rightarrow \alpha_2 + \gamma$ [2, 66, 67]. From an atomic perspective, α-phase with the hexagonal closed pack (*hcp*) based structure transforms to a face centered cubic (*fcc*) based structure with two possible stacking sequences ABCABCABC and ACBACBACB from ABABABAB stacking by dislocation gliding, as shown in Figure 2.6 [68] followed by ordering of the *fcc* phase [66, 69]. In total, this process leads to six variants of γ-phase, as shown in Figure 2.7 [69, 70].

Kim *et al*. and Dey *et al*. have described how lamellar structures are formed by α grain refinement in γ-based Ti-Al alloys during heating cycles [57, 71]. Kim *et al*. explained this phenomenon as recrystallization during heating, since the original lamellar orientation completely disappeared after heat treatment [71]. Dey *et al*. reported that initial γ-lamellae nucleated at prior α/α grain boundaries during cooling by a heterogeneous nucleation mechanism [57], eventually forming a lamellar microstructure [57, 72-74] with <111> directions of the γ-phase parallel to the growth direction of the columnar grains upon rapid cooling. The orientation between the α_2- and γ-phases followed the Blackburn relationship and the lamellar interfaces of this texture are perpendicular to the heat flow direction.

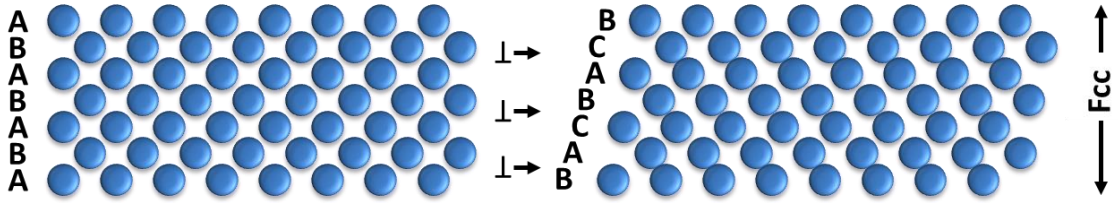

Figure 2.6 The schematics of *hcp* to *fcc* structure change on (0001) planes of *hcp* [68].

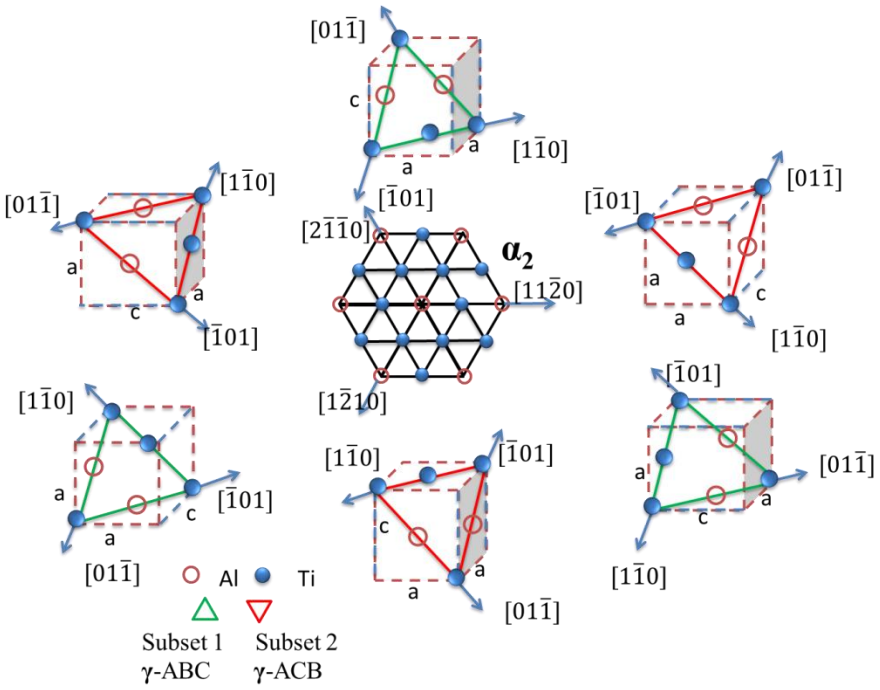

Figure 2.7 The schematics of the six orientation variants of the γ-phase oriented differently in relation to the basal plane of the α_2-phase [69, 70].

The interfaces of the lamellar structure are beneficial for twinning in the γ-phase [75]. As shown in Figure 2.8, twins form by superposing planar faults stacked on {111} planes [16]. Twins nucleate on partial dislocation loops of 1/6<11$\bar{2}$] as indicated in [75, 76].

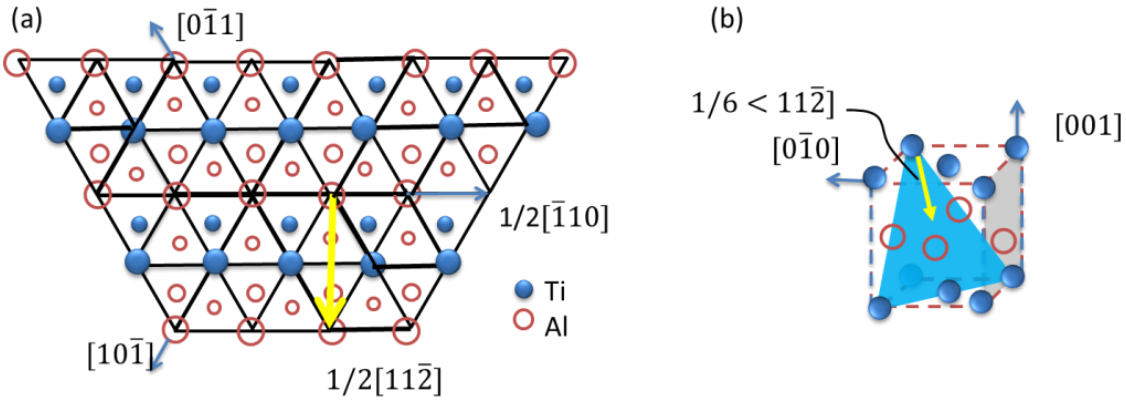

Figure 2.8 Twinning systems in γ-phase of tetragonal $L1_0$ lattice: (a) schematic representation of a three-layer atom sequence stacking on the (111) plane displayed by small, medium and large red circles [77]; (b) crystallographic lattices with the twinning mechanism [78].

2.1.2.3 Microstructures in TNB alloys

The TNB alloys with higher niobium content have fine microstructures and superior mechanical strength [79]. They can have a near-γ phase microstructure or a duplex microstructure depending on the exact composition and heat treatment.

In 2007, Chladil *et al*. [80] studied Ti-45Al-(5/7.5/10)Nb alloys produced by hot isostatic pressing (HIP) at 200 MPa at a temperature of 1553 K and the microstructure is shown in Figure 2.9(b-d). The duplex microstructure, such as the Ti-45Al-(5/7.5)Nb, consists of globular γ-TiAl grains and lamellar colonies of (γ-TiAl + α_2-Ti_3Al). The average grain size is in the range of 15-20 μm. The microstructures are very homogeneous and show no visible phase segregation. By comparing Figure 2.9(b) and (c), it is evident that the addition of niobium does not have a great deal of influence on the present α_2-phase fraction. The temperature ($T_{\gamma,solv}$), at which the (α + γ)- phase field transforms to the α-phase, is not changed much, but the Ti-45Al-10Nb alloy exhibited a near-γ phase microstructure with a lower lamellar phase fraction (see Figure 2.9(d)).

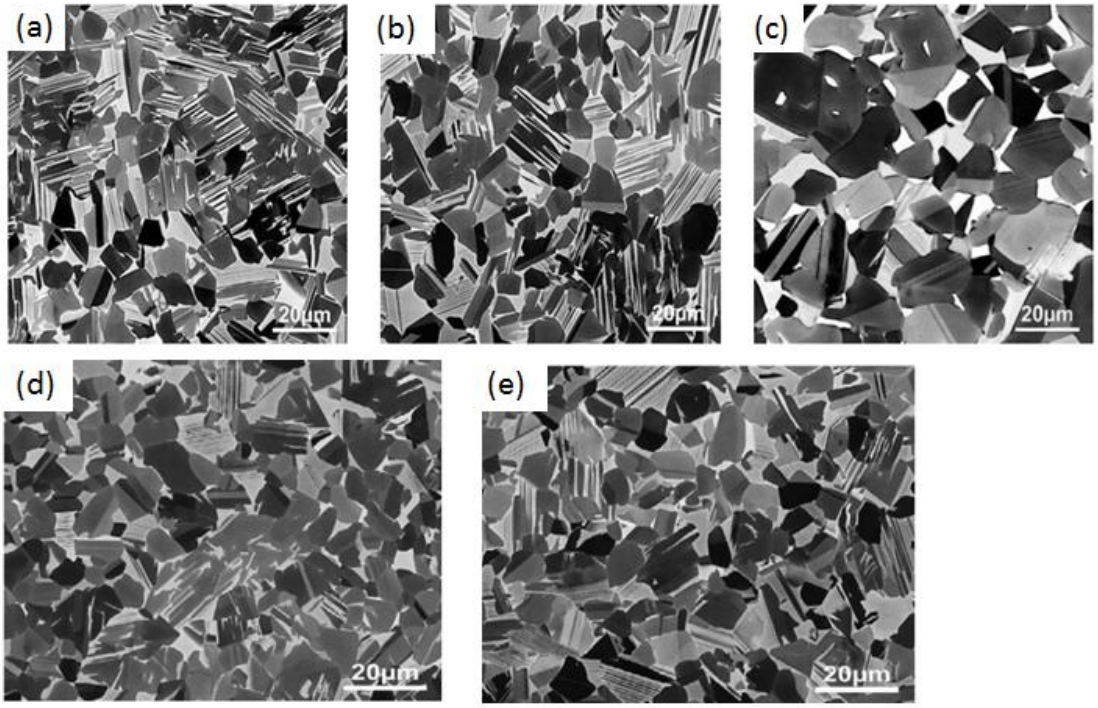

Figure 2.9 Scanning electron microscopy pictures after HIP at 200 MPa and 1553 K (a)Ti-45Al-5Nb [80], (b)Ti-45Al-7.5Nb[80], (c)Ti-45Al-10Nb [80], (d) Ti-45Al-7.5Nb-0.25C [81, 82], (e) Ti-45Al-7.5Nb-0.5C [81, 82]: (a-c) and (d, e) are based on and reproduced from [80], [81, 82] respectively.

Figure 2.9(b) show the general microstructures of powder metallurgical alloys Ti-45Al-5Nb after HIP and rolling, respectively. The dark grey to black grains are the γ-phase while the α_2-grains are white as confirmed by EDX analysis. A near-γ phase microstructure with numerous annealing γ-twins was found, providing evidence that the stacking fault energy in Ti-Al alloys is low at high niobium concentrations. The SEM pictures of Ti-45Al-7.5Nb-(0.25/0.5)C alloys after HIP at 200 MPa and 1553 K for 2h are shown in Figure 2.9(e) and (f) [81, 82] and show a homogeneous duplex microstructure.

Addition of carbon improves the strength of TNB alloys. For example, the strength of Ti-45Al-5Nb is lower than that of Ti-45Al-5Nb-0.5C sheet at room temperature by 200 MPa, reported in [20].

2.1.3 Phase diagram

The binary phase diagram of Ti-Al has in recent years been studied experimentally as well as by thermodynamic calculation [11, 12, 42, 83] and although there is still some controversy, it seems that the most accepted version is that of Schuster and Palm [11]. More recently, Witusiewics *et al.* [12] proposed a new version as shown in Figure 2.10(a). Values suggested for the eutectoid temperature (T_{eu}), where α-phase decomposes into the (α_2 + γ)-phases upon cooling under equilibrium conditions and α-transus temperatures ($T_{\gamma,solv}$), where α transforms to γ-phase are listed in Table 2.2 [11, 12].

Table 2.2 The transition temperatures of Ti-45Al.

The transition temperatures			References
$T_{\gamma,solv}$	T_{eu}	$T_{\gamma,max}$	
1574K	1393K	-	[11]
1543K	1392K	-	[12]
1565K	1453K	1250K	[44]

Thermodynamic assessments of Ti-Al-Nb were investigated by several research groups [81, 84-86], but the reported phase diagrams do not fit well with the liquidus, solidus temperatures or invariant reactions. Chen *et al*. [87] has constructed the phase diagram of Ti-Al-8Nb, indicating that the addition of niobium shifts the phase boundaries and increases the transition temperature. However, the presence of three-phase region has not been reported in [87]. The phase diagram of Ti-Al-10Nb established by Witusiewics *et al.* [12] is shown in Figure 2.10(a). Based on a high-energy X-ray study, Schmoelzer *et al.* [63] proposed the phase diagram of Ti-44Al-4Nb-(0-10Mo),shown in Figure 2.10(b). Both phase diagrams indicate the presence of a (α/α_2 + β + γ) three-phase region. However, the exact location of the phase boundaries and the multi-phase regions in Ti-Al-Nb alloys are still not clear [80]. Moreover, the influence of pressure on the pertaining phase equilibria has yet to be established.

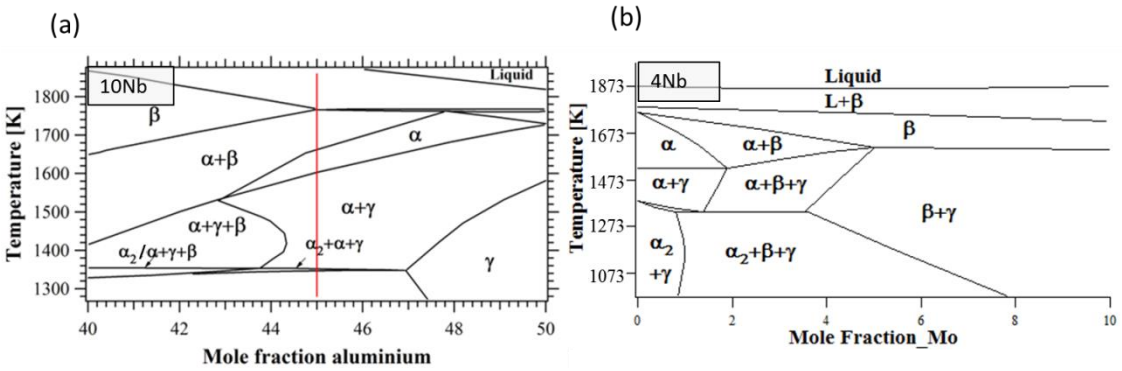

Figure 2.10 (a) The phase diagram of the Ti-Al-10Nb (at. %) alloy system, reproduced from [12]; (b) The phase diagram of Ti-44Al-4Nb-(0-10) Mo obtained by thermodynamic simulations, reproduced from [63].

2.1.4 Mechanical properties

The unique properties of the consistent phases in the γ-based Ti-Al Intermetallics are attractive, listed in Table 2.3. It shows low density, high modulus, good strength, and good resistance against oxidation. However, fracture toughness, fatigue resistance and poor ductility remain issues of concern [88].

Table 2.3 Properties of different phases in γ-based titanium aluminides, based on [88].

Property	α_2-Ti_3Al	γ-TiAl	References
Structure	$D0_{19}$	$L1_0$	[16]
Density (g/cm^3)	4.1-4.7	3.7-3.9	
Youngs Modulus (GPa)	110-145	160-180	
	147.05-0.0525T	173.59-0.0342T	[89]
Yield strength (MPa)	700-990	350-600	[16]
Tensile strength (MPa)	800-1140	440-700	[16, 90]
Room temp. ductility (%)	2-10	1-4	
High temp. ductility (%/°C)	12-20/660	10-600/870	
Room temp. Fracture ($MPa\sqrt{m}a$)	13-30	12-35	
Creep Limit (°C)	750	750[a]-950[b]	
Oxidation Limit (°C)	650	800[c]-950[d]	
Thermal expansion (Ti-46Al-1.9Cr-3Nb)	a: $\alpha[K^{-1}] = 3.2 \times 10^{-6}$ c: $\alpha[K^{-1}] = 3.2 \times 10^{-6}$		[91]

[a] duplex microstructure, [b] fully lamellar microstructure uncoated, [d] coated.

2.1.4.1 Hardness of γ-based Ti-Al alloys

Microhardness tests on γ-based Ti-Al alloys have been conducted by earlier researchers as listed in Table 2.4 [20, 88]. The average micro-hardness decreased from 350 to 306 H_v when heated from 373 K to 673 K [88]. Gerling *et al.* [20] reported that the hardness of Ti-Al-Nb

alloys increased with the addition of carbon. The hardness of a Ti-45Al-5Nb-0.5C alloy following HIP was 363 H_v, which is about 15% higher than the carbon-free alloy (316 H_v). Srinivasarao *et al*. [92] have done microhardness measurements on a Ti-45Al-2Nb-2Mn-0.8TiB_2 (vol %) alloy before and after the application of high pressure torsion. The hardness increased from 300 to 550 H_V but the mechanism of hardening was not identified.

Table 2.4 Microhardness tests of different composition of titanium aluminides [88].

Composition	Load	Method	Ref
Ti-45Al-5Nb-(0.5C)	10kg	Vickers hardness method	Gerling *et al*. [20]
Ti-(40-48)Al	200g	Vickers hardness method	Ma [88]

2.1.4.2 Strength and ductility

Tensile/compression tests were performed on polycrystalline TiAl alloys to measure elongation and strength at room temperature [90, 93]. Löber *et al.* [93] performed compression tests on a Ti-28.9Al-9.68Nb-2.26Mo-0.024B (mass %) alloy and its yield strength varied with different processing techniques. It reached nearly 1800 MPa under casting conditions with good elongation. Liu *et al.* [90] showed the stress-strain curve under compressive deformation at 1273 K and 1473 K. At high temperature, the elongation of Ti-Al-Nb alloys increased greatly [90]. Appel *et al.* [94] measured tensile elongations higher than 3% in a novel Ti-(40-44)Al-8.5Nb alloy at room temperature. Zambaldi *et al.* [95] calculated the stress-strain curves for PST crystals, by modelling 64-grain clusters of a Ti-46Al-8Nb alloy and the ductility was more than 2% at room temperature [96]. Chen *et al.* [28] measured the yield strength and tensile ductility of a Ti-45Al-8Nb PST crystal as 735 MPa and 7.6% at ambient temperature, respectively.

Therefore it is possible to improve the ambient-temperature strength and ductility by different processing techniques, by controlling the microstructure and by adjusting the composition.

2.2 Neutron and synchrotron X-ray diffraction on Ti-Al alloys

Conventional experimental techniques have significant limitations when applied to the analysis of γ-based Ti-Al alloys. The small inter-lamellar spacing following severe plastic deformation cannot be resolved by optical or even scanning electron microscopy. Transmission electron microscopy is confined to the analysis of very small areas. Neutron and high energy X-ray diffraction provide good grain statistics of large samples [64].

Therefore, synchrotron X-ray and neutron diffraction techniques have been used in this study to better understand the fundamental relationships between microstructure and the mechanical properties of γ-based Ti-Al alloys.

2.2.1 The basics of diffraction

Generally, the incident beams are scattered by the different lattice planes of materials and diffracted waves interfere, producing constructive and destructive signals.

Different crystal material produces different diffraction patterns according to the Bragg's law [97], which is the main underlying diffraction theory for this work. As can be seen in Figure 2.11, the incident beam at the angle θ can be reflected strongly at the plane ($h\ k\ l$) with spacing d_{hkl}. The travelling distance difference of the scattering wave between the consecutive lattice planes is calculated to be $\overline{SU} + \overline{UT} = 2d\ sin\theta$, which has to be a multiple of wavelength λ, well-known as Bragg's equation: $n\lambda = 2d_{hkl}\ sin\theta$.

Moreover, $\boldsymbol{k_i}$ is the incident wave vector, $\boldsymbol{k_f}$ the reflected one. Each reflection from the same lattice spacing has its reciprocal lattice vector (**Q**). Figure 2.11 shows the relationship between the vector $\boldsymbol{k_f}$ (or $\boldsymbol{k_i}$) and **Q**: $\boldsymbol{k_f} = \boldsymbol{k_i} + \mathbf{Q}$ and the value $Q = 2k\ sin(\theta)$, where $k = 2\pi/\lambda$.

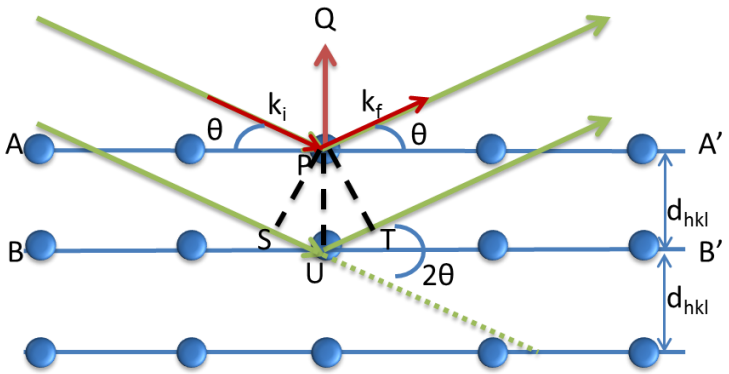

Figure 2.11 Schematic of neutron and X-ray diffraction, where $\boldsymbol{k_i}$ is the incident momentum transfer vector, $\boldsymbol{k_f}$ the reflected one, and $\boldsymbol{k_i} + \mathbf{Q} = \boldsymbol{k_f}$. 2θ is the angle between the two, d_{hkl} is the lattice spacing, and **Q** stands for reciprocal lattice vector.

The relationship between wave vectors and reciprocal lattice of the crystal is demonstrated in Figure 2.12. The value of incident wave vector k_i is equal to the reflected vector k_f (incoherent scattering is not considered here). The circular profile of radius k_f is plotted accordingly, which is referred as Ewald sphere. The reciprocal lattice spot on the circle of Ewald sphere indicates the corresponding lattice plane which can be reflected. Thereby, the scattering vector **Q** can be measured by the distance between the reciprocal lattice spot and the original point. By X-ray and neutron diffraction, with a single crystal rotated, the reciprocal space map could be recorded.

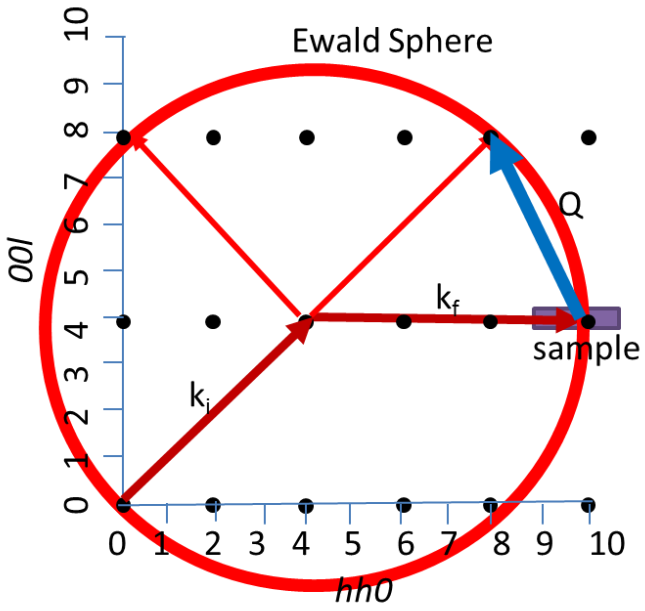

Figure 2.12 The schematic of Ewarld sphere, representing the relationship between reciprocal lattice and wavevector, where $\mathbf{k_f}$ is the reflected vector and **Q** the scattering vector, and the incident momentum transfer vector $\mathbf{k_i} = \mathbf{k_f} - \mathbf{Q}$.

2.2.2 The differences between conventional XRD, HEXRD and neutrons

Neutron and X-ray diffraction are complimentary techniques on γ-based Ti-Al alloys. High-energy synchrotron X-ray diffraction techniques [98] overcome the impediments of traditional X-ray and microscopic methods, while *in-situ* techniques make time-resolved information available.

The differences between conventional XRD, HEXRD and neutrons are illustrated as follows. Firstly, the incident neutron beam interacts with the nuclei of the atoms of a specimen and is diffracted. X-rays, on the other hand, are diffracted by the electron density distribution of the atoms. Secondly, the attenuation length of neutron radiation is much greater than for X-rays. Moreover, neutron scattering has one particular complementarity advantage over X-ray diffraction in structural analysis of the Ti-Al alloys due to the neutron scattering lengths. It is due to their particular scattering lengths (details are described in the section 2.2.2.2), which is

one of the important contributors for the structure factor. The data of penetration depths and scattering lengths of conventional XRD, HEXRD and neutrons are listed in Table 2.5.

Table 2.5 Properties of conventional XRD, HEXRD and neutrons.

	XRD	HEXRD	Neutrons
Wavelength	1.5418 Å	0.1393 Å	2.419 Å
Wave number	4.0752 $Å^{-1}$	45.12 $Å^{-1}$	2.598 $Å^{-1}$
Energy	8.04 keV	~100 keV	14 meV
attenuation length	74.67 μm Al at 8.04 keV	23.56 mm Al at 100 keV	16.77 cm Al at 14 meV
(Atomic form factors *f*)	6.203 fm (f_{Ti})		-3.438 fm (b_{Ti})
Average scattering lengths *b*	3.666 fm (f_{Al})		3.449 fm (b_{Al})

* $fm=10^{-15}m$

2.2.2.1 The penetration ability

As shown in Table 2.5, conventional X-ray diffraction only reveals information from the surface of a specimen since its attenuation length is relatively low. For example, I have calculated that it is 74.67 μm Al-plate for Cu-K_α. The attenuation length of high-energy X-ray is deeper, e.g., 23.56 mm for Al at 100 keV, while the attenuation length of neutron is 16.77 cm, agreeing well with the results from references [98, 99]. Thus, traditional X-ray diffraction can only detect structural information from the surface while neutron scattering provides bulk information [100, 101].

The beam attenuation length τ_0 is the distance where the beam has not been absorbed. It is calculated by the equation $\tau_0 = 1 / (\sum \cdot \rho)$, where the mass absorption coefficient $\sum$ is taken from literature [102] and ρ is the material density. The X-ray attenuation lengths of γ-phase, α-phase and the γ-based Ti-Al alloys are calculated and shown in Figure 2.13. It clearly shows the penetration ability of X-ray beam increases by its energy. For example, the attenuation length is 19 μm at Cu-K_α radiation (8.04 keV) and raises to 10 mm at 100 keV in titanium aluminides.

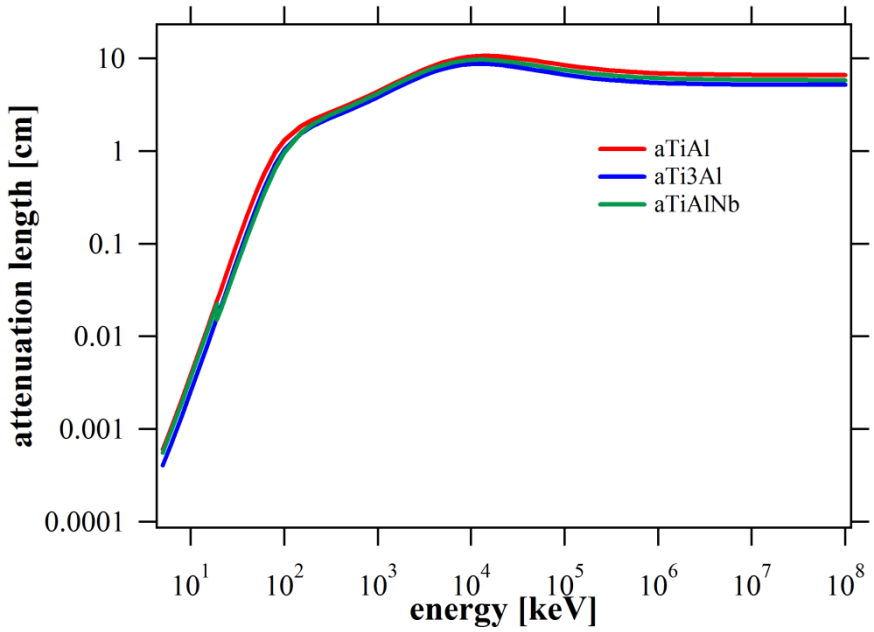

Figure 2.13 X-ray attenuation lengths of the γ-phase (aTiAl), α-phase (aTi3Al) and the γ-based Ti-Al alloys (aTiAlNb) as a function of X-ray beam energy.

2.2.2.2 Structure factor

The intensity (I) of the diffraction peak is largely determined by the structure factor (F). For X-rays, the structure factor, representing the amplitude and phase of a diffracted beam from the lattice plane (h k l), is calculated by

$$F_{hkl} = \sum_j f_j \exp\left(\left(2\pi i\left(hx_j + ky_j + lz_j\right)\right)\right)$$
$$= \sum_j f_j \cos(2\pi\left(hx_j + ky_j + lz_j\right)) + i\sum_j f_j \sin(2\pi\left(hx_j + ky_j + lz_j\right))$$

, where f_j stands for the atomic form factor (also called atomic scattering factor) for the j_{th} atom in a unit cell, (h k l) denotes the Miller indices for this crystal Bragg reflection [103].

For neutron diffraction, the structure factor F_{hkl} of neutrons is expressed by a similar equation above except that the X-ray atomic form factor, *f*, needs to be replaced by the neutron scattering length, *b*. In terms of Ti-Al alloys, the corresponding neutron scattering lengths of Ti (-3.438 fm) and Al (3.449 fm) are of opposite sign with similar magnitudes. Therefore, neutron diffractograms contain superstructure peaks from the ordered α_2-phase, thereby

paving the way for order-disorder transition detection [104]. The peak intensity from a fully disordered phase is nearly zero due to the neutron scattering lengths of Ti and Al. Instead, the superstructure reflections from the ordered phase are reflected strongly in neutron scattering [104]. This advantage offers neutron scattering the capability to not only distinguish the disordered and ordered phases in Ti-Al alloys but also determine the degree of ordering.This feature is well used to characterize the γ-based Ti-Al alloys. Watson *et al.* and Kabra *et al.* [105, 106] performed *in-situ* neutron diffraction experiments during heating and the results clarified the order-disorder transition $\alpha_2 \rightarrow \alpha$ in Ti-43.9Al-4Nb-1Mo-0.1B and Ti-44Al-7Mo alloys. The observed weak and broad peaks from the ordered α_2-phase at 1673 K, confirmed the presence of an α_2-phase in Ti-43.9Al-4Nb-1Mo-0.1B alloys at this temperature [104].

In comparison, XRD techniques obtain much higher intensity of fundamental structure peaks. Consequently, XRD is a complementary technique to neutron diffraction and frequently applied for phase transformations studies in Ti-Al alloys [101, 105].

2.2.3 Atomic order and disorder

There are two distinct parts to study the atomic order and disorder: (1) the order-disorder phase transition; (2) the atomic structure.

2.2.3.1 Order-disorder transition, studied by HEXRD and neutron diffraction

The mechanical properties of γ-based Ti-Al alloys change during order-disorder phase transitions and hence, a study of order-disorder transitions is an essential pre-requisite to the development of these alloys. For example, the disordered β-phase improves the hot workability and good processing characteristics at high temperature because it not only has an isotropic structure but also a very fast dynamic recovery process [107]. The ordered β_o-

phase reduces the ductility at room temperature, in addition to being more stable at low temperature [108-109].

Since it is not easy to measure the disorder-order transition by quenched samples using conventional SEM and TEM methods [79], Yeoh *et al.* and Clemens *et al.* [21, 44] used *in-situ* synchrotron HEXRD techniques. The disordering temperature in a Ti-Al alloy was calculated by assessing the site occupancy of the α-phase by *in-situ* HEXRD [44]. Clemens *et al*. reported the presence of disordered α- and β- phases above 1573 K [21].

Schmoelzer *et al*. have conducted a neutron diffraction experiment using a Ti-43.9Al-4Nb-1Mo-0.1B alloy by the diffractometer SPODI [62, 110]. The diffraction intensity of the peaks of the different phases during heating is shown in Figure 2.14. The transition temperatures of $\alpha_2 \rightarrow \alpha$ and $\beta_o \rightarrow \beta$ were determined by *in-situ* neutron diffraction experiments. Neutron diffractograms clearly recorded the superstructure of the order α_2- and β_o- phases. However, only a few diffractograms could be obtained because of the long acquisition times of the SPODI diffractometer. In order to determine the order-disorder transition temperatures more accurately by the use of neutron diffraction, the WOMBAT facility (at the OPAL reactor of ANSTO in Lucas Heights, Australia) was used since it provides significantly higher flux and hence is better suited to such studies [6].

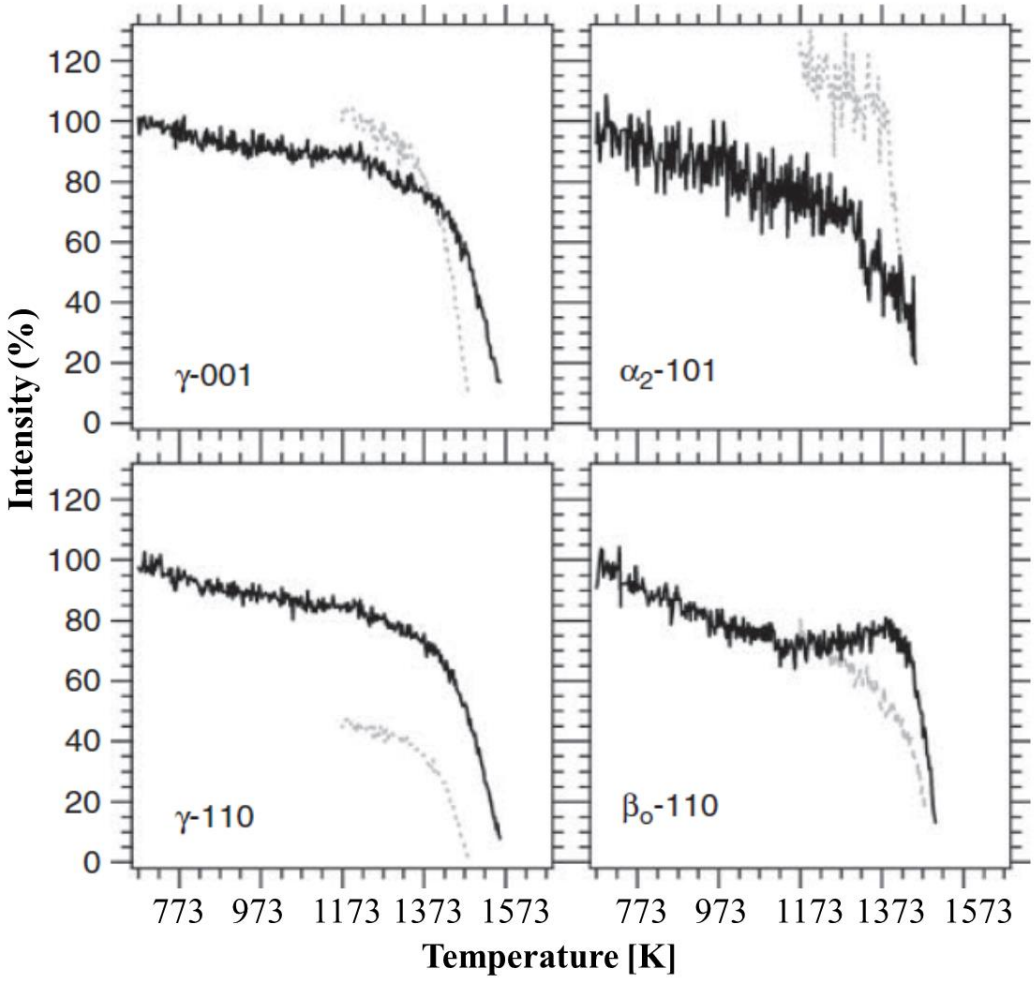

Figure 2.14 Ordering-disordering temperatures of α/α_2 and β/β_o and the dissolution temperature of γ-phase in a Ti-43Al-4Nb-1Mo-0.1B alloy. The solid black lines were recorded during heating and dashed grey lines are on cooling [101].

2.2.3.2 Short-range-order structure, studied by diffuse scattering

The other important part of the study of atomic order and disorder is the atomic structure. Short-range-order structure refers to a regular atomic arrangement over a short distance, while the correlation is lost over longer distances. In this thesis work, the short-range-order structure attracts more attentions, as one of the important atomic disorder structure in Ti-Al alloys.

As known, Bragg diffraction occurs if scattering occurs constructively with long-range-order (coherent scattering). Disorder in a crystal lattice reduces the amplitude of the Bragg peak.

This decrease in scattering intensity contributes to diffuse scattering (incoherent scattering). The diffuse scattering thus arises from the local disorder (not the long-range structural order). For example, in Ti-Al intermetallics, the kind of atoms can be disordered, while their locations still occupy the same lattice. Such statistical disorder reduces the coherence and thus the coherent Bragg peaks, while the incoherent part is increased, scattering into regions between the Bragg peaks. Short-range correlations can still exist, which give some modulations of the diffuse scattering.

Generally, different types of disorder, such as static disorder (substitutional disorder, stacking and other planer faults) and dynamic disorder (orientational disorder and magnetic disorder), lead to diffuse scattering. Therefore, diffuse scattering, which arises from a breakdown of long-range-order, is the method of choice to study the short-range order structure. For single crystals, diffuse scattering is well aligned within the reciprocal lattice and reflects the ordered and disordered structures as shown for example on $PbZn_{1/3}Nb_{2/3}O_3$ in Figure 2.15 by Paściak *et al.* [111]. The diffraction pattern of its long-range-order structure shows the high intensity and sharp Bragg peaks. The wide and weak peaks represent the short-range-order structure [112].

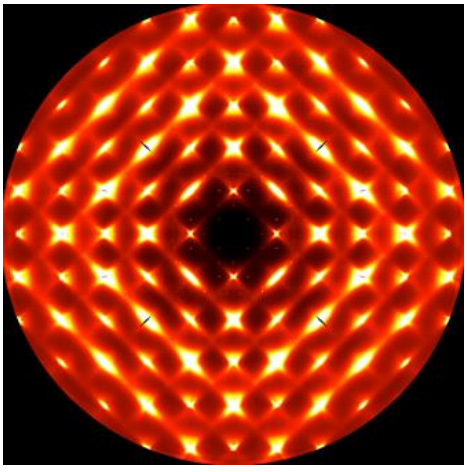

Figure 2.15 X-ray diffuse scattering of $PbZn_{1/3}Nb_{2/3}O_3$, measured by Paściak *et al.* at the Advanced Photon Source Synchrotron in Chicago [111].

2.2.4 Lattice parameter and lattice strain

Lattice parameter and strain evolution, which in part relates to the changes in atomic concentrations during phase transformations, is of vital interest in studying Ti-Al alloys since a new phase forming from a super-saturated parent phase is always accompanied by a change of chemical composition.

According to Vegard's law [113], this transitional process always results in a change in the lattice parameters of the pertaining phases [114, 115]. It is also important to identify the lattice parameters by which microstructural evolution and microstructural stability can be appraised when deformation processing of these alloys at high temperature is considered. For instance, a change in the *c*/*a* ratio of the α/α_2 lattice influences the slip and twinning deformation mechanisms. Moreover, changes in the lattice parameter impact on orientation relationships and interphase stress development. In addition, the mechanism and morphology of phase transformations need to be taken into account since they play an important role in achieving microstructural stability.

Although lattice parameter evolution plays a pivotal role in assessing the high-temperature behavior of titanium-aluminides, little information has been provided to date except the following: In 1990, Shull & Cline [116] conducted *in-situ* X-ray diffraction studies on the phase transformation in Ti-45Al alloys. In 2004, by employing *in-situ* high energy X-ray diffraction, Novoselova *et al*. [47] have determined the lattice parameter of a Ti-46Al-1.9Cr-3Nb alloy, as shown in Figure 2.16(a). The volume of the unit cell as a function of temperature in the temperature range 293-1723 K was utilized to calculate the thermal expansion coefficient [47]. More recently Yeoh *et al.* [44] reported the *c*/*a* ratio of the γ-phase in a Ti-45Al-7.5Nb-0.5C alloy during heating in a synchrotron experiment. It keeps decreasing until the α_2 to α disorder transformation happens. In 2011, Schmoelzer *et al.* [63]

showed that a decrease of *c*/*a* ratio in the γ-phase is related to the aluminium concentration in the γ-phase above 1173 K, as depicted in Figure 2.16(b). This means that the *c*/*a* ratio in the γ-phase decreases during heating, and at 1503 K, it reaches a minimum due to a minimum in the aluminium content. These studies emphasize that knowledge of the lattice parameter is important in the evaluation of the material behavior.

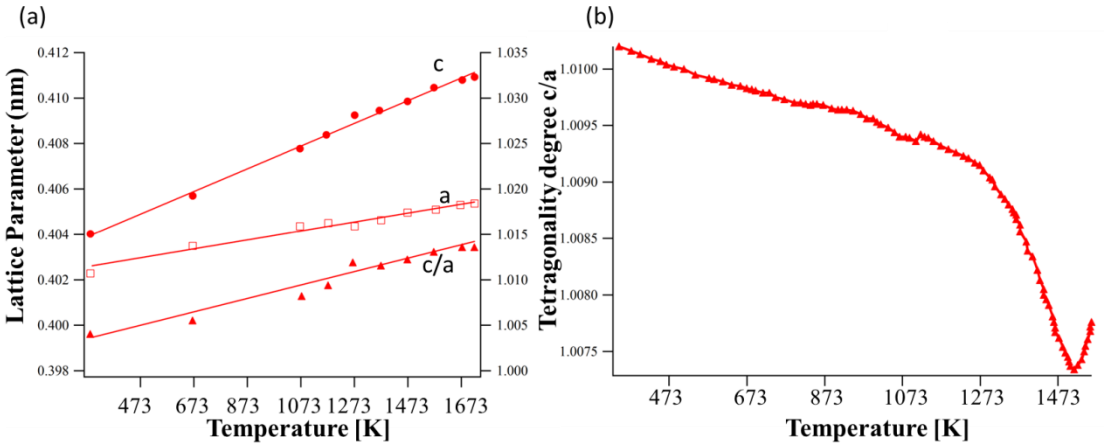

Figure 2.16 (a) Lattice parameters of the γ-phase in a Ti-46Al-1.9Cr-3Nb alloy reproduced by [47], and (b) *c*/*a* ratio of the γ-phase in Ti-43.5Al-4Nb-1Mo-0.1B as a function of temperature reproduced from [63].

Another factor influencing the lattice parameter is strain. Figure 2.17 shows three types of strain [117, 118]. ε^{I} represents macrostrain within a volume averaged over a statistically representative number of grains, for example the stress discussed in section 2.1.4.2. ε^{II} is the deviation of the volume averaged strain of (*h k l*) from the macrostrain as determined by diffraction peak broadening by superposition of individually, shifted reflection curves. ε^{III} is the strain, which characterizes the local strain deviation within a single grain. It is related to sub-peak broadening, by strain gradients within a crystallite, also known as the local stain.

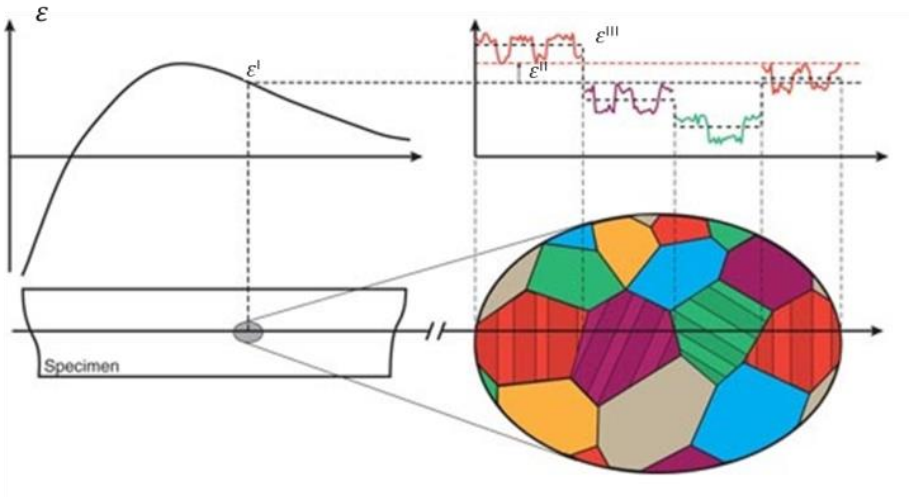

Figure 2.17 Phenomenological classification of internal strains. ε^{I}, ε^{II} and ε^{III} are respectively macro-, meso- and microscopic strains [119].

Macroscopic strain evolution in γ-based Ti-Al alloys has not been evaluated by high energy X-ray diffraction pattern analysis, save for a study by Liss *et al.* [17]. In diffraction analysis, macroscopic strain is deduced from peak shifts. Similarly, Sarkar *et al.* [120] reported macroscopic strain calculated by electron scattering patterns from selected areas as shown in Figure 2.18.

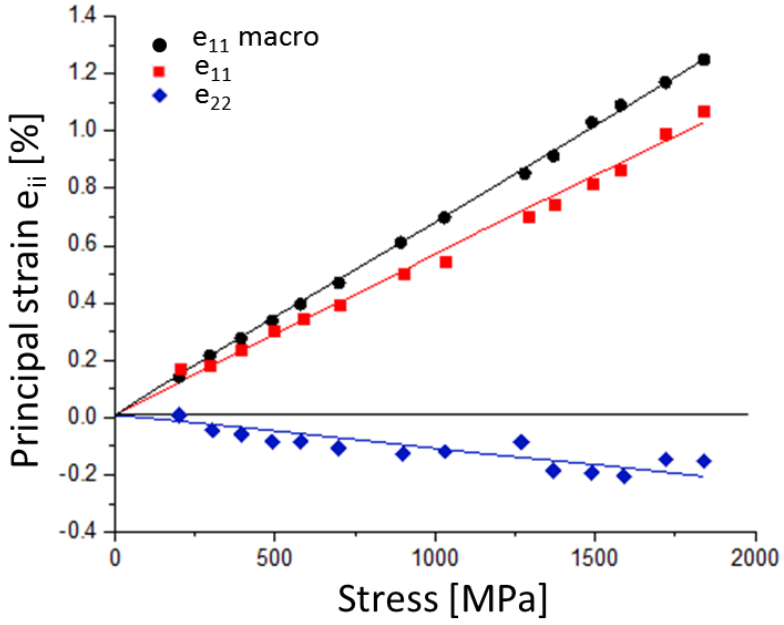

Figure 2.18 Linear dependences of macroscopic strains of Ti-55Al. The figure is reproduced based on [120].

2.3 Severe plastic deformation of selected titanium aluminides

A recent development is to manufacture titanium aluminide components under extreme conditions and severe plastic deformation. The dearth of information of the effect of severe plastic deformation on γ-based Ti-Al alloys prompted this part of the present study, in which high pressure torsion was used as a means of applying severe plastic deformation. High pressure torsion techniques have been used to improve plasticity and ductility. The application of high pressure torsion is a new approach to improve and intensify grain refinement [121], mainly used for understanding the phase transformation of titanium aluminides at this stage. The description of high pressure torsion method is described in section 3.1.3. Since these processes operate at high temperature it is important that microstructural integrity be maintained - grain growth has to be limited during high-temperature processing and internal stresses need to be minimized.

2.4 Laser-scanning confocal microscopy of selected Ti-Al alloys

In-situ high-temperature laser-scanning confocal microscopy is employed to study the microstructural evolution of Ti-Al alloys during heating and cooling. In 2008, Liss *et al.* [61] captured the formation and precipitation of ultrafine γ-lamellae in a Ti-45Al-7.5Nb alloy during heating by using a HTLSCM technique, as shown in Figure 2.19. In 2009, Watson *et al*. [105] observed slow grain growth kinetics in a Ti-44Al-4Nb-1Mo-0.1B alloy in the high temperature (α + β)-phase field by using the same technique. These studies provide convincing evidences that high-temperature laser-scanning confocal microscopy can be usefully employed to capture microstructural changes *in-situ,* at high temperature and at high resolution.

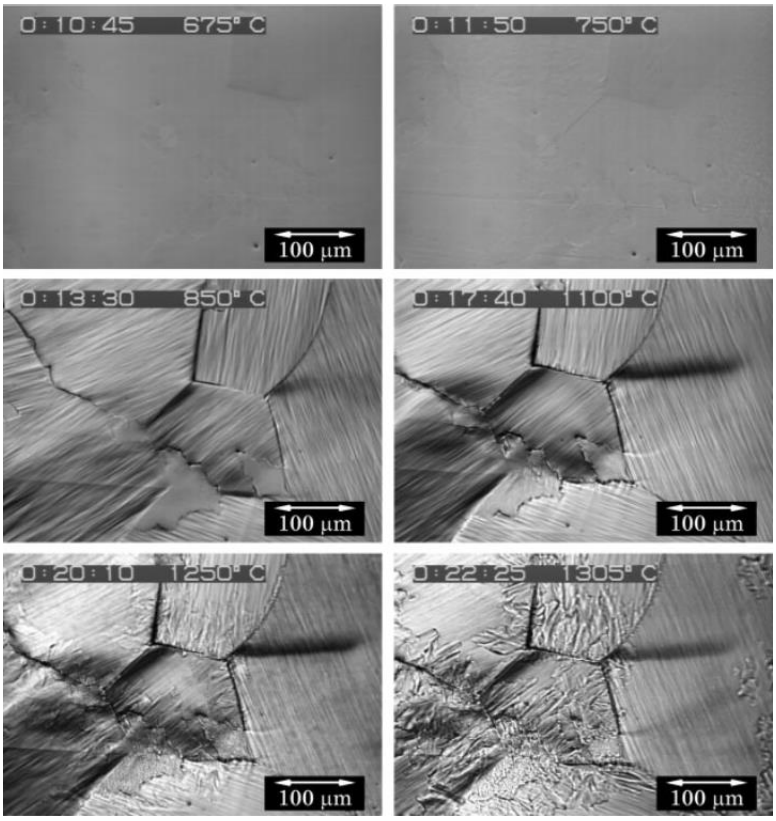

Figure 2.19 Micrographs of a Ti-45Al-7.5Nb alloy at selected temperatures during heating as shown in the annotations, based on and reproduced from [61].

2.5 Conclusion

In conclusion, the superior mechanical properties of γ-based Ti-Al alloys are largely attained by microstructural improvements. In earlier studies, detailed microstructural development from single crystals to polycrystalline γ-based Ti-Al alloys, has not been analyzed in detail. In addition, lattice evolution under conditions of severe plastic deformation has received little attention. This dearth of information prompted the present fundamental study, which is aimed at establishing a link between the pertaining mechanical properties and microstructure. This study is specifically targeted at providing better understanding of the nature, behavior and response to deformation of γ-based Ti-Al alloys. To this end, high pressure torsion techniques can be used to apply severe plastic deformation aimed at reducing grain size. Neutron and high energy X-ray diffraction, as complimentary techniques are ideally suited to study phase transformations of γ-based Ti-Al alloys. High temperature laser-scanning confocal

microscopy provides an excellent platform for observing *in-situ*, at high temperature and in real time the microstructural evolution in γ-based Ti-Al alloys in the course of phase transformations.

A variety of these modern experimental techniques has been used to study the evolution and structural changes occurring in selected Ti-Al intermetallics under extreme operating conditions at high-temperature, high-pressure and severe plastic deformation.

2.6 Reference

[1] M. Yamaguchi, H. Inui, and K. Ito, "High-temperature structural intermetallics," Acta materialia, vol. 48, pp. 307-322, 2000.

[2] F. Appel and R. Wagner, "Microstructure and deformation of two-phase γ-titanium aluminides," Materials Science and Engineering: R: Reports, vol. 22, pp. 187-268, 1998/05/01 1998.

[3] Y. Kim, D. Morris, R. Yang, and C. Leyens, "Structural aluminides for elevated temperature applications," TMS, Warrendale, 2008.

[4] X. Wu, "Review of alloy and process development of TiAl alloys," Intermetallics, vol. 14, pp. 1114-1122, 2006/10/01/ 2006.

[5] M. S. Kesler, S. Goyel, O. Rios, D. M. Cupid, H. J. Seifert, and F. Ebrahimi, "A study of phase transformation in a TiAlNb alloy and the effect of Cr addition," Materials Science and Engineering: A, vol. 527, pp. 2857-2863, 2010.

[6] A. J. Studer, M. E. Hagen, and T. J. Noakes, "Wombat: The high-intensity powder diffractometer at the OPAL reactor," Physica B: Condensed Matter, vol. 385, pp. 1013-1015, 2006.

[7] T. Tetsui, "Development of a TiAl turbocharger for passenger vehicles," Materials Science and Engineering: A, vol. 329, pp. 582-588, 2002.

[8] D. Music and J. M. Schneider, "Effect of transition metal additives on electronic structure and elastic properties of TiAl and Ti 3 Al," Physical Review B, vol. 74, p. 174110, 2006.

[9] B. Zhang and H. Xie, "Structural Materials Properties, Microstructure and Processing," Materials Science & Engineering, vol. 281, pp. 286-291, 2000.

[10] W. J. Zhang, S. C. Deevi, and G. L. Chen, "On the origin of superior high strength of Ti–45Al–10Nb alloys," Intermetallics, vol. 10, pp. 403-406, 2002/05/01/ 2002.

[11] J. C. Schuster and M. Palm, "Reassessment of the binary aluminum-titanium phase diagram," Journal of phase equilibria and diffusion, vol. 27, pp. 255-277, 2006.

[12] V. Witusiewicz, A. Bondar, U. Hecht, and T. Y. Velikanova, "The Al–B–Nb–Ti system: IV. Experimental study and thermodynamic re-evaluation of the binary Al–Nb and ternary Al–Nb–Ti systems," Journal of Alloys and Compounds, vol. 472, pp. 133-161, 2009.

[13] Y.-W. Kim, "Effects of microstructure on the deformation and fracture of γ-TiAl alloys," Materials Science and Engineering: A, vol. 192, pp. 519-533, 1995.

[14] K. Hashimoto, M. Kimura, and Y. Mizuhara, "Alloy design of gamma titanium aluminides based on phase diagrams," Intermetallics, vol. 6, pp. 667-672, 1998/01/01/ 1998.

[15] M. Kimura and K. Hashimoto, "High-temperature phase equilibria in Ti-Al-Mo system," Journal of Phase Equilibria, vol. 20, p. 224, 1999/05/01 1999.

[16] F. Appel, J. D. H. Paul, and M. Oehring, Gamma titanium aluminide alloys: science and technology: John Wiley & Sons, 2011.

[17] K.-D. Liss, K.-I. Funakoshi, R. Dippenaar, Y. Higo, A. Shiro, M. Reid, et al., "Hydrostatic Compression Behavior and High-Pressure Stabilized β-Phase in γ-Based Titanium Aluminide Intermetallics," Metals, vol. 6, p. 165, 2016.

[18] S.-l. Xiao, J. Tian, L.-j. Xu, Y.-y. Chen, H.-b. Yu, and J.-c. Han, "Microstructures and mechanical properties of TiAl alloy prepared by spark plasma sintering," Transactions of Nonferrous Metals Society of China, vol. 19, pp. 1423-1427, 2009.

[19] T. Schmoelzer, K. D. Liss, C. Kirchlechner, S. Mayer, A. Stark, M. Peel, et al., "An in-situ high-energy X-ray diffraction study on the hot-deformation behavior of a β-phase containing TiAl alloy," Intermetallics, vol. 39, pp. 25-33, 2013.

[20] R. Gerling, F. Schimansky, A. Stark, A. Bartels, H. Kestler, L. Cha, et al., "Microstructure and mechanical properties of Ti 45Al 5Nb+ (0–0.5 C) sheets," Intermetallics, vol. 16, pp. 689-697, 2008.

[21] H. Clemens, H. F. Chladil, W. Wallgram, G. A. Zickler, R. Gerling, K. D. Liss, et al., "In and ex situ investigations of the β-phase in a Nb and Mo containing γ-TiAl based alloy," Intermetallics, vol. 16, pp. 827-833, 2008.

[22] S. Kremmer, H. Chladil, H. Clemens, A. Otto, and V. Güther, "Near conventional forging of titanium aluminides," Ti-2007 science and technology, vol. 2, 2008.

[23] H. Inui, K. Kishida, M. Misaki, M. Kobayashi, Y. Shirai, and M. Yamaguchi, "Temperature dependence of yield stress, tensile elongation and deformation structures in polysynthetically twinned crystals of Ti-Al," Philosophical magazine a, vol. 72, pp. 1609-1631, 1995.

[24] D. R. Johnson, H. Inui, S. Muto, Y. Omiya, and T. Yamanaka, "Microstructural development during directional solidification of α-seeded TiAl alloys," Acta Materialia, vol. 54, pp. 1077-1085, 2006.

[25] D. Johnson, Y. Masuda, T. Yamanaka, H. Inui, and M. Yamaguchi, "Creep deformation of TiAl-Si alloys with aligned γ/α2 lamellar microstructures," Metallurgical and Materials Transactions A, vol. 31, pp. 2463-2473, 2000.

[26] Y.-W. Kim, "Gamma titanium aluminides," JOM Journal of the Minerals, Metals and Materials Society, vol. 47, pp. 38-38, 1995.

[27] Y.-W. Kim, "Ordered intermetallic alloys, part III: gamma titanium aluminides," JOM Journal of the Minerals, Metals and Materials Society, vol. 46, pp. 30-39, 1994.

[28] G. Chen, Y. Peng, G. Zheng, Z. Qi, M. Wang, H. Yu, et al., "Polysynthetic twinned TiAl single crystals for high-temperature applications," Nature Materials, 2016.

[29] V. Güther, C. Rothe, S. Winter, and H. Clemens, "Metallurgy, microstructure and properties of intermetallic TiAl ingots," BHM Berg-und Hüttenmännische Monatshefte, vol. 155, pp. 325-329, 2010.

[30] S. Huang, "Structural Intermetallics, ed," By R. Darolia, JJ Lewandowski, CT Liu, PL Martin, DB Miracle and MV Nathal (TMS, 1993) pp, pp. 299-307, 1993.

[31] R. Gerling, H. Clemens, and F. P. Schimansky, "Powder Metallurgical Processing of Intermetallic Gamma Titanium Aluminides," Advanced Engineering Materials, vol. 6, pp. 23-38, 2004.

[32] S. Bystrzanowski, A. Bartels, H. Clemens, R. Gerling, F. Schimansky, G. Dehm, et al., "Creep behaviour and related high temperature microstructural stability of Ti–46Al–9Nb sheet material," Intermetallics, vol. 13, pp. 515-524, 2005.

[33] S. Chen, P. Beaven, and R. Wagner, "Carbide precipitation in γ-TiAl alloys," Scripta metallurgica et materialia, vol. 26, pp. 1205-1210, 1992.

[34] W. Tian and M. Nemoto, "Effect of carbon addition on the microstructures and mechanical properties of γ-TiAl alloys," Intermetallics, vol. 5, pp. 237-244, 1997.

[35] P. Gouma, M. Mills, and Y.-W. Kim, "Characterization of the precipitation process in a TiAl-based alloy with carbon and silicon additions," Philosophical magazine letters, vol. 78, pp. 59-66, 1998.

[36] K. Khan, C. Sanchez, M. Thomas, S. Naka, and -. C. Office National d'Etudes et de Recherches Aerospatiales "Development of third generation castable gamma titanium aluminides: role of solidification paths," 1997.

[37] Y. Jin, J. N. Wang, J. Yang, and Y. Wang, "Microstructure refinement of cast TiAl alloys by β solidification," Scripta Materialia, vol. 51, pp. 113-117, 7// 2004.

[38] K.-D. Liss, T. Schmoelzer, K. Yan, M. Reid, M. Peel, R. Dippenaar, et al., "In situ study of dynamic recrystallization and hot deformation behavior of a multiphase titanium aluminide alloy," Journal of Applied Physics, vol. 106, p. 113526, 2009.

[39] H. Clemens and S. Mayer, "Design, processing, microstructure, properties, and applications of advanced intermetallic TiAl alloys," Advanced Engineering Materials, vol. 15, pp. 191-215, 2013.

[40] H. Clemens, M. Schloffer, E. Schwaighofer, R. Werner, A. Gaitzenauer, B. Rashkova, et al., "Advanced β-Solidifying Titanium Aluminides–Development Status and Perspectives," in MRS Proceedings, 2013, pp. 3-16.

[41] D. Huber, R. Werner, H. Clemens, and M. Stockinger, "Influence of process parameter variation during thermo-mechanical processing of an intermetallic β-stabilized γ-TiAl based alloy," Materials Characterization, vol. 109, pp. 116-121, 2015.

[42] V. Raghavan, "Al-Ti (Aluminum-Titanium)," Journal of Phase Equilibria and Diffusion, vol. 26, pp. 171-172, 2005.

[43] A. Stark, Textur-und Gefügeentwicklung bei der thermomechanischen Umformung Nb-reicher [gamma]-TiAl-Basislegierungen [Gamma-TiAl-Basislegierungen]: Shaker, 2009.

[44] L. A. Yeoh, K.-D. Liss, A. Bartels, H. Chladil, M. Avdeev, H. Clemens, et al., "In situ high-energy X-ray diffraction study and quantitative phase analysis in the α+ γ phase field of titanium aluminides," Scripta Materialia, vol. 57, pp. 1145-1148, 2007.

[45] E. Menon, A. Fox, and R. Mahapatra, "Accurate determination of the lattice parameters of γ-TiAl alloys," Journal of materials science letters, vol. 15, pp. 1231-1233, 1996.

[46] G. Ghosh and M. Asta, "First-principles calculation of structural energetics of Al–TM (TM= Ti, Zr, Hf) intermetallics," Acta Materialia, vol. 53, pp. 3225-3252, 2005.

[47] T. Novoselova, S. Malinov, W. Sha, and A. Zhecheva, "High-temperature synchrotron X-ray diffraction study of phases in a gamma TiAl alloy," Materials Science and Engineering: A, vol. 371, pp. 103-112, 4/25/ 2004.

[48] N. Dubrovinskaia, M. Vennström, I. Abrikosov, R. Ahuja, P. Ravindran, Y. Andersson, et al., "Absence of a pressure-induced structural phase transition in Ti 3 Al up to 25 GPa," Physical Review B, vol. 63, p. 024106, 2000.

[49] S. Djanarthany, J.-C. Viala, and J. Bouix, "An overview of monolithic titanium aluminides based on Ti 3 Al and TiAl," Materials Chemistry and Physics, vol. 72, pp. 301-319, 2001.

[50] S. Sarkar, S. Datta, S. Das, and D. Basu, "Oxidation protection of gamma-titanium aluminide using glass–ceramic coatings," Surface and Coatings Technology, vol. 203, pp. 1797-1805, 3/25/ 2009.

[51] R. K. Bird, T. A. Wallace, and S. N. Sankaran, "Development of protective coatings for high-temperature metallic materials," Journal of spacecraft and rockets, vol. 41, pp. 213-220, 2004.

[52] M. Asta, D. de Fontaine, and M. Van Schilfgaarde, "First-principles study of phase stability of Ti–Al intermetallic compounds," Journal of materials research, vol. 8, pp. 2554-2568, 1993.

[53] F. Appel, P. Beaven, and R. Wagner, "Deformation processes related to interfacial boundaries in two-phase γ-titanium aluminides," Acta metallurgica et materialia, vol. 41, pp. 1721-1732, 1993.

[54] E. Bumps, H. Kessler, and M. Hansen, "Titanium-aluminum system," J. Metals (NY), vol. 4, 1952.

[55] S. Huang, E. Hall, and M. Gigliotti, "Rapidly Solidified Binary TiAl Alloys," in MRS Proceedings, 1986, p. 481.

[56] L. Huang, "Microstructural Evolution of TiAl-Intermetallic Alloys Containing W and B," 2005.

[57] S. R. Dey, A. Hazotte, and E. Bouzy, "Crystallography and phase transformation mechanisms in TiAl-based alloys – A synthesis," Intermetallics, vol. 17, pp. 1052-1064, 2009.

[58] S. Gebhard, F. Pyczak, and M. Göken, "Microstructural and micromechanical characterisation of TiAl alloys using atomic force microscopy and nanoindentation," Materials Science and Engineering: A, vol. 523, pp. 235-241, 2009.

[59] S. R. Dey, A. Hazotte, E. Bouzy, and S. Naka, "Development of Widmanstätten laths in a near-γ TiAl alloy," Acta Materialia, vol. 53, pp. 3783-3794, 2005.

[60] D. Hu, A. Huang, and X. Wu, "On the massive phase transformation regime in TiAl alloys: the alloying effect on massive/lamellar competition," Intermetallics, vol. 15, pp. 327-332, 2007.

[61] K.-D. Liss, A. Stark, A. Bartels, H. Clemens, T. Buslaps, D. Phelan, et al., "Directional Atomic Rearrangements During Transformations Between thea-andc-Phases in Titanium Aluminides," Advanced Engineering Materials, vol. 10, 2008.

[62] T. Schmoelzer, S. Mayer, C. Sailer, F. Haupt, V. Güther, P. Staron, et al., "In Situ Diffraction Experiments for the Investigation of Phase Fractions and Ordering Temperatures in Ti-44 at% Al-(3-7) at% Mo Alloys," Advanced Engineering Materials, vol. 13, pp. 306-311, 2011.

[63] T. Schmoelzer, K. D. Liss, P. Staron, S. Mayer, and H. Clemens, "The Contribution of High‐Energy X‐Rays and Neutrons to Characterization and Development of Intermetallic Titanium Aluminides," Advanced engineering materials, vol. 13, pp. 685-699, 2011.

[64] T. Schmoelzer, K. D. Liss, P. Staron, A. Stark, E. Schwaighofer, T. Lippmann, *et al.*, "The Contribution of High‐Energy X‐rays and Neutrons to Characterization and Development of Intermetallic Titanium Aluminides," Neutrons and Synchrotron Radiation in Engineering Materials Science: From Fundamentals to Applications, pp. 395-424, 2017.

[65] L. Lu, Y. Shen, X. Chen, L. Qian, and K. Lu, "Ultrahigh strength and high electrical conductivity in copper," Science, vol. 304, pp. 422-426, 2004.

[66] R. Ramanujan, "Phase transformations in γ based titanium aluminides," International Materials Reviews, vol. 45, pp. 217-240, 2000.

[67] A. Denquin and S. Naka, "Phase transformation mechanisms involved in two-phase TiAl-based alloys—I. Lambellar structure formation," Acta Materialia, vol. 44, pp. 343-352, 1996/01/01/ 1996.

[68] R. V. Ramanujan, "Phase transformations in γ based titanium aluminides," International Materials Reviews, vol. 45, pp. 217-240, 2000/06/01 2000.

[69] S. Zghal, S. Naka, and A. Couret, "A QUANTITATIVE TEM ANALYSIS OF THE LAMELLAR MICROSTRUCTURE IN TiAl BASED ALLOYS," Acta Materialia, vol. 45, pp. 3005-3015, 1997/07/01/ 1997.

[70] C. Teng, "Phase Field Simulation of the Nucleation and Growth of the Lamellar Microstructure in TiAl Alloys," Northeastern University, 2012.

[71] S. Kim, H. Lee, M. Oh, and D. Wee, "Effects of the variation in α-phase volume fraction on the thermal stability of TiAl alloys with a lamellar microstructure," Journal of materials science, vol. 39, pp. 6929-6935, 2004.

[72] K. Muraleedharan, L. Rishel, M. De Graef, A. Cramb, T. Pollock, and G. Gray, "Structural Intermetallics," TMS, Warrendale, PA, vol. 215, 1997.

[73] V. Küstner, M. Oehring, A. Chatterjee, V. Güther, H. Brokmeier, H. Clemens, et al., "An investigation of microstructure formation during solidification of gamma titanium aluminide alloys," Gamma titanium aluminides, pp. 89-96, 2003.

[74] M. DEGRAEF, N. Biery, L. RISHEL, T. Pollock, and A. CRAMB, "Gamma Titanium Aluminides 1999," The Minerals, Metals & Materials Society, Warrendale, PA, 1999) p, vol. 247, 1999.

[75] M. Yoo and M. Wuttig, "Twinning in advanced materials," TMS, Warrendale, PA, p. 97, 1994.

[76] J. W. Christian and S. Mahajan, "Deformation twinning," Progress in materials science, vol. 39, pp. 1-157, 1995.

[77] S. Court, V. Vasudevan, and H. Fraser, "Deformation mechanisms in the intermetallic compound TiAl," Philosophical Magazine A, vol. 61, pp. 141-158, 1990.

[78] J. E. Schnabel and S. Bargmann, "Accessing Colony Boundary Strengthening of Fully Lamellar TiAl Alloys via Micromechanical Modeling," Materials (Basel), vol. 10, Aug 3 2017.

[79] K.-D. Liss, A. Bartels, H. Clemens, S. Bystrzanowski, A. Stark, T. Buslaps, et al., "Recrystallization and phase transitions in a γ-TiAl-based alloy as observed by ex situ

and in situ high-energy X-ray diffraction," Acta Materialia, vol. 54, pp. 3721-3735, 2006.

[80] H. F. Chladil, H. Clemens, G. A. Zickler, M. Takeyama, E. Kozeschnik, A. Bartels, et al., "Experimental studies and thermodynamic simulation of phase transformations in high Nb containing γ-TiAl based alloys," International Journal of Materials Research, vol. 98, pp. 1131-1137, 2007.

[81] H. F. Chladil, H. Clemens, H. Leitner, A. Bartels, R. Gerling, and W. T. Marketz, "Experimental Studies of Phase Transformations in a Carbon Containing Ti‐45Al‐7.5 Nb Alloy and Related Thermodynamic Simulations," Advanced Engineering Materials, vol. 7, pp. 1131-1134, 2005.

[82] H. Chladil, H. Clemens, H. Leitner, A. Bartels, R. Gerling, F.-P. Schimansky, et al., "Phase transformations in high niobium and carbon containing γ-TiAl based alloys," Intermetallics, vol. 14, pp. 1194-1198, 2006.

[83] A. Grytsiv, P. Rogl, H. Schmidt, and G. Giester, "Constitution of the ternary system Al-Ru-Ti (Aluminum-Ruthenium-Titanium)," Journal of phase equilibria, vol. 24, pp. 511-527, 2003.

[84] U. Kattner and W. Boettinger, "Thermodynamic calculation of the ternary Ti・Al・Nb system," Materials Science and Engineering: A, vol. 152, pp. 9-17, 1992.

[85] C. Servant and I. Ansara, "Thermodynamic assessment of the Al‐Nb‐Ti system," Berichte der Bunsengesellschaft für physikalische Chemie, vol. 102, pp. 1189-1205, 1998.

[86] C. Servant and I. Ansara, "Thermodynamic modelling of the order-disorder transformation of the orthorhombic phase of the Al-Nb-Ti system," Calphad, vol. 25, pp. 509-525, 2001.

[87] W. J. Z. G. L. Chen, Z. C. Liu, S. J. Li, Y.-W. Kim, "Microstructure and properties of high-Nb containing TiAl-base alloys, Gamma Titanium Aluminides," TMS, Warrendale, PA, pp. 371-380, 1999.

[88] Y. Ma, "Fabrication of gamma titanium aluminide alloys by gas tungsten arc welding-based additive layer manufacturing," 2015.

[89] R. E. Schafrik, "Dynamic elastic moduli of the titanium aluminides," Metallurgical and Materials Transactions A, vol. 8, pp. 1003-1006, 1977.

[90] B. Liu, Y. Liu, Y. P. Li, W. Zhang, and A. Chiba, "Thermomechanical characterization of β-stabilized Ti–45Al–7Nb–0.4W–0.15B alloy," Intermetallics, vol. 19, pp. 1184-1190, 8// 2011.

[91] Y. He, R. Schwarz, T. Darling, M. Hundley, S. Whang, and Z. Wang, "Mater Sci Eng 1997," A239–240, vol. 157.

[92] B. Srinivasarao, A. Zhilyaev, R. Muñoz-Moreno, and M. Pérez-Prado, "Effect of high pressure torsion on the microstructure evolution of a gamma Ti–45Al–2Nb–2Mn–0.8 vol% TiB2 alloy," Journal of Materials Science, vol. 48, pp. 4599-4605, 2013.

[93] L. Löber, F. P. Schimansky, U. Kühn, F. Pyczak, and J. Eckert, "Selective laser melting of a beta-solidifying TNM-B1 titanium aluminide alloy," Journal of Materials Processing Technology, vol. 214, pp. 1852-1860, 2014.

[94] F. Appel, M. Oehring, and J. Paul, "A novel in situ composite structure in TiAl alloys," Materials Science and Engineering: A, vol. 493, pp. 232-236, 2008.

[95] C. Zambaldi, F. Roters, and D. Raabe, "Analysis of the plastic anisotropy and pre-yielding of (γ/α2)-phase titanium aluminide microstructures by crystal plasticity simulation," Intermetallics, vol. 19, pp. 820-827, 2011.

[96] Y.-W. Kim, "Ordered intermetallic alloys, part III: gamma titanium aluminides," Jom, vol. 46, pp. 30-39, 1994.

[97] W.H. Bragg, W.L. Bragg. "The Reflexion of X-rays by Crystals". Proc. R. Soc. Lond. A. vol. 88, pp. 428–38.,1913.doi: 10.1098/rspa.1913.0040.

[98] K.-D. Liss, A. Bartels, A. Schreyer, and H. Clemens, "High-energy X-rays: a tool for advanced bulk investigations in materials science and physics," *Textures and Microstructures*, vol. 35, pp. 219-252, 2003.

[99] K.-D. Liss, Y. Kun. Material Science and Engineering A. vol. 528, pp. 11, 2010.

[100] W. Reimers, A. R. Kaysser-Pyzalla, A. Schreyer, and H. Clemens, Neutrons and synchrotron radiation in engineering materials science: from fundamentals to material and component characterization: John Wiley & Sons, 2008.

[101] T. Schmoelzer, K.-D. Liss, G. A. Zickler, I. J. Watson, L. M. Droessler, W. Wallgram, et al., "Phase fractions, transition and ordering temperatures in TiAl–Nb–Mo alloys: An in-and ex-situ study," Intermetallics, vol. 18, pp. 1544-1552, 2010.

[102] M.J Berger., J.H. Hubbell , Seltzer, S.M., Coursey, J.S. and Zucker, D.S. XCOM: Photon Cross Sections Database. National Institute of Standards and Technology, 1998.

[103] S. Bystrzanowski, A. Bartels, H. Clemens, R. Gerling, F. Schimansky, G. Dehm, et al., "Creep behaviour and related high temperature microstructural stability of Ti–46Al–9Nb sheet material," Intermetallics, vol. 13, pp. 515-524, 2005.

[104] P. Erdely, T. Schmoelzer, E. Schwaighofer, H. Clemens, P. Staron, A. Stark, et al., "In Situ Characterization Techniques Based on Synchrotron Radiation and Neutrons Applied for the Development of an Engineering Intermetallic Titanium Aluminide Alloy," Metals, vol. 6, p. 10, 2016.

[105] I. J. Watson, K.-D. Liss, H. Clemens, W. Wallgram, T. Schmoelzer, T. C. Hansen, et al., "In Situ Characterization of a Nb and Mo Containing$\hat{I}^3$-TiAl Based Alloy Using Neutron Diffraction and High-Temperature Microscopy," Advanced Engineering Materials, vol. 11, pp. 932-937, 2009.

[106] S. Kabra, K. Yan, S. Mayer, T. Schmoelzer, M. Reid, R. Dippenaar, et al., "Phase transition and ordering behavior of ternary Ti–Al–Mo alloys using in-situ neutron diffraction," International Journal of Materials Research, vol. 102, pp. 697-702, 2011.

[107] K.-D. Liss, et al., Hydrostatic Compression Behavior and High-Pressure Stabilized β-Phase in γ-Based Titanium Aluminide Intermetallics. Metals, vol. **6,** pp. 165, 2016.

[108] T. Hattori, H. Saitoh, H. Kaneko, Y. Okajima, K. Aoki, W. Utsumi. "Does Bulk Metallic Glass of Elemental Zr and Ti Exist Phys," Rev. Lett. vol. 96, 255504, 2006 https://doi.org/10.1103/PhysRevLett.96.255504

[109] F. Ducastelle, "Order and phase stability in alloys," 1991.

[110] M. Hoelzel, R. Gilles, M. Schlapp, H. Boysen, and H. Fuess, "Monte Carlo simulations of various instrument configurations of the new structure powder diffractometer (SPODI)," Physica B: Condensed Matter, vol. 350, pp. E671-E673, 2004.

[111] M. Paściak, A. Heerdegen, D. Goossens, R. Whitfield, A. Pietraszko, and T. Welberry, "Assessing Local Structure in PbZnNbO Using Diffuse Scattering and Reverse Monte Carlo Refinement," Metallurgical & Materials Transactions. Part A, vol. 44, pp. 87-93, 2013.

[112] T. Welberry, M. Gutmann, H. Woo, D. Goossens, G. Xu, C. Stock, et al., "Single-crystal neutron diffuse scattering and Monte Carlo study of the relaxor ferroelectric PbZn1/3Nb2/3O3 (PZN)," Journal of applied crystallography, vol. 38, pp. 639-647, 2005.

[113] A. R. Denton and N. W. Ashcroft, "Vegard's law," Physical review A, vol. 43, pp. 3161, 1991.

[114] K.-D. Liss, R. E. Whitfield, W. Xu, T. Buslaps, L. A. Yeoh, X. Wu, et al., "In situ synchrotron high-energy X-ray diffraction analysis on phase transformations in Ti–Al alloys processed by equal-channel angular pressing," Journal of synchrotron radiation, vol. 16, pp. 825-834, 2009.

[115] K. Yan, D. Carr, S. Kabra, M. Reid, A. Studer, R. Harrison, et al., "In-situ characterization of lattice structure evolution during phase transformation of Zr-2.5 Nb," World J. Eng, vol. 7, p. P422, 2010.

[116] R. D. Shull and J. P. Cline, "High temperature X-ray diffractometry of Ti-Al alloys," in Materials Chemistry at High Temperatures, ed: Springer, 1990, pp. 95-117.

[117] D. Chateigner, Combined Analysis, 2010.

[118] E. Schneider and V. Hauk, "Structural and residual stress analysis by nondestructive methods," Amsterdam: Elsevier, pp. 522-63, 1997.

[119] L. Daniel, D. A. Hall, and P. J. Withers, "A multiscale modelling analysis of the contribution of crystalline elastic anisotropy to intergranular stresses in ferroelectric materials," Journal of Physics D: Applied Physics, vol. 47, p. 325303, 2014.

[120] R. Sarkar, C. Ebner, J. Rajagopalan, and C. Rentenberger, "Study of anelastic behavior of amorphous TiAl by atomic-level elastic strain measurement during in-situ TEM straining," pp. 706-707, 2016.

[121] F. Froes, C. Suryanarayana, G.-H. Chen, A. Frefer, and G. R. Hyde, "Nanostructure processing for titanium-based materials," JOM Journal of the Minerals, Metals and Materials Society, vol. 44, pp. 26-29, 1992.

Chapter 3. Experimental

A schematic outline of the experimental equipment and procedures of this doctoral thesis are shown in Figure 3.1. This chapter introduces the experimental methods and instruments related to the current study. Different types of γ-based Ti-Al alloys used in this study were processed by methods such as directional solidification, powder metallurgical techniques and high pressure torsion (HPT). Microstructure, lattice evolution and phase transitions were examined by scanning electron microscopy (SEM), Electron Backscatter Diffraction (EBSD), X-ray diffraction (XRD), *in-situ* high-energy XRD (HEXRD), neutron diffraction and high-temperature laser-scanning confocal microscopy (HTLSCM). Hardness measurements were applied to assess mechanical properties. The X-ray and neutron diffraction patterns were analyzed using Rietveld Method by the *Material Analysis Using Diffraction* (MAUD) software. The detailed experimental procedures and the research outcomes are described in the following chapters.

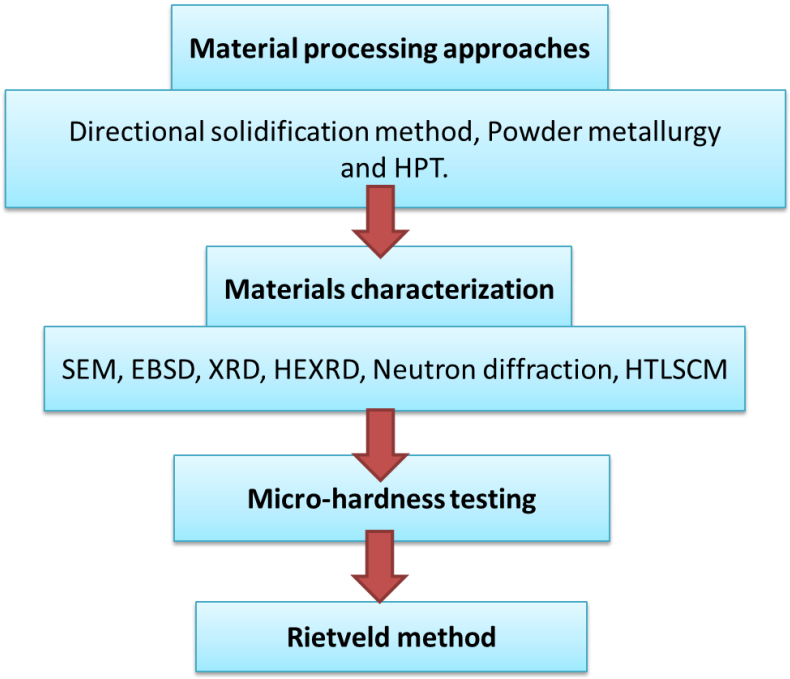

Figure 3.1 The flowchart of the experimental work.

3.1 Material processing approaches

Following a study of these relatively simple structures of polysynthetically twinned Ti-Al crystals, γ-based Ti-Al alloys were produced by powder metallurgical techniques, while the specimens were processed by the use of high-pressure torsion technology. Aiming to study the microstructural development and phase transformation of γ-based Ti-Al alloys under different conditions, initial experiments were conducted on polysynthetically twinned Ti-Al crystals, with a single lamellar colony structure.

3.1.1 Directional solidification methods

Directional solidification techniques [1] are used to restrain the growth of horizontal grain boundaries and to improve the required mechanical properties along the loading axis. Figure 3.2 shows the directional solidification process by an optical floating zone technique, which was used for growing the PST crystals used in this study. It was heated by light produced by a xenon lamp, focused by ellipsoidal lenses onto the specimen. By using seed crystals, the rod-like PST crystals in this study were grown by this technique [2, 3].

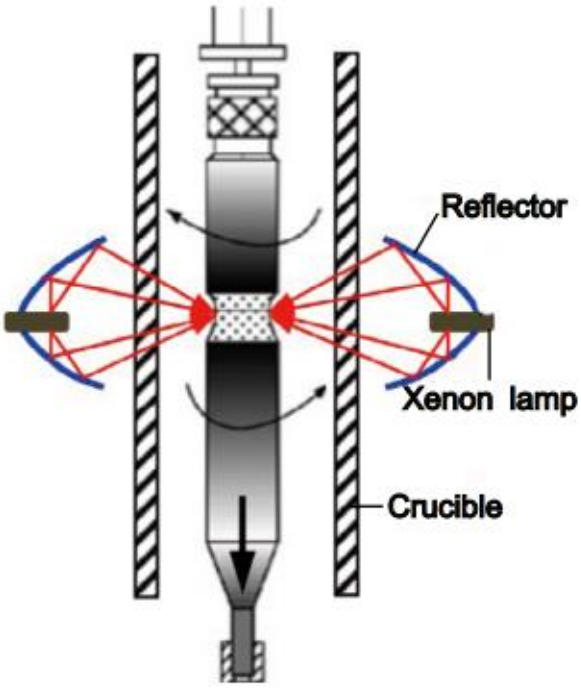

Figure 3.2 Directional solidification process by optical floating zone technique [2].

3.1.2 Powder Metallurgy processing of Ti-Al alloys

The Ti-45Al-7.5Nb-(0.25/0.5C) specimens used in this study have been manufactured by GKSS Research Center and provided through a research project at Hamburg University of Technology [4]. For better interpretation of outcomes in the present study, it is pertinent to briefly refer to the pre-alloyed powder technology, one of the powder metallurgical techniques, used to produce the Ti-Al alloys, which have been supplied for this study. Gas atomization process was followed by hot isostatic pressing (HIP) at 200 MPa and a temperature of 1553 K for 2 h as schematically shown in Figure 3.3.

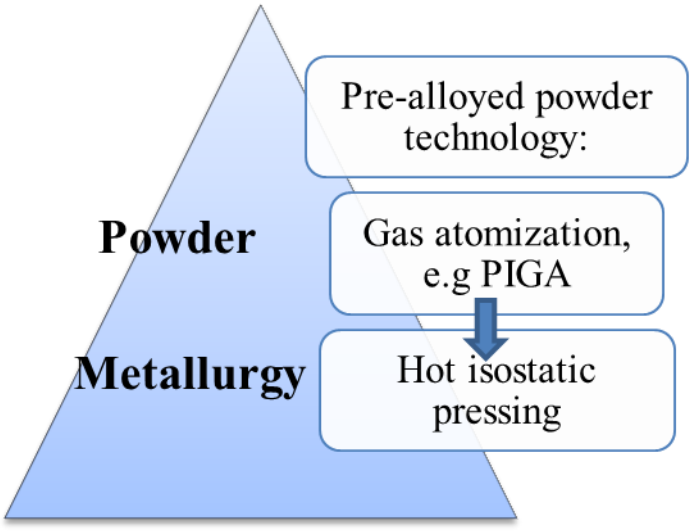

Figure 3.3 A schematic outline of the powder metallurgical processing route used to fabricate the Ti-Al alloys in this study.

The pre-alloyed “atomized” Ti-Al powder was produced by a plasma-melting, induction-guiding gas atomization (PIGA) technique [4, 5], schematically illustrated in Figure 3.4. A plasma torch was used to melt the metallic raw materials in a cold crucible under an inert argon gas atmosphere [4]. Hot isostatic pressing was used for consolidation and densification of the metallic powder.

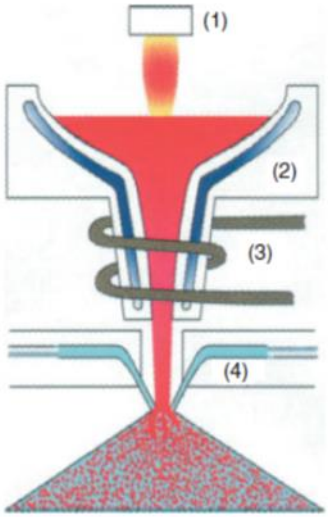

Figure 3.4 Schematic representations of the plasma melting induction guiding gas atomization technique: (1) Plasma Torch (2) Cold copper crucible (3) Induction heated cold copper funnel (4) Gas Nozzle, reproduced from [5].

3.1.3 High pressure torsion

The consolidated and densified Ti-45Al-7.5Nb alloys were further processed by a modern high-pressure torsion technique in order to refine the microstructure. Specimens were machined into rods and cut into disks (10 mm diameter and 0.85 mm thick). As shown in Figure 3.5, they were then subjected to a compressive force of 480 kN and continuous torsionally strained by a quasi-constrained HPT facility at Hanyang University, Korea [6, 7]. The lower anvil is rotated in one direction at a fixed speed of 1 rpm, which imposes torsional strain to the samples.

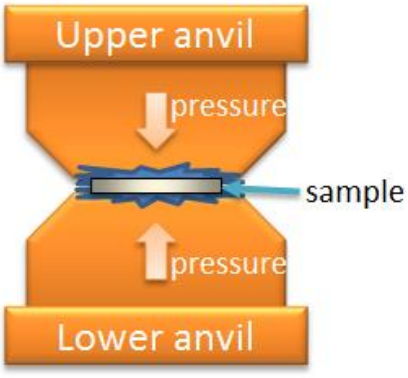

Figure 3.5 Schematic illustration of a quasi-constrained HPT facility.

3.2 Characterization techniques

Before observations were made under optical and confocal microscopes, specimens were ground and polished in the Struers Tegrapal-21 facility shown in Figure 3.6 and then metallographically prepared according to conventional polishing procedures for Ti-Al alloys [8]. A more detailed outline of the grinding and polishing procedure is shown in Table 3.1.

Table 3.1 Grinding and polishing procedure for HPT.

Procedure	Surface	Time, minutes	solution
Grinding	1200# SiC	4	Water
Polishing	15 μm MD-Pan cloth	15	Water-based lubricant
Polishing	0.25 μm MD-Chem cloth	10	50% OPS*

* OPS is short for oxide polishing suspensions.

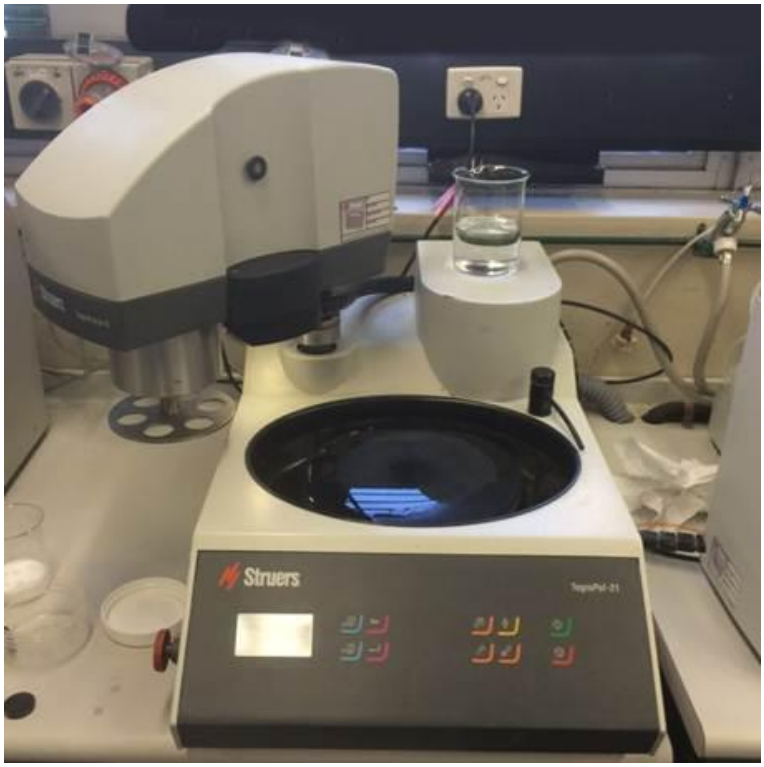

Figure 3.6 The Struers Tegrapal-21 automatic grinder and polisher.

For the preparation of specimens for EBSD characterization, polishing was done in a 90 ml colloidal silica and 10 ml hydrogen peroxide solution (sigma-aldrich^{R}). The Struers Tegrapal-

21 automatic grinder and polisher was set to the non-ferrous and chem ops with 25 N normal load and 150 rpm for 6 min. Then the residue was immediately very lightly "brushed" with soapy water, followed by sonication in ethanol for approximately 10 min, and then dried in air.

3.2.1 Scanning electron microscopy (SEM)

A JEOL JBM-7001 SEM, shown in Figure 3.7(a) was used in this study. Energy Dispersive Spectroscopy (EDS) was employed to conduct compositional analysis under standardless mode in the scanning (SEM) mode. The average grain size was determined by using the line intercept method on SEM images.

3.2.2 Electron Backscatter Diffraction (EBSD)

Back-scattered electron diffraction studies were conducted on a Zeiss® Ultra Plus™ SEM, coupled with an Oxford Instruments® Nordlys™ electron backscatter diffraction (EBSD) system, shown in Figure 3.7 (b). The EBSD data was collected using the Aztec™ software, and analysed using the Channel 5™ software.

Typical output, a crystal orientation map, of such EBSD is shown in Figure 3.8. By the method of inverse pole figure, different colour represents different crystal axis. For example, the blue means the [111] axis whereas green is [101]. It is clearly to see how the crystals oriented in the whole sample from the EBSD map.

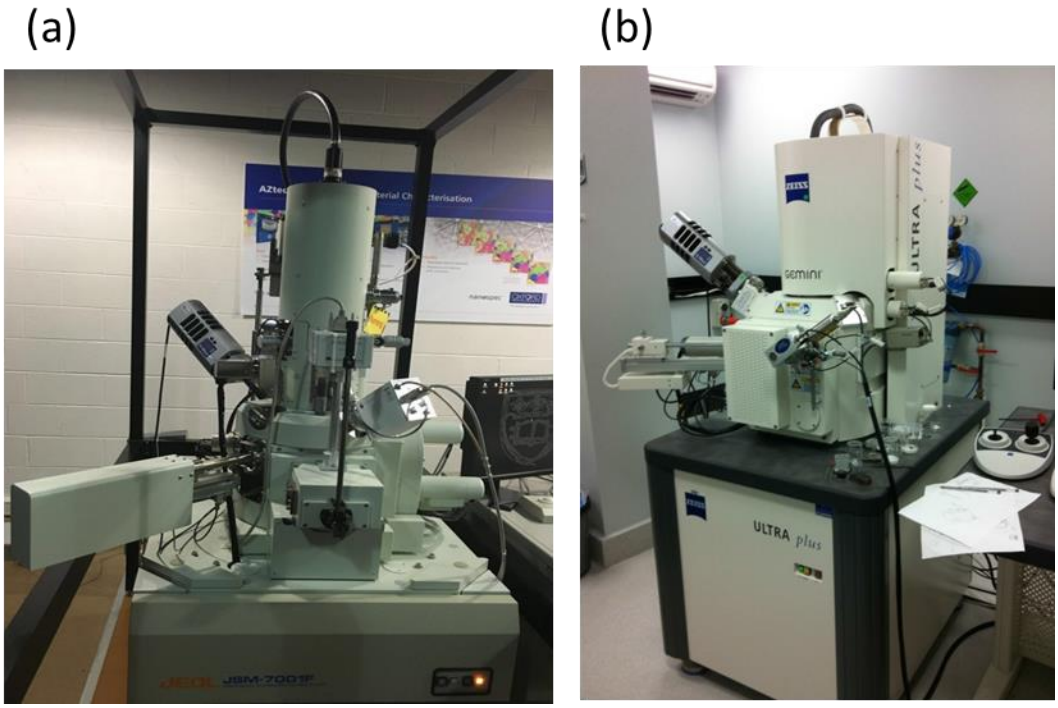

Figure 3.7: (a) JEOL JBM-7001 scanning electron microscopy (SEM) (b) Zeiss® Ultra Plus™ scanning electronic microscope (SEM).

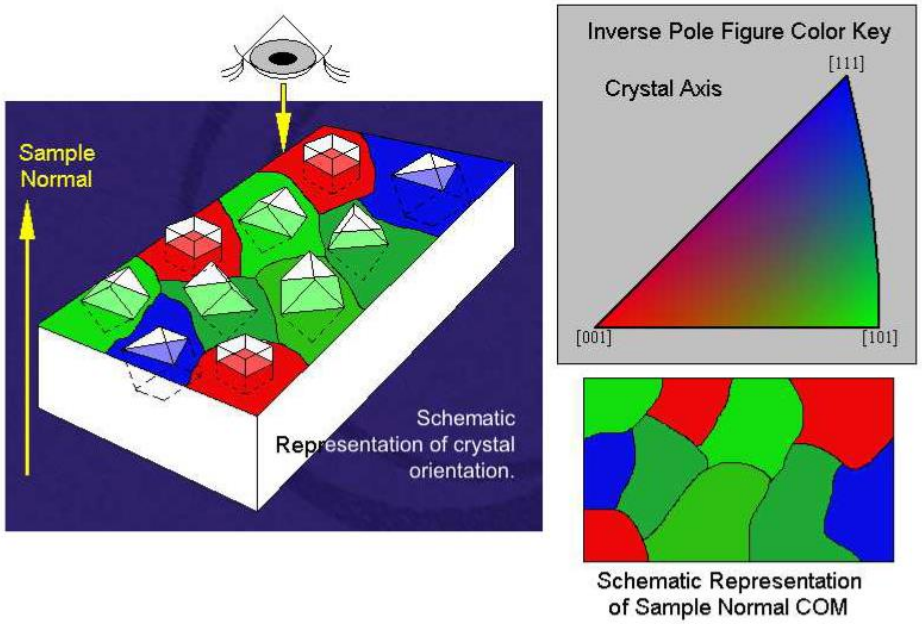

Figure 3.8 Schematic EBSD map and inverse pole figures, reproduced from the reference [9].

3.2.3 X-Ray diffraction (XRD)

Figure 3.9(a) and (b) show a GBC MMA X-Ray diffractometer using monochromatic Cu-K_α radiation and an Ultima IV (Rigaku, Japan) X-ray diffractometer which were used in this conventional X-ray diffraction study.

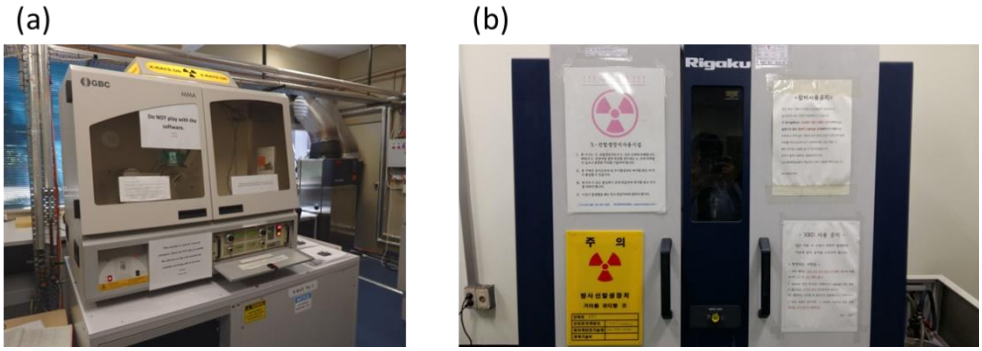

Figure 3.9: (a) GBC MMA X-ray diffractometer; (b) Ultima III (Rigaku, Japan) X-ray diffractometer.

3.2.4 High-energy and energy-dispersive X-ray diffraction

In comparison to traditional XRD, high-energy XRD can penetrate much deeper [10, 11]. However since the HEXRD beam is highly collimated (~1 mm^2), information can only be obtained from a small area [12], compared with conventional XRD. The HEXRD facility involved in this study is the European Synchrotron Radiation Facility (ESRF) in Grenoble, as shown in Figure 3.10(a). On the other hand, energy-dispersive X-ray diffraction methods have been developed in recent years. Figure 3.11 (b) shows the modern synchrotron source SPring-8 [13] with Kawai-type multi-anvil press (SPEED-Mk.II), used for such experiments. More details of how to use these facilities for this study are described below.

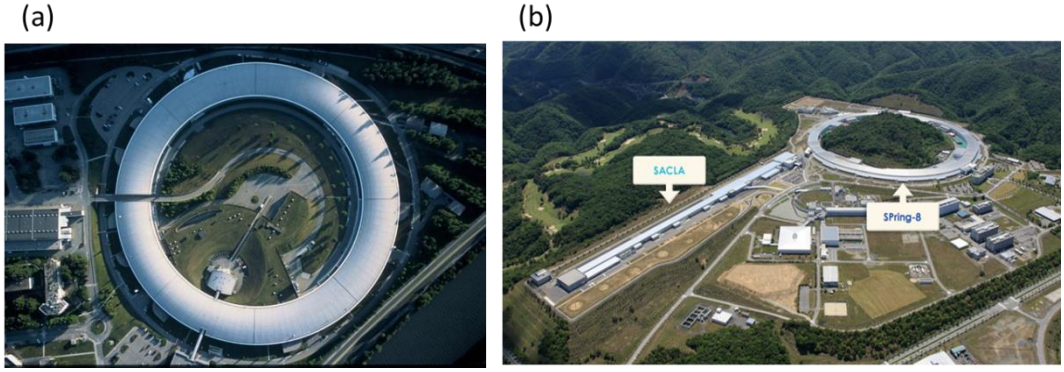

Figure 3.10 (a) The top view of the European Synchrotron Radiation Facility (ESRF) in Grenoble, and (b) the panoramagram of the modern synchrotron SPring-8.

In 2007, Yeoh *et al.* [14] have done *in-situ* HEXRD experiments during heating under atomospheric pressure at the ESRF. Beamline ID15B was utilized, with 6 GeV electron-energy rings to provide undulator radiation. The energy of incident beam is 89.05 keV using

silicon monochromator, with wave number 45.12 Å. The incident beam impinges onto the polycrystalline sample with transmission mode, is diffracted into Debye-Scherrer cones and are recorded by a 2D detector, as shown in Figure 3.11[15].

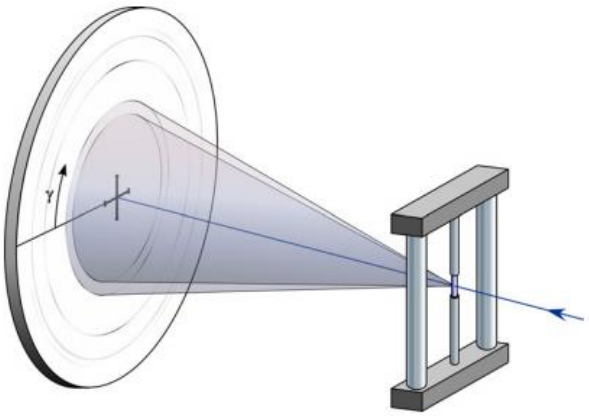

Figure 3.11 (a) Typical experimental set-up. A fine synchrotron beam impinges from the right to the polycrystalline sample, recording diffraction patterns on a 2D detector, reproduced by Liss *et al.* [15].

An energy dispersive experiment was conducted with fixed angle by the polychromatic photons, at Spring-8, by Liss *et al.* [16]. A pressure cell within an integrated resistance-heating furnace was designed in order to provide the capability of heating the specimen under high pressure. The facility is schematically shown in Figure 3.12, but a more comprehensive account of the experimental details has recently been provided by Liss *et al.* [16]

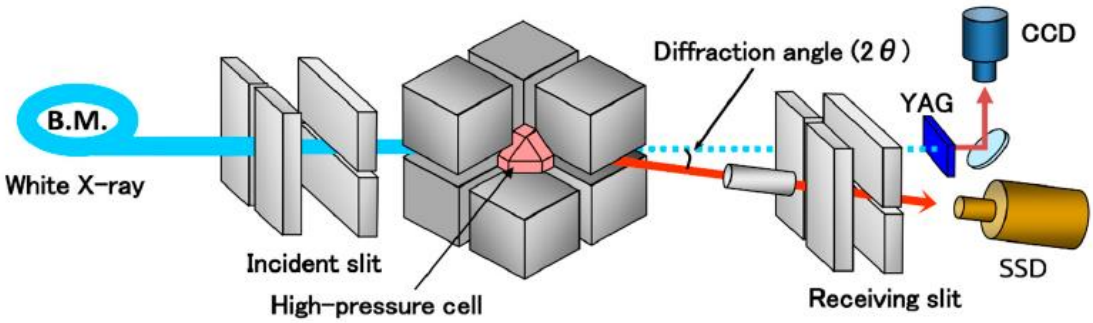

Figure 3.12 The BL04B1 beamline set-up with high pressure cell, based on and reproduced from [16].

3.2.5 Neutron diffraction

In neutron diffraction, the incident neutron beam has a much larger attenuation length than X-rays and hence, information can be obtained from a bulk volume rather than merely the surface. Moreover, neutrons react with the nucleus, which renders neutron diffraction particularly suitable to study the order-disorder transitions in Ti-Al.

3.2.5.1 WOMBAT powder diffractometer

The high intensity neutron powder diffractometer, WOMBAT [17], at the Australian Nuclear Science and Technology organisation (ANSTO), is employed in this study and shown in Figure 3.13. The wavelength of 2.42 or 1.54 Å can be selected by a Ge-311 or a Ge-511 monochromator under the take-off angle 2θ of 90^{o}. A true two-dimensional, position sensitive detector of this facility covers 120^{o} in-plane and 15^{o} out-of-plane [18]. The area is binned into 968 × 128 pixels, each with ~microseconds of intrinsic time response. With this two-dimensional detector, diffraction patterns have been collected in as little as 18.2s exposure time per frame [17, 19].

Figure 3.13 The high intensity powder diffractometer WOMBAT.

3.2.5.2 C-shaped Eulerian cradle

The Huber 512.5 Eulerian cradle is used for texture measurement, as shown in Figure 3.14. It is a four-circle setup with φ-plane and χ-plane vertical each other and its detailed angle conventions are introduced in the next paragraph. It can be used in both X-ray and neutron diffraction field and also can set up with the closed cycle refrigerator to reach temperatures of 10 K to 300 K. A full pole figure of a sample (5 mm^3) was mapped within 15 min approximately [20]. In this work, it was used within WOMBAT to measure crystallographic texture and map reciprocal space.

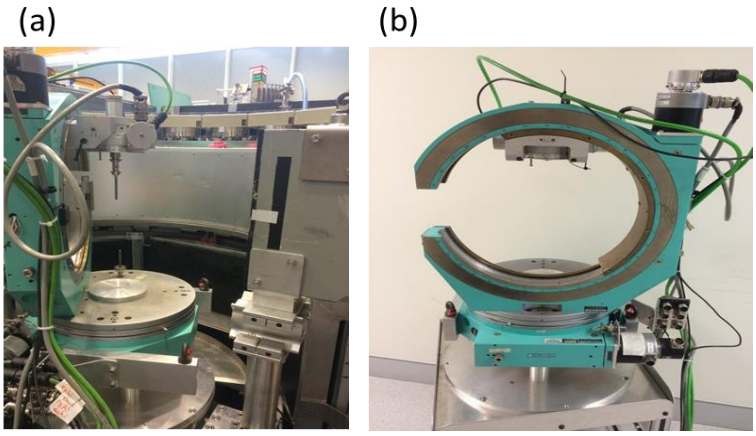

Figure 3.14 The Euler Cradle for texture measurement (a) within WOMBAT and (b) on its own independently.

Figure 3.15(a) shows the full view of Eulerian Cradle with the diffraction angle ω, the tilt angle χ and the sample rotation φ. The rotation conventions in the sample coordinate system, are shown in Figure 3.15(b). ω, is rotation around vertical axis of the instrument. 2θ is the angle of the diffracted to the incident beam, rotation is same as ω; χ is the tilt angle of the sample, rotation around Eulerian Cradle axis; while φ is the sample rotation angle, which is around Z_i (the sample normal) and η represents the azimuthal angle of the diffraction ring mapped to the detector.

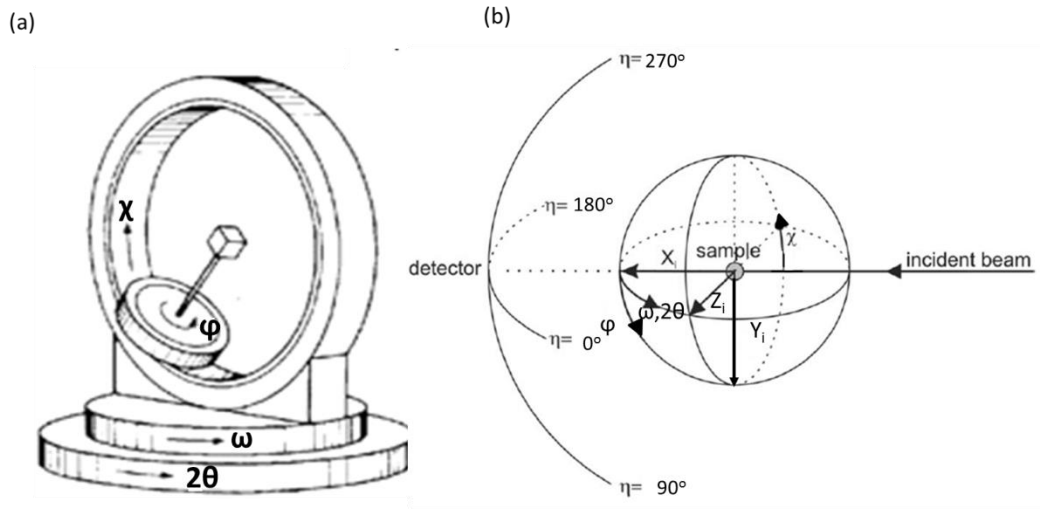

Figure 3.15 (a) The Eulerian Cradle (right handed system), based on the reference [23], (b) The angle convention, showing the sample tilt (χ) and rotation (φ) angles, the diffraction angle (ω) and the detector orientation angle (η) in the instrument coordinate system (*Xi*, *Yi*, *Zi*), reproduced from [22].

3.2.6 High-Temperature Laser-Scanning Confocal Microscopy

In-situ observations in a high-temperature laser-scanning confocal microscope provide useful information with respect to the morphology and kinetics of phase transformations in real time and at high resolution [24, 25]. The high-temperature laser-scanning confocal microscopy used in this study in the University of Wollongong is shown in Figure 3.16. Laser light is focused by an objective lens on to the specimen surface and the reflected beam is focused onto a photo detector through a beam splitter, providing a high-resolution image. Magnifications up to 1350X at a resolution of 0.25 μm can be obtained, using a He-Ne laser with a wavelength of 632.8 nm and a beam diameter of 0.5 μm. Specimen holders consist of 5 or 10 mm diameter round platinum holders or a $12 \times 4 \times 3\ mm^3$ rectangular platinum holder [26].

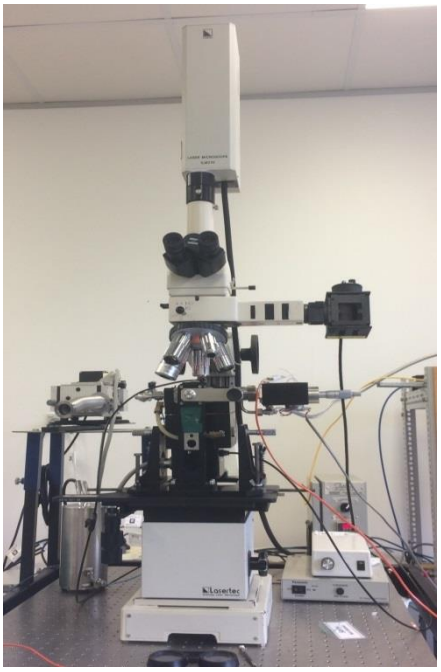

Figure 3.16 High temperature laser scanning confocal microscopy, at the University of Wollongong.

3.3 Micro-hardness testing

Micro-hardness testing was performed on a DuraScan 70 automatic hardness tester using the Vickers hardness method [27]. The instrument, LECO M-400-H1, at University of Wollongong, is shown in Figure 3.17.

Figure 3.17 The micro-hardness instrument LECO M-400-H1.

3.4 Rietveld Method

Since the Rietveld refinement technique [28-30] has been used in this study for the characterization of crystalline material, it is pertinent to briefly refer to the basic principles used in this technique. Rietveld refinement utilized a least square method to minimize the difference between the experimental data and the corresponding calculated values so that the whole calculated line profile matches the measured one. The calculated intensity of diffraction can be expressed as:

$$I_i^{calc}(\chi,\theta) = bkg_i + I_0 L_P(2\theta_i) A_i(\chi,\theta) \sum_{n=1}^{N_{phases}} f_n \sum_{k=1}^{N_{hkl}} m_{h;n} \left|F_{h;n}\right|^2 S_{h;n}(2\theta_i - 2\theta_{h;n}) P_{h;n}(\chi,\theta)$$

Where, $I_i^{calc}(\chi,\theta)$ represents the calculated intensity of point i at the sample position(χ,θ), bkg_i is the background and I_0 the incident beam intensity. $L_P(2\theta_i)$ is the Lorentz polarization factor at the 2θ point i. $A_i(\chi,\theta)$ is the absorption factor at the point i for the sample position (χ,θ). $m_{h;n}$, $F_{h;n}$, $S_{h;n}$ and $P_{h;n}$ are multiplicity, structural factor, profile shape function and texture pole figure factors of the diffraction plane h for the phase n. 2θ is the diffraction angle.

The MAUD (*Material Analysis Using Diffraction*) software, developed by Lutterotti *et al.* [31] is one of the powerful analytical Rietveld analysis tools. Inside there are several parameters, through adjusting them to get the calculated pattern agreeing well with the measured one. For example, the lattice parameters are related to the peak shifts while the crystallite size and micro-strain affect the width of peak. MAUD was used for analyzing the traditional XRD, HEXRD and neutron diffraction patterns in the present study.

3.5 References

[1] L. T. Su Yanqing, Li Xinzhong, Chen Ruirun, Ding Hongsheng, Guo Jingjie, and Fu Hengzhi, "Lamellar orientation control in directionally solidified TiAl intermetallics," sicence report, vol. 11, 2014.

[2] D. R. Johnson, H. Inui, S. Muto, Y. Omiya, and T. Yamanaka, "Microstructural development during directional solidification of α-seeded TiAl alloys," Acta Materialia, vol. 54, pp. 1077-1085, 2006.

[3] Y. Rui, "DIRECTIONAL SOLIDIFICATION OF Ti-43Al-3Si ALLOYS IN AN OPTICAL FLOATING ZONE FURNACE," Acta Metall, vol. 48, pp. 235-239, 2012-02-11 2012.

[4] R. Gerling, H. Clemens, and F. P. Schimansky, "Powder Metallurgical Processing of Intermetallic Gamma Titanium Aluminides," Advanced Engineering Materials, vol. 6, pp. 23-38, 2004.

[5] R. Gerling, F. Schimansky, A. Stark, A. Bartels, H. Kestler, L. Cha, et al., "Microstructure and mechanical properties of Ti 45Al 5Nb+ (0–0.5 C) sheets," Intermetallics, vol. 16, pp. 689-697, 2008.

[6] A. P. Zhilyaev and T. G. Langdon, "Using high-pressure torsion for metal processing: Fundamentals and applications," Progress in Materials Science, vol. 53, pp. 893-979, 8// 2008.

[7] M. Kawasaki and T. G. Langdon, "The significance of strain reversals during processing by high-pressure torsion," Materials Science and Engineering: A, vol. 498, pp. 341-348, 12/20/ 2008.

[8] Y. Ma, "Fabrication of gamma titanium aluminide alloys by gas tungsten arc welding-based additive layer manufacturing," 2015.

[9] K. Dicks. (2003). Introduction to EBSD. Available: http://www.ebsd.com/

[10] W. D. Callister and D. G. Rethwisch, Materials science and engineering: an introduction vol. 7: Wiley New York, 2007.

[11] K.-D. Liss, A. Bartels, A. Schreyer, and H. Clemens, "High-energy X-rays: a tool for advanced bulk investigations in materials science and physics," *Textures and Microstructures,* vol. 35, pp. 219-252, 2003.

[12] K. Yan, "In-situ characterization by high-energy x-ray and neutron diffraction of micro-structural evolution of selected materials during thermo-mechanical processing," 2012.

[13] T. Katsura, K.-i. Funakoshi, A. Kubo, N. Nishiyama, Y. Tange, Y.-i. Sueda, et al., "A large-volume high-pressure and high-temperature apparatus for in situ X-ray observation,'SPEED-Mk. II'," Physics of the Earth and Planetary Interiors, vol. 143, pp. 497-506, 2004.

[14] L. A. Yeoh, K.-D. Liss, A. Bartels, H. Chladil, M. Avdeev, H. Clemens, et al., "In situ high-energy X-ray diffraction study and quantitative phase analysis in the α+ γ phase field of titanium aluminides," Scripta Materialia, vol. 57, pp. 1145-1148, 2007.

[15] K.-D. Liss and K. Yan, "Thermo-mechanical processing in a synchrotron beam," Materials Science and Engineering: A, vol. 528, pp. 11-27, 2010.

[16] K.-D. Liss, K.-I. Funakoshi, R. Dippenaar, Y. Higo, A. Shiro, M. Reid, et al., "Hydrostatic Compression Behavior and High-Pressure Stabilized β-Phase in γ-Based Titanium Aluminide Intermetallics," Metals, vol. 6, p. 165, 2016.

[17] A. J. Studer, M. E. Hagen, and T. J. Noakes, "Wombat: The high-intensity powder diffractometer at the OPAL reactor," Physica B: Condensed Matter, vol. 385, pp. 1013-1015, 2006.

[18] A. P. Hammersley, S. O. Svensson, M. Hanfland, A. N. Fitch, D. Häusermann, "Two-dimensional detector software: from real detector to idealised image or two-theta scan," High Pressure Res, vol 14 pp. 235-248, 1996.

[19] T. Schmoelzer, K.-D. Liss, G. A. Zickler, I. J. Watson, L. M. Droessler, W. Wallgram, et al., "Phase fractions, transition and ordering temperatures in TiAl–Nb–Mo alloys: An in-and ex-situ study," Intermetallics, vol. 18, pp. 1544-1552, 2010.

[20] M. Avdeev, J. R. Hester, V. K. Peterson, and A. J. Studer, "Wombat and Echidna: The Powder Diffractometers," Neutron News, vol. 20, pp. 29-33, 2009.

[21] D. Chateigner, Combined Analysis, 2010.

[22] J. Grasslin, L. B. McCusker, C. Baerlocher, F. Gozzo, B. Schmitt, and L. Lutterotti, "Advances in exploiting preferred orientation in the structure analysis of polycrystalline materials," Journal of Applied Crystallography, vol. 46, pp. 173-180, 2012.

[23] H.-R. Wenk, "Neutron diffraction texture analysis," Reviews in mineralogy and geochemistry, vol. 63, pp. 399-426, 2006.

[24] H. Yin and T. Emi, "Marangoni flow at the gas/melt interface of steel," Metallurgical and Materials Transactions B, vol. 34, pp. 483-493, 2003/10/01 2003.

[25] D. Phelan, M. Reid, N. Stanford, and R. Dippenaar, "In-situ observations of phase transformations in titanium," JOM Journal of the Minerals, Metals and Materials Society, vol. 58, pp. 67-69, 2006.

[26] S.-C. Moon, R. Dippenaar, and S.-H. Lee, "Solidification and the δ/γ phase transformation of steels in relation to casting defects," in IOP Conference Series: Materials Science and Engineering, pp. 012061, 2012.

[27] R. Smith and G. Sandland, "Some notes on the use of a diamond pyramid for hardness testing," J. Iron Steel Inst, vol. 111, pp. 285-294, 1925.

[28] I. Lonardelli, H.-R. Wenk, L. Lutterotti, and M. Goodwin, "Texture analysis from synchrotron diffraction images with the Rietveld method: dinosaur tendon and salmon scale," Journal of synchrotron radiation, vol. 12, pp. 354-360, 2005.

[29] H. Rietveld, "A profile refinement method for nuclear and magnetic structures," Journal of applied Crystallography, vol. 2, pp. 65-71, 1969.

[30] H. M. Rietveld, "The Rietveld Method," Physica Scripta, vol. 89, p. 098002, 2014.

[31] L. Lutterotti, S. Matthies, and H. Wenk, "MAUD (Material Analysis Using Diffraction): a user friendly Java program for Rietveld texture analysis and more," in Proceeding of the twelfth international conference on textures of materials (ICOTOM-12), 1999, p. 1599.

Chapter 4. *In-situ* studies of polysynthetically twinned Ti-Al crystals during heating and cooling

4.1 Introduction

In the as-received condition, the structure of the polysynthetic Ti-Al alloys studied in this part of the current research program consists of parallel lamellar platelets of ordered $L1_0$-γ and DO_{19}-α_2 phases, formed through the phase transformation sequence ($\alpha \rightarrow \alpha + \gamma \rightarrow \alpha_2 + \gamma$) or ($\alpha \rightarrow \alpha_2 \rightarrow \alpha_2 + \gamma$) during cooling, depending upon the overall alloy composition [1-3]. The mechanical properties are strongly anisotropic due to the lamellar orientation, but these properties are significantly improved when the lamellar orientation is parallel to the tensile load direction [4-6]. Using a directional solidification technique, polysynthetically twinned (PST) alloys with a single lamellar colony along the desired orientation have been successfully synthesized [7-9]. The PST crystals have attracted much attention on with respect to fabrication techniques and mechanical properties [7-10] since they provide excellent opportunities to develop an improved understanding of the pertaining deformation mechanisms because of their microstructural simplicity [1]. A deeper understanding of the microstructural changes and phase evolution within PST crystals that can occur during heat treatment, paves the way for guiding the design of PST ingots aimed at advanced alloy development [11, 12]. Kim *et al*. [11] and Lee *et al.* [12] argued that new α-grains nucleate within the platelets of the ordered γ-phase on heating a specimen to a temperature above the eutectoid temperature. These microstructural changes were observed by optical microscopy after heating and subsequent cooling and it was assumed that the α_2-grains formed by the nucleation of the α-phase within γ-laths on stacking faults or twins [13]. However, *ex-situ* microscopy can provide only partial answers; information and *in-situ* studies of the pertaining

microstructural development would greatly enhance our understanding of these nucleation and growth events.

To address the problem of phase transformation sequence, undercooling and correlated secondary processes, such as the formation of the microstructure, it is important to investigate the sequence of ordering in the disordered structures. According to the phase diagram, α always transforms to ordered γ-phase before the remnant α self-orders to α_2 at the eutectoid temperature. However, the transformation from disordered α-phase to ordered γ-phase needs to involve two processes simultaneously: the displacive change of topological close-packed stacking sequence from ABABABABA to ABCABCABC, and the diffusion controlled atomic ordering on the titanium and aluminium lattice sites. Undercooling of γ-phase nucleation has been frequently observed but rarely discussed [3, 11], it would seem upon cooling an α solid solution, the observation of γ-phase is delayed until ordering of α to α_2 sets in. In such a cooling scenario, the displacive character would not take place due to lack of order, however as soon as partial ordering on the basal lattice planes sets in, the displacive character is triggered and α_2 and γ appear simultaneously.

Neutron diffraction provides advantages of deep bulk penetration, quick measurement and the capability of detecting the ordered phases in Ti-Al alloys [14-16], and hence, this experimental technique is widely used to study order-disorder transitions, for example the ($\alpha_2 \rightarrow \alpha$) phase transition during heating [17, 18]. Moreover, it is also possible to study short-range-order structures by neutron diffuse-scattering analysis [19]. Because of the null-matrix effect [15, 19] neutron scattering is distinct from high-energy synchrotron X-ray diffraction [20] and particularly sensitive to the crystallographic order. Therefore, neutron diffraction is a very useful state-of-the-art technique for studying *in-situ* microstructural development and

phase changes in PST alloys, especially addressing the question of ordering and short-range ordering in the solid solution α-phase.

In addition to the information that can be obtained from *in-situ* neutron diffraction experiments, high-temperature laser-scanning confocal microscopy (HTLSCM) can record morphological evolution at high resolution in real time during an entire heat treatment [21-23]. By a combination of complementary *in-situ* neutron diffraction to obtain crystallographic information and *in-situ* HTLSCM observation to obtain morphological information, useful and reliable information can be obtained of the microstructural development and phase evolution in PST alloys during heat treatment.

In the present study, the orientation relationships between the respective phases and the atomic arrangement in the lamellar structure were determined by using EBSD techniques and neutron diffraction analysis at room temperature. Subsequently, phase changes and microstructural evolution during heating and cooling were revealed by *in-situ* neutron diffraction and *in-situ* HTLSCM experiments. Particular emphasis is given to determining short-range order in solid-solution α-phase at very high temperature. By taking into account these *in-situ* experimental findings, some new perspectives are provided about the way in which a single lamellar colony transforms into a fully lamellar structure.

In order to put into perspective the significance of the *in-situ* studies, it is pertinent to refer to selected findings of earlier researchers. Many researchers have studied the phase diagram of the Ti-Al system, but the relevant section of the diagram proposed by Shuster and Palm [24] and reproduced in Figure 4.1. It is used as a reference in the present discussion.

Although an eutectoid reaction is supposed to occur at 1393 K (1120˚C), Denquin and Naka [3] have provided convincing evidence supporting the premise: ‘the formation of the lamellar

structure does not occur through an eutectoid reaction but results from the precipitation of γ-lamellae in either a disordered α- or an ordered α_2-matrix'. Moreover, they have shown earlier that a fully lamellar structure can be formed in both the (α + γ) and (α_2 + γ) phase-fields [3]. This premise will be further considered in the analysis of the *in-situ* observations in a high-temperature microscope.

Denquin and Naka [3] argued: "the formation of the lamellar structure starts with a pre-nucleation stage on which stacking faults are introduced through the propagation of Shockley partials in either the hexagonal disordered α- or ordered α_2- matrix. The nucleation essentially involves an ordering reaction. The ordering process, which supposes the existence of a metastable lamellar *fcc* phase, consists of a nucleation of orientation variants at a number of separate sites in this metastable phase, followed by independent growth of the variants". These lamellar precipitates can grow longitudinally and/or laterally by the transfer of atoms onto ledge-kinks. They also found evidence that the longitudinal growth is faster than lateral growth. This finding will be re-visited by reference to the high-temperature observations in this study.

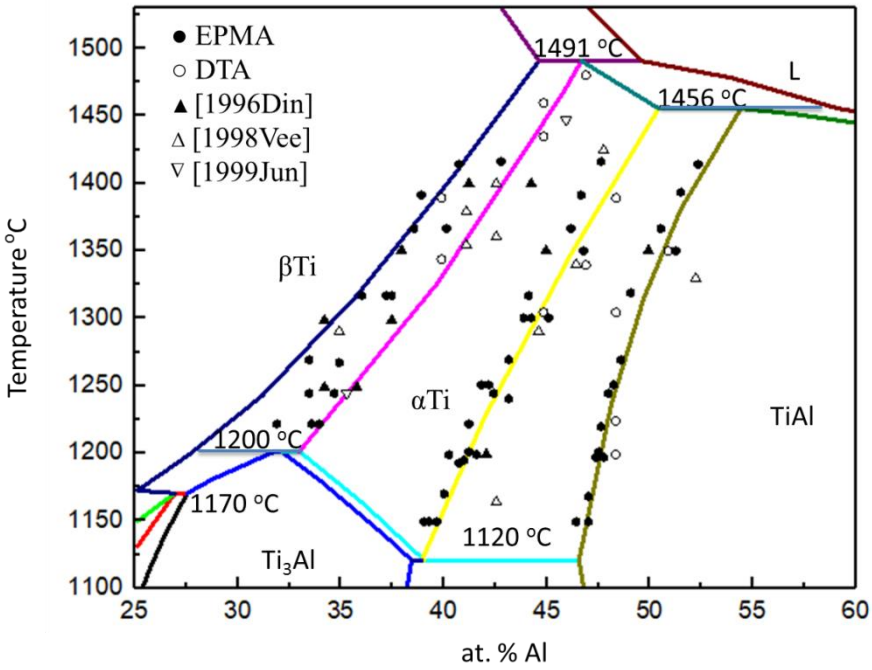

Figure 4.1 Section of the Ti-Al phase diagram, reproduced from reference [24].

4.2 Experiments

Button ingots of 35 g and nominal composition Ti-47.5Al (at. %) were produced by arc-melting in a water cooled copper crucible with titanium sponge and aluminium sheet. The buttons were melted six times to make sure that the composition distribution is uniform. The button ingots were then drop-cast into a steel mould. Master ingots had dimensions with diameter of 9 mm and length of 100 mm. Directional solidification [10], introduced in Chapter 3.1.1, was employed to induce grain growth in an optical float zone furnace at a growth rate of 5 mm/h without seeding material. Subsequently, 1 mm of the sample surface was removed from the top to avoid near-surface effects caused by the long heating cycle in the crystal growing process. Then, all the material except the main colony was ground off, such that only a single lamellar colony was obtained.

The microstructure of the alloy was characterized using a Zeiss® Ultra Plus™ scanning electronic microscope (SEM), coupled with an Oxford Instruments® Nordlys™ EBSD

system. As described in section 3.2.2, the EBSD data was collected using the Oxford Instruments® Aztec™ software and analysed using the Channel 5™ software. *In-situ* neutron diffraction was conducted in the WOMBAT diffractometer [25] at ANSTO. The incident beam wavelength λ, selected by a Ge-511 monochromator, was 1.54 Å or wavenumber 4.08 $Å^{-1}$. The sample was oriented with a zone axis γ-[111] || α-[002] pointing up, along the rotation axis ω, and mounted into the vacuum furnace of the Wombat instrument. 3D reciprocal-space maps were recorded by sample rotation around the ω-axis. A full map has been taken at room temperature. Subsequently, the system was heated to 1648 K, ostensibly just above the transition temperature (T_α ~1640 K), at a rate of 25 K/min. In order to completely transform to the α-phase, the sample was then held at 1648 K for 3.7 h before being cooled at a rate of 35 K/min. During the heat treatment, neutron diffraction patterns were captured at selected temperatures. *Canvas*™ software was used to draw the reciprocal space map and atomic arrangement. *Igor Pro4*™ software (WaveMatrix®, Lake Oswego, OR, USA) was then employed to compute the widths of the diffraction peaks.

In-situ microstructural observations were made on a polished sample 2 mm^2 x 1 mm in a high-temperature laser-scanning confocal microscope [22], introduced in section 3.2.6. The sample was heated from 373 K to 1703 K at a heating rate of 100 K/min, and then held for 10 min at 1703 K. It was subsequently cooled to 1280 K at a rate of 300 K/min and held for another 10 min at this temperature. The sample was cooled to room temperature at a rate of 100 K/min.

4.3 Results and discussions

4.3.1 Microstructure of the as-grown PST alloy

The microstructure and orientation texture of the as-grown PST alloys was measured in the as-received condition by EBSD as shown in Figure 4.2. The EBSD phase map confirms that

the PST alloys consist entirely of a lamellar structure with α_2-phase (blue region) and γ-phase (red region). Analysis of the area fraction indicates that the fraction of the γ-phase is about 77-78%. The pole figures (PF) of the α_2-phase in Figure 4.2(b) (top) shows that all the α_2-lamellae have the same crystal orientation. All the laths of the tetragonal γ-phase have a <111> zone axis, which is parallel to the <0001> zone axis of the hexagonal α_2-phase. The pole figures of the γ-phase in Figure 4.2(b) (bottom) show that the γ-laths have several variants, and that these variants orient with well-known Blackburn orientation relationship [29] to the α_2-laths, which can be described by: $\{111\}\gamma \parallel \{0001\}\ \alpha_2$, $<1\bar{1}0>\ \gamma \parallel <11\bar{2}0>\ \alpha_2$.

The common {0001} and {111} poles in the α_2- and γ-phases are indicated in the pole figure by surrounding blue and red hexagons, while the matching $<11\bar{2}0>\alpha_2$ and $<1\bar{1}0>\gamma$ directions are shown by blue and red squares, respectively. These observations are consistent with the experimental evidence and proposed mechanism of formation provided by Denquin and Naka [3].

When these γ-variants are separated on the basis of common {111} poles, they are classifiable into two groups, as shown in Figure 4.2(c,d) and Figure 4.2(e,f). The pole figures of these groups in Figure 4.2(d) and Figure 4.2(f) show that the lamellae in these groups are rotated crystallographically from each other by an angle of 60° about the common <111> pole, as is evident from the {111} pole figures. It therefore appears that these groups are analogous to Σ-3 twins in *fcc* crystals. The individual variants inside these groups are related to each other by a rotation of 90° about the $<100>\gamma$ axis, meaning that there are two groups of three variants each, to give a total of six orientation variants in the γ-phase, as illustrated by the six cubes in Figure 4.3 (same as Figure 2.7). It illustrates how these γ-variants formed

from the one single α-variant. The α-phase, with a hexagonal closed pack (*hcp*) based structure, transforms to a face centered cubic (*fcc*) based structure with two possible stacking sequences [5, 26, 27]. More details are described in section 2.1.2.2. Based on the stacking sequences, the new γ-phase crystals can be divided into two types (subsets 1 and 2 in Figure 4.3). The *fcc* phase then orders by aligning the *c*-axis in each type of γ-variant in three different directions, resulting in its $L1_0$ structure [2, 5, 26]. In total, this phase transformation leads to the formation of six variants in the γ-phase [26, 27], as also seen in the pole figures in Figures 4.3(d) and 4.3(f). These variants are grouped into two subsets, denoted in red and green colour by a rotational twinning. It is worth mentioning that the γ-phase was grouped in laths separately by subsets according to this ordering sequence. Each lath then consisted of three variants related by a rotation of 90° about <100>, or, equivalently, 120° about <111>, as noted above. The reason for this separation into two subsets is probably the fact that the three variants of the same subset have only minor differences in the length of their parallel axes, corresponding to the small difference between *c*-axis and the *a*-axis of the tetragonal γ-phase. It is therefore probable that these three similar variants, called domains, form relatively easily in juxtaposition with each other, with less interfacial energy required than the boundary of twins in the γ-phase. This kind of variant selection within any γ-lath may result in slip transmission being preferably confined to each lath, thereby affecting the ductility of the material.

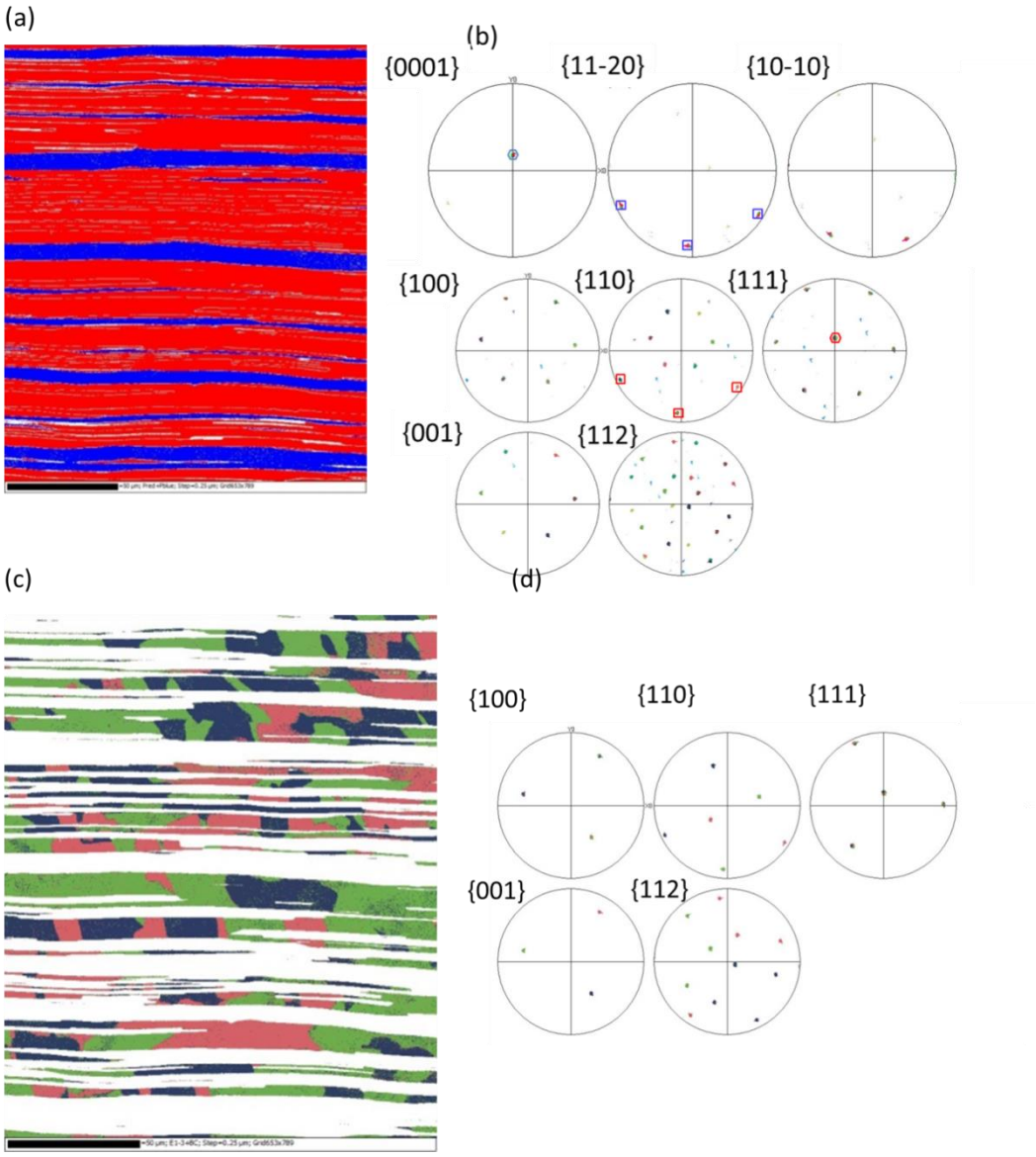
(a)
(b)
{0001}
{11-20}
{10-10}
{100}
{110}
{111}
{001}
{112}
(c)
(d)
{100}
{110}
{111}
{001}
{112}

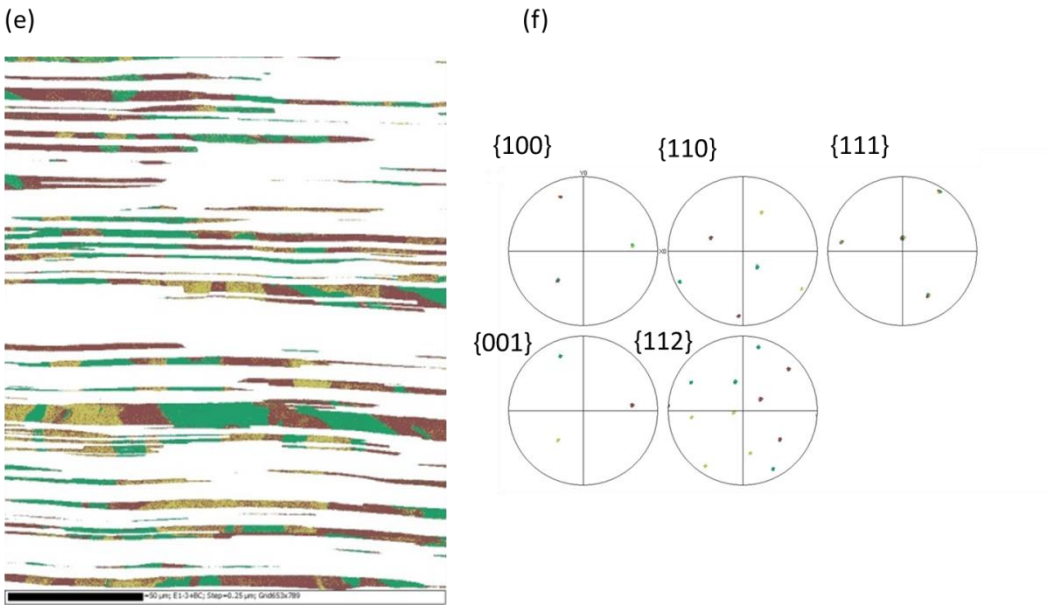

Figure 4.2: Texture studies of the prepared PST alloy at room temperature.
(a) Phase map – Red- γ TiAl, Blue- α_2 Ti_3Al;
(b) Pole figure of the α_2-phase (top) in the as-received sample showing one orientation for the whole area confirming that the crystal is a single colony, and γ-phase (bottom) showing orientation relationship with α_2 : $\{111\}\gamma \parallel \{0001\}\alpha_2$, $<1\bar{1}0>\gamma \parallel <11\bar{2}0>\alpha_2$;
(c) γ-Phase in TiAl – Subset 1;
(d) Corresponding PF showing one twin family with three variants rotated by 120° about <111> ;
(e) γ-Phase in TiAl – Subset 2, comprising laths with orientation rotated by 60° about <111> from Subset 1 (f).

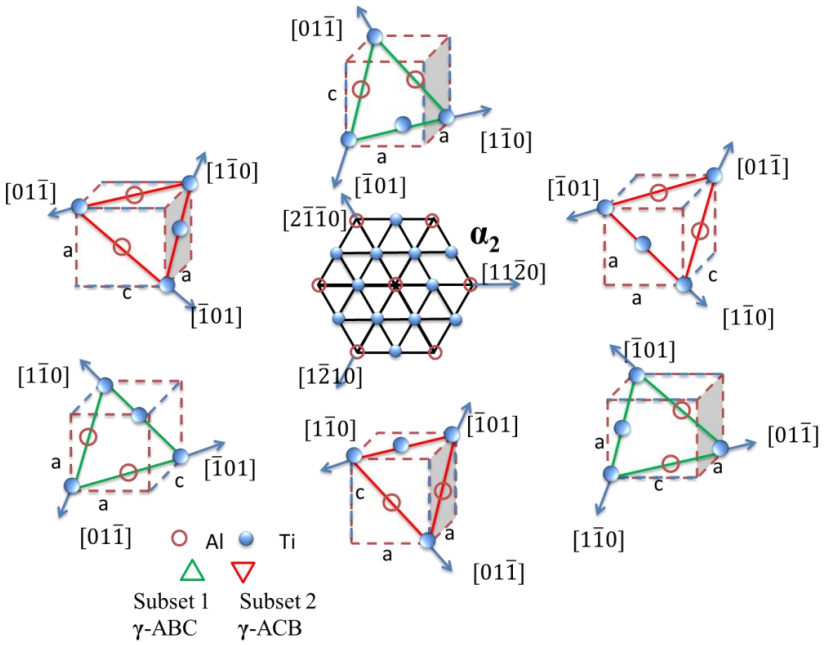

Figure 4.3. Schematics of the six γ orientation variants oriented differently with reference to the (0001) plane in the α_2-phase. The blue axis indicates the *c*-direction.

Detailed crystal structure information of the as-grown PST alloy was obtained by neutron diffraction experiments at 309 K, as presented in Figure 4.4. The zone axes of α_2- and γ-phases are respectively $[00\bar{1}]$ and $[1\bar{1}\bar{1}]$ (3-axes Miller indices [28]) according to the experimental set-up. The continuous rings in Figure 4.4 are reflections from the polycrystalline molybdenum wires, which were used to fix the sample. The sharp diffraction spots consist of three different reciprocal lattice patterns. By measuring the reciprocal spacing between each sharp spot, the first reciprocal lattice pattern is ascribed to the α_2-phase, which is indexed and drawn with black lines. There are two sets of reciprocal lattice patterns for the γ-phase, rotated with respect to each other by 60° about [111], which are represented by the orange and pink lines in Figure 4.4, respectively. These neutron diffraction analysis further confirms the presence of single lamellar ($\alpha_2 + \gamma$) colony structure of the as-grown PST alloy. Moreover, 60^o rotational twins along the [111] direction exist in the γ-phase, agreeing well with the EBSD results. The diffraction patterns from α_2- and γ- phases show overlapping diffraction spots, providing the existence of the Blackburn orientation relationship between the two phases: $<110>\gamma \parallel <110>\alpha_2$ and $[1\bar{1}\bar{1}]\gamma \parallel [00\bar{1}]\alpha_2$ (3-axes Miller indices [28]). Figure 4.4 shows streaks along the ring direction of the marked spots, which are attributed to a small angular mosaic spread about the zone axis in the orientation of the crystals. These observations indicate that the as-grown PST specimens were strained even before the imposition of heating cycles, such strain could have been introduced during grinding or alternatively, the strain could have been introduced during solidification.

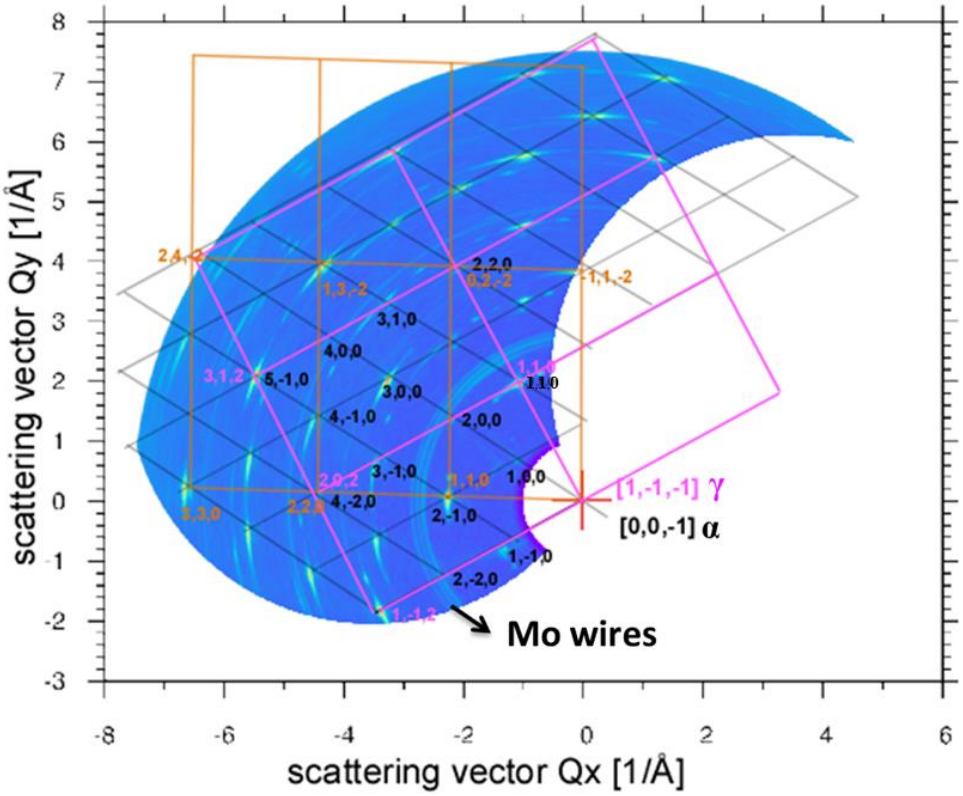

Figure 4.4 Neutron diffraction pattern of as-grown PST sample at 309 K, with zone axis parallel to $[00\bar{1}]$ α_2 // $[1\bar{1}\bar{1}]$ γ. The continuous diffraction rings are those of the Mo wires.

4.3.2 Microstructure evolution during heat treatment

In-situ neutron diffraction techniques were used to assess structural changes in the PST alloy during heating. The sample was heated to a temperature of 1648 K, where it was assumed that both the α_2- and γ- phases have transformed completely into the disordered α-phase. Following thermal stabilization, the neutron diffraction patterns were recorded and are displayed in Figure 4.5(a). The Ti-47.5Al PST crystals are near null-matrix composition [15, 21], with consequence that the peak intensity from the fully disordered phase is nearly zero due to the opposite neutron scattering lengths b_c of Ti ($b_{c,Ti}$ = -3.438 fm) and Al ($b_{c,Al}$ = 3.449 fm) atoms. In the disordered solid solution, the composition weighted average amounts to $b_{c,totl}$ = -0.17 fm, while the intensities scale with their square, leading to 10^{-3} times the intensities from a pure titanium or aluminium specimen - meaning the null-matrix reflections are practically invisible. $F_{hkl} = \sum_j a_j e^{i\vec{G}\cdot\vec{r}} = \sum_j a_j \exp[2\pi i(hx_j + ky_j + lz_j)]$ [19], in the ordered α_2- and

γ- phases basically lead to main reflections adding ($b_{c,Al}$ + $b_{c,Ti}$) = 0.01 fm and superstructure reflections subtracting ($b_{c,Al}$ - $b_{c,Ti}$) = 6.9 fm, their squares leading to non-observable main- and very strong superstructure reflections. The latter occurring only in the ordered structure makes neutron scattering very sensitive to the order parameter of Ti-Al alloys. Therefore, the Bragg peaks of the disordered α-phase are nearly invisible. Hence, only diffuse scattering of α-phase appears in Figure 4.5(a). The diffuse scattering intensity is distributed streakily around the reciprocal lattice points 030, 110 and $2\bar{1}0$. These reciprocal lattice points are related to the pattern of the α_2-phase, which suggests the existence of a short-range-order in the α-phase even at such a high temperature. In α_2-phase, superstructure reflections would be very strong as outlined before. Upon heating, they would weaken and finally disappear at the transformation eutectoid temperature T_{eu}. Above, critical fluctuations take place arranging on short length and time scales a tendency for local order, as it would appear below T_{eu}. In other words, having a known atom, say Al, in solid solution, it would feel the low-temperature binding potential and have a preference to a Ti neighbor atom, with some preference probability $P < 1$. The second nearest neighbor has a preference with P^2, the third P^3 and so on, which quickly dies off to zero for larger numbers, and the atomic probability is given by the concentration. A correlation length was estimated based on the full width at half-maximum of the radial diffuse peak, which gives an average value of 8.40 Å, equivalent to 2.9 atomic distances. In other words, after 2.9 atomic distances the probability to find the 'right ordered' kind of atoms drops to e^{-1}. Based on the above discussions, a model of the short-range-order structure on the [001]α-zone has been constructed and is shown in Figure 4.5(b). The blue and red positions represent titanium and aluminium atoms respectively. The blending into purple positions indicates that these lattice points can be randomly occupied by either titanium or aluminium atoms, according to the composition.

Note that such critical fluctuations occur not only as a function of spatial coordinate but also fluctuate in time. They are important pre-requisites for driving the α → γ transformation and

give answer to the raised question, whether a diffusive or displacive aspect of the transformation occurs first. Here we found evidence that first the order is established before a change in stacking takes place, explaining the often observed large undercooling of the onset of $\alpha \rightarrow \gamma$ transformation, which occurs only upon the onset of occurrence of α_2.

After the annealing the Ti-Al alloy at 1648 K for short-range order studies in the disordered α-phase, it has been cooled to 1553 K to record a neutron diffraction pattern with the re-formed γ-phase, displayed in Figure 4.6. The patterns of the re-appearing γ-phase form moreover an arc-shaped distribution of spots centered azimuthally around the locations of the previous single-crystal pattern. The distribution suggests a polycrystalline nature of the alloy at this temperature. The broken γ-spots are observed in the regions, as denoted by arrows in Figure 4.6, and their texture overlaps with the locations of the diffuse reflection of $2\bar{1}0$ and 110 of α phase in Figure 4.5. It indicates that these reflections are developed from the original α-grains by the Blackburn orientation relationship. Moreover, new γ-grains with different orientation were also formed.

For the breakdown we suggest the following scenario: The initial azimuthal streaks (Figure 4.4) describe a mosaic distribution of 6°, consisting of mosaic blocks separated by small-angle grain boundaries.

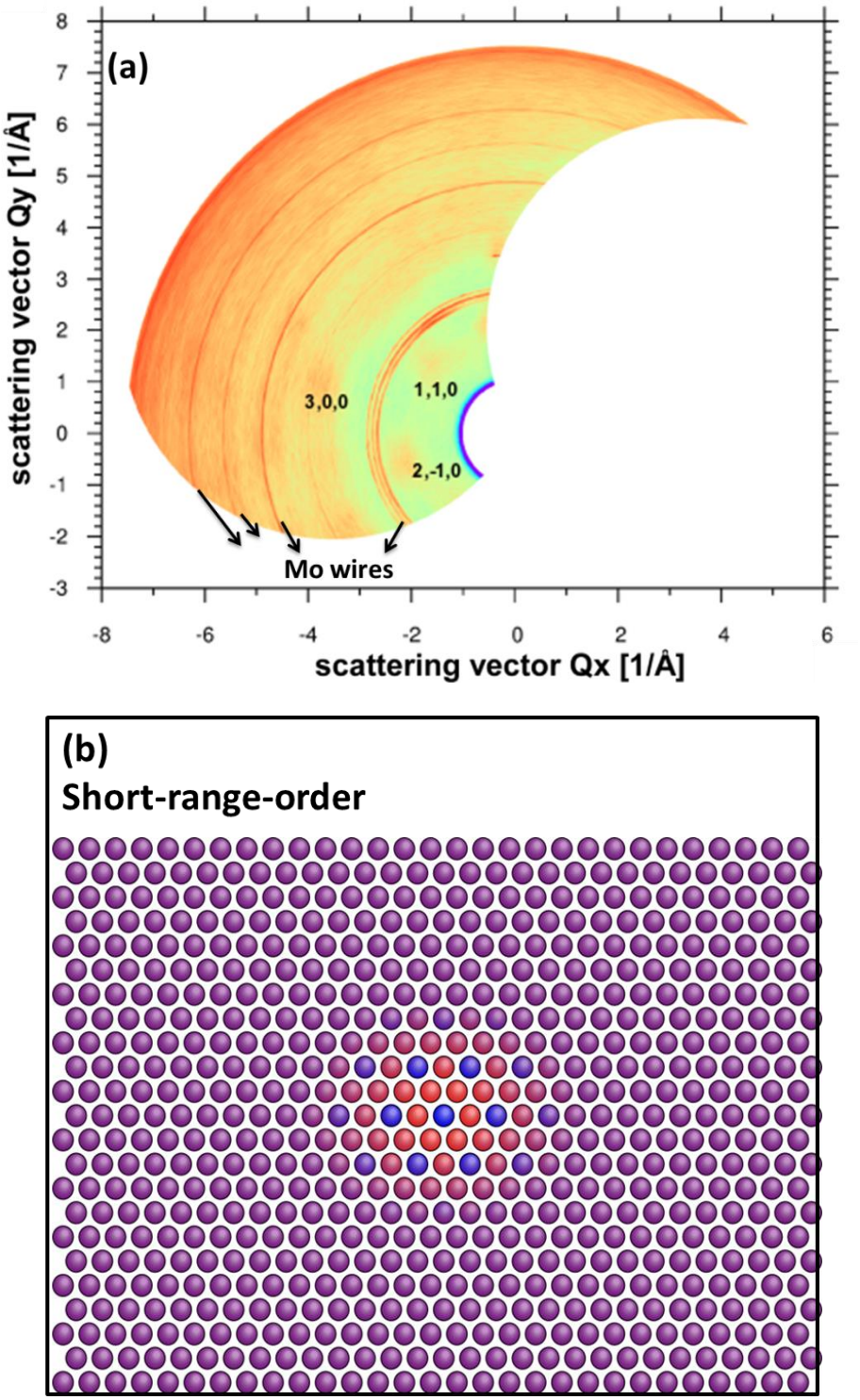

Figure 4.5:(a) Reciprocal map of PST crystals by neutron diffraction at 1648 K. (b) Schematic short-range-order structure on the (001) plane at 1648 K. The blue and red positions represent Ti and Al atoms respectively.The purple positons mean that they can be randomly occupied by Ti and Al atom.

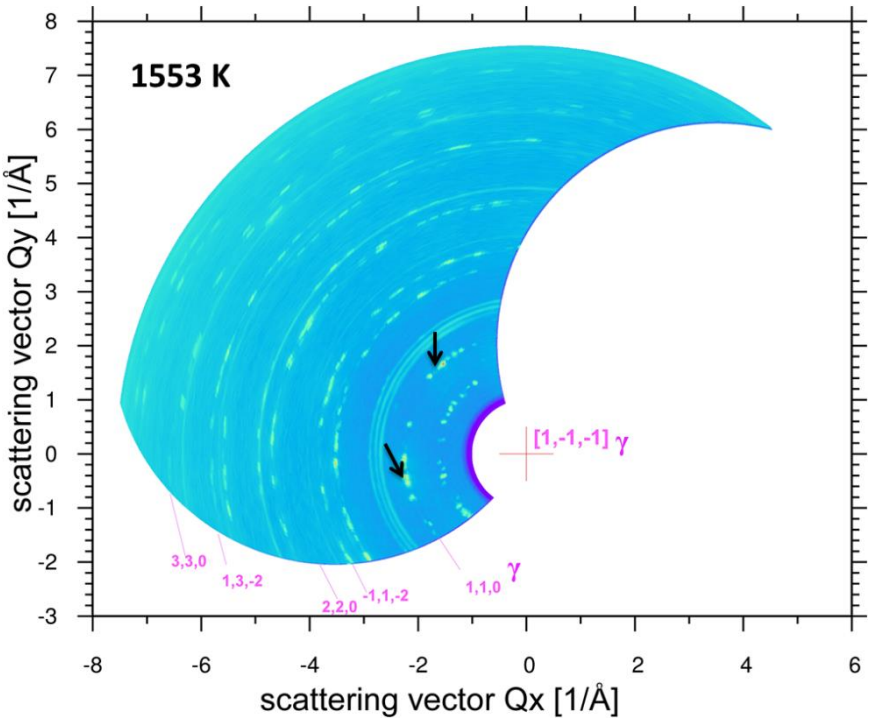

Figure 4.6 Neutron diffraction pattern after cooling from 1648K to 1553 K showing rings typical of polycrystalline samples .

The presence of new γ-variants provides support for the premise [3] that γ-lamellae can from in the (α_2 + γ) two phase-field. In order to further investigate this interesting observation, *in-situ* observations were made in a high-temperature laser-scanning confocal microscope.

Extracts from a video taken during the microstructural evolution during heating and cooling are shown in Figure 4.7. The micrographs in Figure 4.7 show microstructural evolution at 1703 K as a function of time (Figure 4.7(a-d)) and events occurring at 1553 K, following cooling from 1703K (Figure 4.7(e-f)). A single α-grain is visible upon heating to 1703 K (Figure 4.7(a)), meaning that the as-received lamellar structure has been full transformed to the disordered α-phase. After holding for 4 minutes, several new grains appear at the edge of the sample, as denoted by the red arrows in Figure 4.7(b). These new grains then grow as a function of time, as shown in Figure 4.7(c-d) (the new grain boundaries are marked by red arrows). The nucleation and growth at a temperature of 1703 K, of several α-grains from the

original lamellar structure are observed.

Following cooling from 1703K to 1553 K, γ-laths (green arrows) nucleated heterogeneously on α/α grain boundaries (Figure 4.7(e)), in accordance with earlier suggestions [30], These laths then grew into multiple lamellar colonies, the so-called fully lamellar structure (Figure 4.7(f)). These *in-situ* observations provide evidence in favour of the premise that the new γ-variants observed in the neutron diffractograms, originate from α-grains, the Bragg peaks of which are not visible in neutron scattering. It furthermore provides support of the suggestion [3] that γ-lamellae can from in the two phase (α + γ)-phase field, i.e. above the eutectoid transformation temperature.

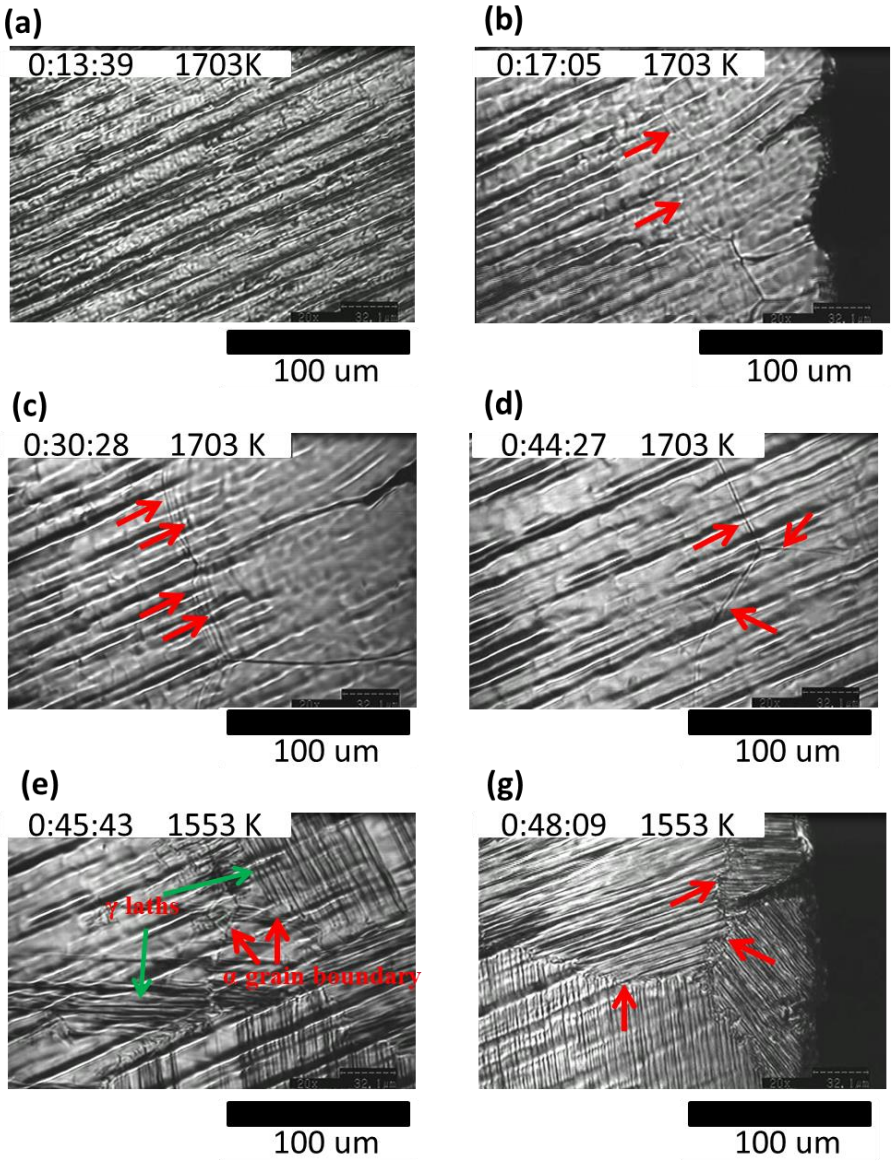

Figure 4.7 Laser scanning confocal micrographs from PST sample at selected temperatures (1703 K and 1553 K) with different time.

In order to provide further evidence in support of this premise, specimens were continuously cooled from 1703 K at a rate of 300 K/min, as shown in Figure 4.8.

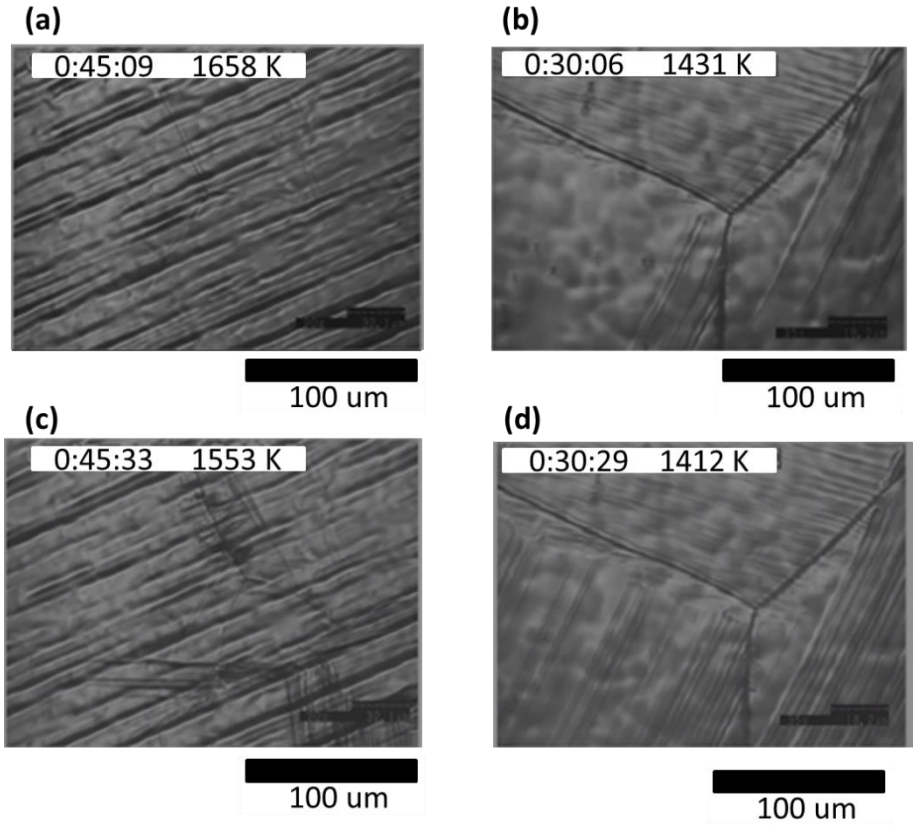

Figure 4.8 Selected extracts from videos of the Ti-47.5 %Al alloy continuously cooled from 1703 K at a rate of 300 K/min.
(a) Nucleation of new α-grains in the pre-existing lamellar matrix (please note that due to the mechanism of creating confocal images, the grooves of the pre-existing lamellar structure is preserved although the transformation to the α-phase has already occurred)
(b) Observations of a different sample cooled from 1703 K at a rate of 50 K/min. γ-lamellae have nucleated on α/α grain boundaries and grow into the α-matrix longitudinally and laterally. The rate of longitudinal growth is much higher than that of the lateral growth.
(c) The image in the right bottom section reveals that the laterally growing γ-lamellae grow longitudinally as individual platelets. Although it is not possible to provide crystallographic information, it appears that α-platelets form in-between these growing γ-lamellae.
(d) Pockets of γ-lamellae grow into the α-matrix of a different sample as (b) shows, cooled from 1703 K at a rate of 50 K/min.

In Figure 4.8(a), a new α-grain nucleates and grows into the lamellar structure that was heated from room temperature to 1703 K. Following cooling to 1553 K, γ-platelets nucleate on α/α grain boundaries and grow into the α-matrix as clearly shown in Figure 4.8(b). Our *in-situ* observations in a confocal microscope confirm the premise [3] that the formation of the lamellar structure does not occur through an eutectoid reaction, but originates from the precipitation of γ-lamellae in either an ordered α_2- or a disordered α-matrix. These

observations are also in agreement with the suggestion by Doherty [31] that the longitudinal growth of the lamellae is much faster that then lateral growth (thickening) of the lamellae. This more rapid growth in the longitudinal direction is clearly shown in Figure 4.8(b) and also in Figure 4.8(c), which was taken from a different specimen.

4.3.3 Microstructure after cooling

Figure 4.9 shows EBSD information of the microstructure and texture of the PST crystals following cooling from 1703 K to room temperature. It can be clearly seen in Figure 4.9(a) that equiaxed primary γ-phase forms on the boundaries of lamellar colonies. The Euler angle map confirms the presence of multiple ($\alpha_2 + \gamma$) lamellar colonies. The corresponding $\{0001\}\alpha_2$ pole figure in Figure 4.9(b) provides evidence of the existence of three different orientations of the α_2-phase since there are new α_2 colonies unrelated to the original orientations. The texture is more random than that of the as-grown PST crystals, providing further evidence that a fully lamellar structure has developed. The EBSD-map confirms the earlier optical microscopical evidence provided by Kim *et al.* [11] that lamellae of the new γ-phase nucleate at the α/α grain boundaries and grow into the α-matrix to form a fully lamellar structure alongside α_2-lamellae.

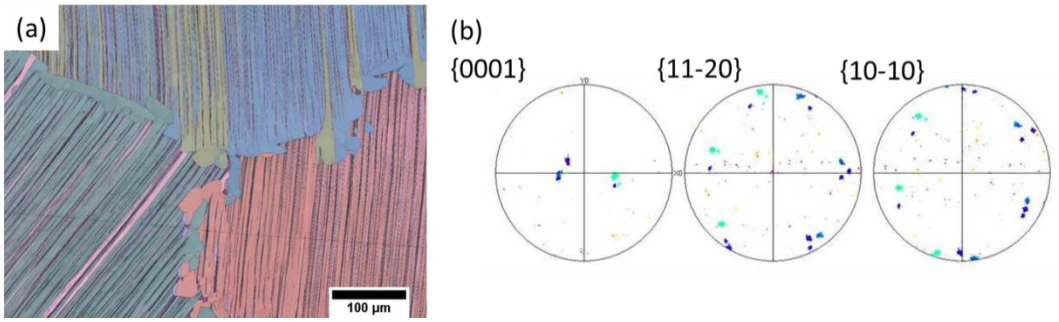

Figure 4.9: (a) EBSD Euler angle map of a triple point in the sample after cooling to room temperature (b) Pole figure of the α_2 -phase showing at least three different grains.

4.4 Conclusions

- Complimentary EBSD analysis and *in-situ* neutron diffraction and high-temperature

laser-scanning confocal microscopical studies provide new information of phase transformation sequences and microstructural evolution in polysynthetically twinned Ti-Al crystals.

- As-grown PST alloys consist of α_2- and γ-phase platelets within a single colony.
- During heating into the single α-phase field, the α_2- and γ-phases transform into a single disordered α-phase.
- At 1703 K, a single disordered α-phase recrystallized into the newly nucleated α-crystals due to the strain induced by grinding or solidification.
- During cooling, γ-phase lamellae nucleate on α/α grain boundaries and grow in pockets into the respective grains of the α-matrix.
- The disordered α-phase, trapped between these pockets undergoes a disorder/order transformation to form the ordered α_2-phase and in the result, the final structure consists of finely interspaced lamellae of the ordered γ- and ordered α_2-phases.

4.5 References

[1] F. Appel and R. Wagner, "Microstructure and deformation of two-phase γ-titanium aluminides," Materials Science and Engineering: R: Reports, vol. 22, pp. 187-268, 1998/05/01 1998.

[2] R. Ramanujan, "Phase transformations in γ based titanium aluminides," International Materials Reviews, vol. 45, pp. 217-240, 2000.

[3] A. Denquin and S. Naka, "Phase transformation mechanisms involved in two-phase TiAl-based alloys—I. Lambellar structure formation," Acta Materialia, vol. 44, pp. 343-352, 1996/01/01/ 1996.

[4] J. D. H. Paul, F. Appel, and R. Wagner, "The compression behaviour of niobium alloyed γ-titanium alumindies," Acta Materialia, vol. 46, pp. 1075-1085, 1998/02/13/ 1998.

[5] Y.-W. Kim, "Gamma titanium aluminides," JOM Journal of the Minerals, Metals and Materials Society, vol. 47, pp. 38-38, 1995.

[6] Y.-W. Kim, "Ordered intermetallic alloys, part III: gamma titanium aluminides," JOM Journal of the Minerals, Metals and Materials Society, vol. 46, pp. 30-39, 1994.

[7] H. Inui, K. Kishida, M. Misaki, M. Kobayashi, Y. Shirai, and M. Yamaguchi, "Temperature dependence of yield stress, tensile elongation and deformation structures in polysynthetically twinned crystals of Ti-Al," Philosophical magazine a, vol. 72, pp. 1609-1631, 1995.

[8] D. R. Johnson, H. Inui, S. Muto, Y. Omiya, and T. Yamanaka, "Microstructural development during directional solidification of α-seeded TiAl alloys," Acta Materialia, vol. 54, pp. 1077-1085, 2006.

[9] D. Johnson, Y. Masuda, T. Yamanaka, H. Inui, and M. Yamaguchi, "Creep deformation of TiAl-Si alloys with aligned γ/α2 lamellar microstructures," Metallurgical and Materials Transactions A, vol. 31, pp. 2463-2473, 2000.

[10] G. Chen, Y. Peng, G. Zheng, Z. Qi, M. Wang, H. Yu, et al., "Polysynthetic twinned TiAl single crystals for high-temperature applications," Nature Materials, 2016.

[11] S. Kim, H. Lee, M. Oh, and D. Wee, "Effects of the variation in α-phase volume fraction on the thermal stability of TiAl alloys with a lamellar microstructure," Journal of materials science, vol. 39, pp. 6929-6935, 2004.

[12] H. N. Lee, D. R. Johnson, H. Inui, M. H. Oh, D. M. Wee, and M. Yamaguchi, "Microstructural control through seeding and directional solidification of TiAl alloys containing Mo and C," Acta Materialia, vol. 48, pp. 3221-3233, 2000/07/17/ 2000.

[13] E. A. Ott and T. M. Pollock, "Microstructural development and creep deformation in equiaxed γ, γ+ α 2 and γ+ α 2+ B2 titanium aluminides," Metallurgical and Materials Transactions A, vol. 29, pp. 965-978, 1998.

[14] W. Reimers, A. R. Kaysser-Pyzalla, A. Schreyer, and H. Clemens, Neutrons and synchrotron radiation in engineering materials science: from fundamentals to material and component characterization: John Wiley & Sons, 2008.

[15] K.-D. Liss, "Metals challenged by neutron and synchrotron radiation" Metals, vol 7, pp. 266, 2017.

[16] T. Schmoelzer, K.-D. Liss, G. A. Zickler, I. J. Watson, L. M. Droessler, W. Wallgram, et al., "Phase fractions, transition and ordering temperatures in TiAl–Nb–Mo alloys: An in-and ex-situ study," Intermetallics, vol. 18, pp. 1544-1552, 2010.

[17] I. J. Watson, K.-D. Liss, H. Clemens, W. Wallgram, T. Schmoelzer, T. C. Hansen, et al., "In Situ Characterization of a Nb and Mo ContainingÎ³-TiAl Based Alloy Using Neutron Diffraction and High-Temperature Microscopy," Advanced Engineering Materials, vol. 11, pp. 932-937, 2009.

[18] S. Kabra, K. Yan, S. Mayer, T. Schmoelzer, M. Reid, R. Dippenaar, et al., "Phase transition and ordering behavior of ternary Ti–Al–Mo alloys using in-situ neutron diffraction," International Journal of Materials Research, vol. 102, pp. 697-702, 2011.

[19] J. Rodriguez, S. Moss, J. Robertson, J. Copley, D. Neumann, and J. Major, "Neutron scattering studies of short-range order, atomic displacements, and effective pair interactions in a null-matrix Ni 0.52 62 Pt 0.48 crystal," Physical Review B, vol. 74, pp. 104115, 2006.

[20] K.-D. Liss, A. Bartels, A. Schreyer, H. Clemens, "High-energy X-rays: a tool for advanced buld investigations in materials science and physics" Texture, Stress, and Microstructure. vol. 35, pp. 219-252, 2003

[21] D. Phelan and R. Dippenaar, "Widmanstätten ferrite plate formation in low-carbon steels," Metallurgical and Materials Transactions A, vol. 35, pp. 3701-3706, 2004.

[22] D. Phelan, M. Reid, N. Stanford, and R. Dippenaar, "In-situ observations of phase transformations in titanium," JOM Journal of the Minerals, Metals and Materials Society, vol. 58, pp. 67-69, 2006.

[23] K.-D. Liss, A. Stark, A. Bartels, H. Clemens, T. Buslaps, D. Phelan, et al., "Directional Atomic Rearrangements During Transformations Between thea-andc-Phases in Titanium Aluminides," Advanced Engineering Materials, vol. 10, 2008.

[24] J.C. Schuster, M. Palm, "Reassessment of the binary aluminum-titanium phase diagram," JPED, vol.27, pp. 255, 2006.

[25] A. J. Studer, M. E. Hagen, and T. J. Noakes, "Wombat: The high-intensity powder diffractometer at the OPAL reactor," Physica B: Condensed Matter, vol. 385, pp. 1013-1015, 2006.

[26] S. Zghal, S. Naka, and A. Couret, "A QUANTITATIVE TEM ANALYSIS OF THE LAMELLAR MICROSTRUCTURE IN TiAl BASED ALLOYS," Acta Materialia, vol. 45, pp. 3005-3015, 1997/07/01/ 1997.

[27] C. Teng, "Phase Field Simulation of the Nucleation and Growth of the Lamellar Microstructure in TiAl Alloys," Northeastern University, 2012.

[28] P. Partridge, "The crystallography and deformation modes of hexagonal close-packed metals," Metallurgical reviews, vol. 12, pp. 169-194, 1967.

[29] M. Blackburn, "SOME ASPECTS OF PHASE TRANSFORMATIONS IN TITANIUM ALLOYS," Boeing Scientific Research Labs., Seattle1970.

[30] S. R. Dey, A. Hazotte, and E. Bouzy, "Crystallography and phase transformation mechanisms in TiAl-based alloys – A synthesis," Intermetallics, vol. 17, pp. 1052-1064, 2009.

[31] R. D. Doherty, Physical Metallurgy, 3rd edn, Elsevier Science, Amsterdam, 1983.

Chapter 5. *In-situ* study of phase transitions in a selected Ti-Al alloys

5.1 Introduction

In the previous chapter, information was provided of *in-situ* studies in a binary Ti-Al alloy. In industrial practice, multi-component, γ-based Ti-Al alloys are used and for this reason *in-situ* observations have been extended to the analysis of a more complex alloy. The addition of niobium and carbon to Ti-Al alloys can enhance its mechanical performance since niobium decreases the stacking fault energy, stabilizes the beta phase at high temperature and modifys the structure of oxidation layer [1, 2]. Carbon can induce precipitation hardening in Ti-Al alloys, which further improves their strength [3]. The Ti-45Al-7.5Nb-0.5C alloy has been targeted as a candidate for application in the aerospace industry and for this reason it has been selected for the high-temperature microscopical study.

For an appropriate heat treatment design, it is important to have knowledge of the pertaining phase relationships and consequently, microstructural development of this alloy. Unfortunately there are serious discrepancies between the experimental data provided by earlier researchers and thermodynamic calculations [4-6]. Chladil *et al.* [5] employed Differential Scanning Calorimetry and Liss *et al.* [4] and Yeoh *et al.* [6] used *in-situ* high energy X-ray techniques to estimate the temperature at which the alloy transforms to a fully disordered α-phase (the so-called alpha transus temperature, usually abbreviated as T_α). Chladil *et al.* [5] determined T_α of the alloy under investigations under near-equilibrium conditions, as 1566 K. It should be noted that carbon has an insignificant influence on the T_α. They are 1565 K and 1566 K respectively remains essentially constant, for the alloys

containing 0.25 at. % C and 0.5 at. % C respectively. On the contrary, Liss *et al.* [4] found that a fully α-structure existed at 1344 K. On slow cooling, γ-reflections re-appeared, which were coherently aligned with two twinned and all three domain orientations to the α-grain, thereby showing the fully developed lamellar structure.

However, it is not only knowledge of the transus temperature that is important, but also the detail of the subsequent microstructural development as a function of cooling rate. In a recent development Phelan *et al.* [7] and Moon *et al.* [8] incorporated a differential thermal analytical facility into a high temperature laser-scanning confocal microscope, which was used in the present study. By this technique it is possible to observe *in situ*, on the surface of a specimen, microstructural changes that occur at temperature and in real time, while at the same time recording thermodynamic data pertaining to phase transitions occurring in the bulk.

5.2 Experiments

The Ti-45Al-7.5Nb-0.5C powder was manufactured by a plasma-melting induction-guiding atomization method, the introduction of which is shown in section 3.1.2. Then it was consolidated by hot isostatic pressing (HIP) for 2 h at 200 MPa at 1553 K to produce the Ti-45Al-7.5Nb-0.5C alloy [9]. After the HIP processing, the alloy forms a duplex microstructure consisting of lamellar α_2/γ- and globular γ- grains with average grain size of 15 μm [5, 10]. Then, the samples were Electrical Discharge Machining (EDM) wire-cutted into the round disk with 4 mm diameter, 2 mm thick and polished by Struers Tegrapal-21 for HTLSCM studies.

Specimens were heated to a temperature of 1703 K at a heating rate of 100 K/min. and held for 5 min. at this temperature. Then they were then cooled at rates of 25 K/min, 50 K/min,

100 K/min, 200 K/min and 400 K/min respectively to room temperature. In another series of experiments, samples were reheated from room temperature to 1703 K, held for 5 min. and then cooled at a rate of 200 K/min to room temperature and this heating/cooling cycle was repeated four times. Microstructures were characterized by a Leica Eclipse LV100DA-U microscope, different parts of the specimen surface were captured and ImageJ [11] software was employed to stitch together the pictures of the entire HTLSCM sample.

5.3 Results and Discussions

5.3.1 Cooling rates

Figure 5.1 shows the microstructure evolution at a cooling rate of 100 K/min. following annealing at 1703 K for 5 minutes. Figure 5.1(a) shows how ordered γ-laths nucleate on α/α grain boundaries and grow alongside α_2-laths into the α -matrix as shown in Figure 5.1(b). On further cooling newly formed γ-laths developed into a fully lamellar structure as shown in Figure 5.1(c). No further microstructural changes occur upon further cooling as shown in Figure 5.1(d). The morphology of the microstructural changes in the Ti-Al-Nb alloy are essentially the same as those observed in the PST crystals (Chapter 4).

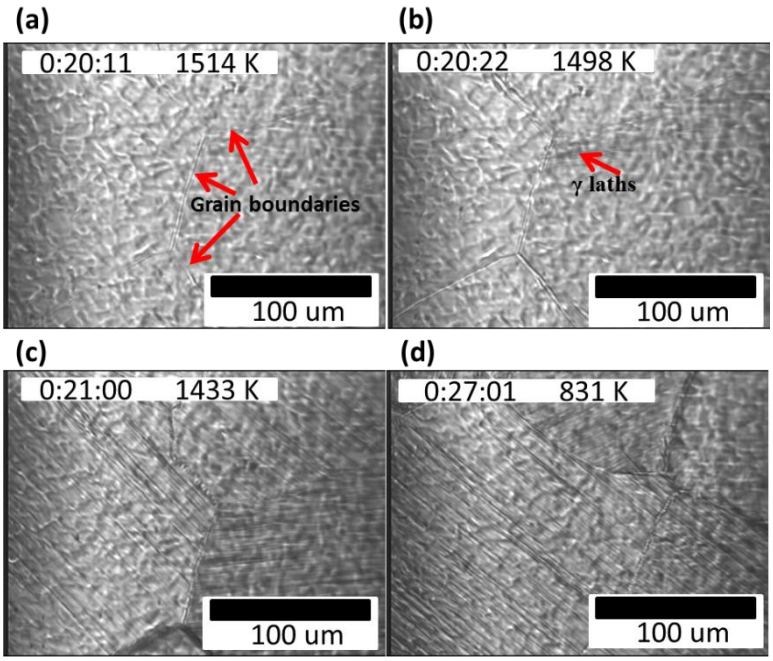

Figure 5.1 The microstructural evolution of a Ti-45Al-7.5Nb-0.5C alloy upon cooling at a rate of 100 K/min following annealing at 1703 K.

The temperature, at which these nucleation events occur, depends on the cooling rate and Figure 5.2 shows the observed nucleation events that we observed firstly at five different cooling rates.

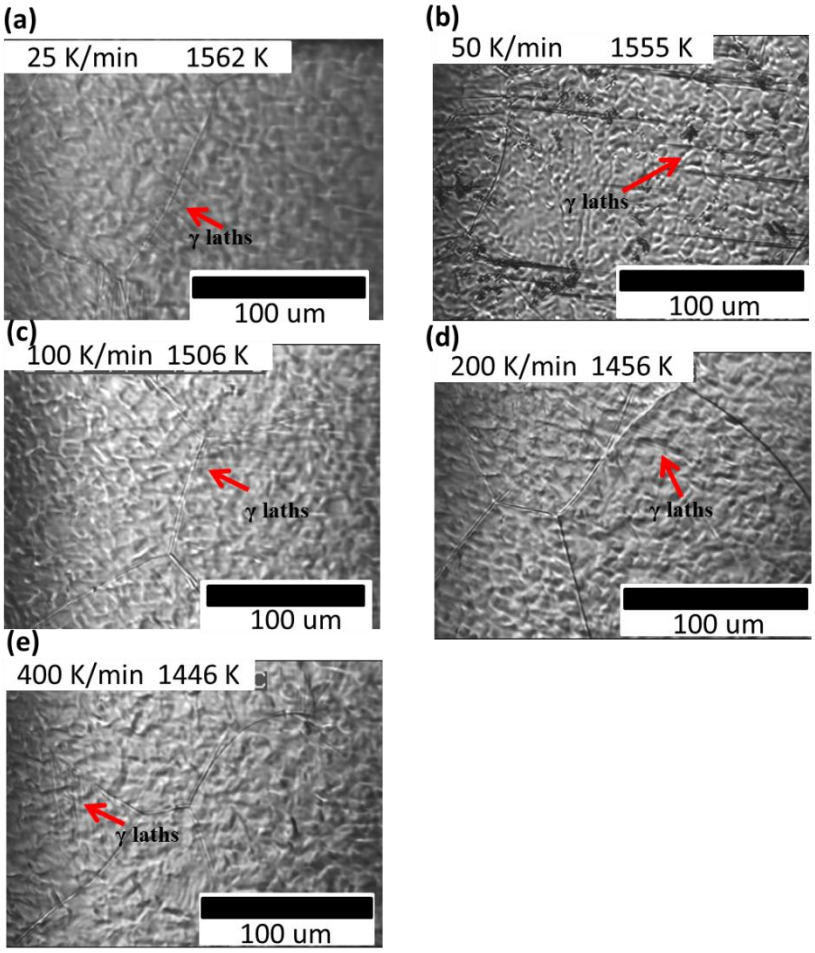

Figure 5.2 Nucleation of γ-laths at five different cooling rates (a) 25 K/min, (b) 50 K/min, (c) 100 K/min, (d) 200 K/min, (e) 400 K/min on the HTLSCM.

Only a small area can be observed in the high-temperature microscope at a given time, but bulk information can be obtained by using the incorporated DTA. Figure 5.3 shows the first derivature of *in-situ* DTA curves of the Ti-45Al-7.5Nb-0.5C alloy, cooled at different cooling rates. It is evident that the transformation temperature of α to γ decreases with an increase in cooling rate, changing from 1512 K to 1384 K with a cooling rate increase from 25 K/min to 400 K/min.

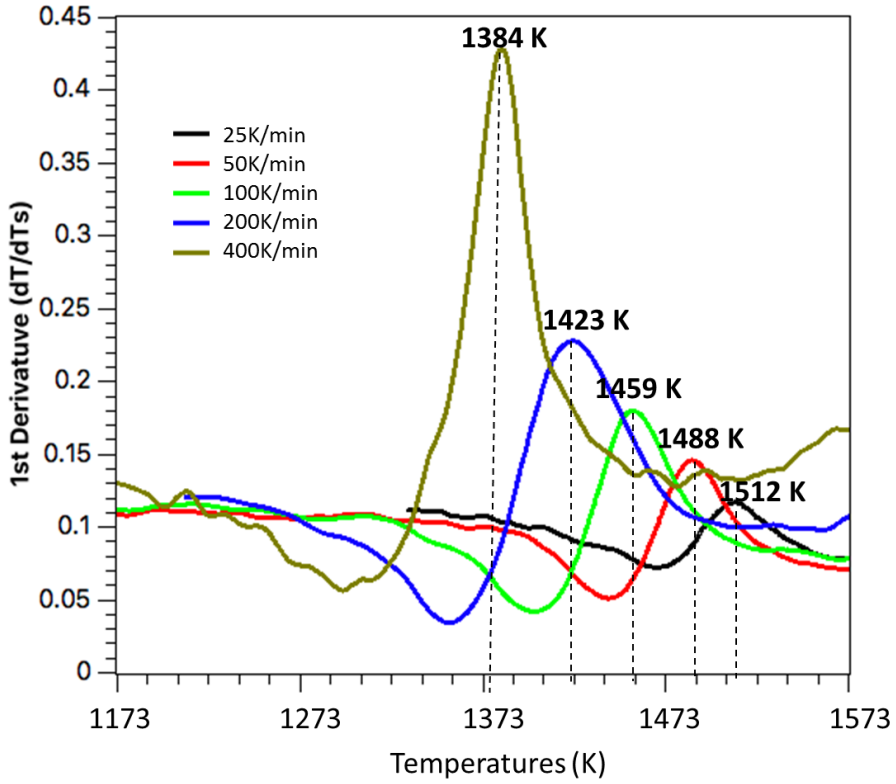

Figure 5.3 The first derivature of DTA curves with different cooling rate, where black curve stands for 25 K/min, red 50 K/min green 100 K/min blue 200 K/min brown 400 K/min.

Specimens of the Ti-45Al-7.5Nb-0.5C alloy were annealed at 1703 K and cooled to room temperature at rates of 25 K/min, 50 K/min, 100 K/min and 400 K/min, respectively. The average grain sizes, shown in Figure 5.4, were 174, 171, 146 and 129 μm at the corresponding cooling rates, whereas in the as-received condition the grain size was only 15 μm. It is therefore clear that annealing at 1703 K leads to the formation of large α-grains. It also transpires that the rate of cooling from the annealing temperature has an influence on the resulting grain size at room temperature.

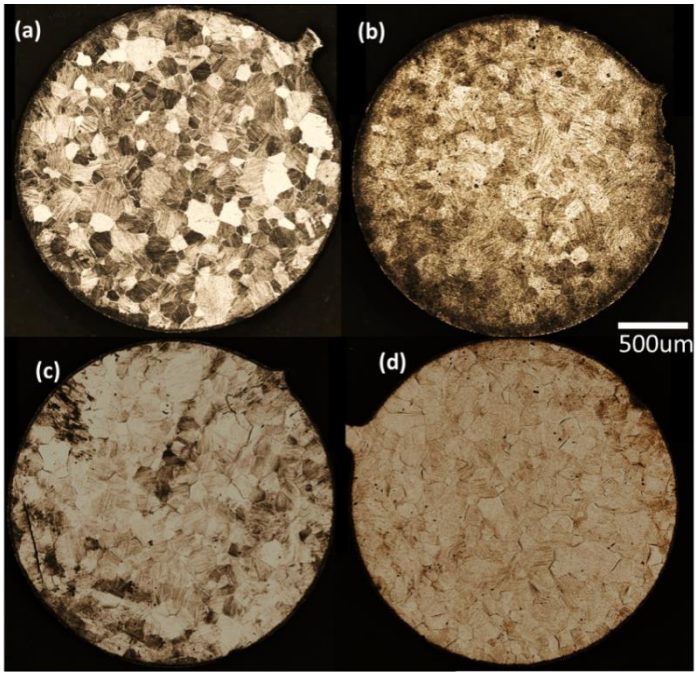

Figure 5.4 The microstructure of the Ti-45Al-7.5Nb-0.5C alloy following different cooling rates: (a) 25 K/min, (b) 50 K/min, (c) 100 K/min and (d) 400 K/min.

5.3.2 Grain size

In addition to the cooling rate, grain size needs to be considered as a factor that might affect the measured α-transus temperature.Since the γ-phase nucleates on α/α grain boundaries, it was important to determine whether or not the grain boundary area available for nucleation would have an effect on the measured α-transus temperature.

Samples of the Ti-45Al-7.5Nb-0.5C were heated to 1703 K and then cooled to room temperature at a rate of 200 K/min and the cycle was repeated four times. Figure 5.5 shows the microstructures following the 2^{nd} to the 4^{th} cycle. It therefore seems that repeated heating and cooling cycles increase the grain size, which is maybe caused by the participation of secondary γ-phase.

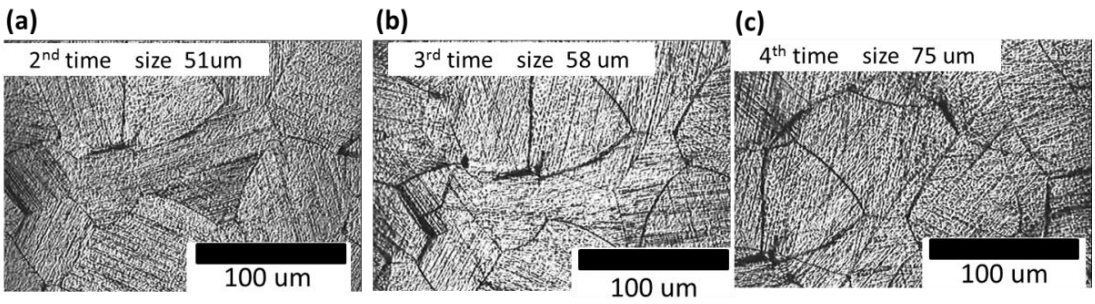

Figure 5.5 Microstructures following repeated heating and cooling cycles.

The *in-situ* DTA curves obtained in the same experiments are shown in Figure 5.6 and it seems that there is little change in the measured α-transus temperature, confirming that nucleation is not limited by the grain boundary area available for nucleation.

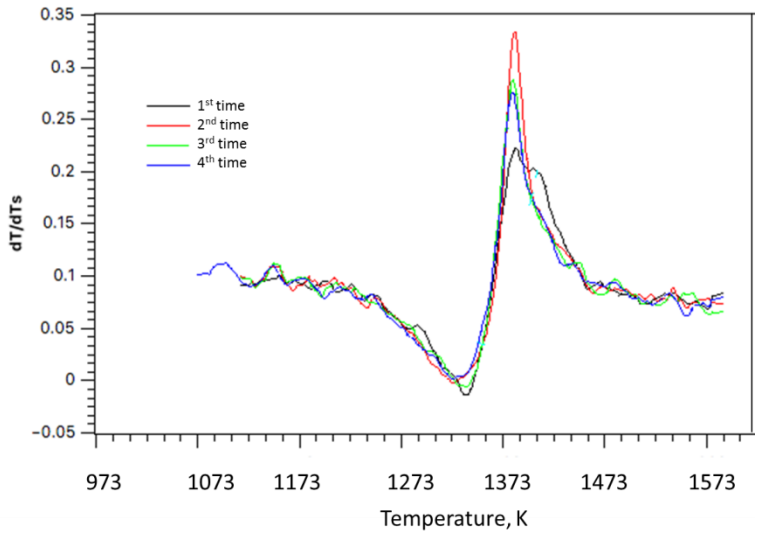

Figure 5.6 The first derivative of DTA curves with different original grain size at the cooling rate of 200 K/min.

5.3.3 α-transus temperature

The experimental information discussed above, shows that the measured α-transus temperature is a strong function of the cooling rate and that the size of the α-grains does not play a major role. The transformation temperature as a function of cooling rate is shown in Figure 5.7 and it follows that the measured transus temperature is almost a nearly function of undercooling as expected from the fundamental theories of phase transformations.

Extrapolation of the experimental measurements indicates that the equilibrium α-transus temperature is higher than 1520 K, since the y-axis is approached asymptotically. This observation is in reasonable agreement with the equilibrium measurement of Chladil *et al*., 1566 K determined by Chladil *et al.* [5]. (In comparing these transus temperatures, it has to be borne in mind that the temperatures shown in the high-temperature microscope videos are the control temperatures and not the actual specimen temperature).

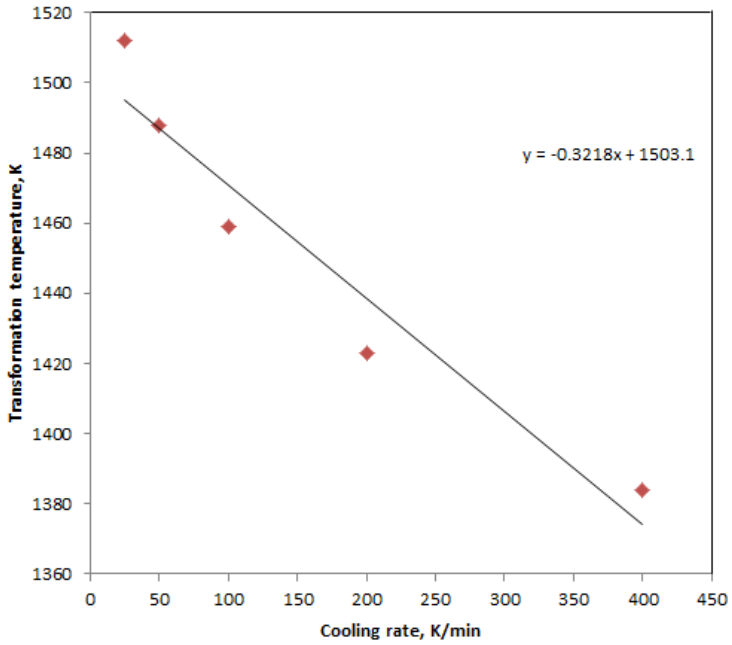

Figure 5.7 The transformation temperature as a function of cooling rate, where the red square represents the measured α-transus temperature determined by DTA.

5.4 Conclusions

- With cooling rate increases, the measured α-transus temperature of a Ti-45Al-7.5Nb-0.5C alloy decreases almost linearly with an increase in cooling rate (undercooling) as expected.
- The size of α-grains does not affect the measured α-transus temperature.
- The estimated equilibrium α-transus temperature is in reasonable agreement with earlier measurements on the exact same alloy.

5.5 References

[1] V. Haanappel, H. Clemens, and M. Stroosnijder, "The high temperature oxidation behaviour of high and low alloyed TiAl-based intermetallics," Intermetallics, vol. 10, pp. 293-305, 2002.

[2] I. J. Watson, K. D. Liss, H. Clemens, W. Wallgram, T. Schmoelzer, T. C. Hansen, et al., "In Situ Characterization of a Nb and Mo Containing γ - TiAl Based Alloy Using Neutron Diffraction and High - Temperature Microscopy," Advanced engineering materials, vol. 11, pp. 932-937, 2009.

[3] F. Appel, J. D. H. Paul, and M. Oehring, Gamma titanium aluminide alloys: science and technology: John Wiley & Sons, 2011.

[4] K.-D. Liss, A. Bartels, H. Clemens, S. Bystrzanowski, A. Stark, T. Buslaps, et al., "Recrystallization and phase transitions in a γ-TiAl-based alloy as observed by ex situ and in situ high-energy X-ray diffraction," Acta Materialia, vol. 54, pp. 3721-3735, 2006.

[5] H. F. Chladil, H. Clemens, G. A. Zickler, M. Takeyama, E. Kozeschnik, A. Bartels, et al., "Experimental studies and thermodynamic simulation of phase transformations in high Nb containing γ-TiAl based alloys," International Journal of Materials Research, vol. 98, pp. 1131-1137, 2007.

[6] L. A. Yeoh, K.-D. Liss, A. Bartels, H. Chladil, M. Avdeev, H. Clemens, et al., "In situ high-energy X-ray diffraction study and quantitative phase analysis in the α+ γ phase field of titanium aluminides," Scripta Materialia, vol. 57, pp. 1145-1148, 2007.

[7] D Phelan, N Stanford, R Dippenaar, "In situ observations of Widmanstätten ferrite formation in a low-carbon steel," Materials Science and Engineering: A, vol. 407 (1-2), pp. 127-134, 2005.

[8] S.-C. Moon, R. Dippenaar, and S.-H. Lee, "Solidification and the δ/γ phase transformation of steels in relation to casting defects," in IOP Conference Series: Materials Science and Engineering, pp. 012061, 2012.

[9] R. Gerling, H. Clemens, and F. P. Schimansky, "Powder Metallurgical Processing of Intermetallic Gamma Titanium Aluminides," Advanced Engineering Materials, vol. 6, pp. 23-38, 2004.

[10] H. Chladil, H. Clemens, H. Leitner, A. Bartels, R. Gerling, F.-P. Schimansky, et al., "Phase transformations in high niobium and carbon containing γ-TiAl based alloys," Intermetallics, vol. 14, pp. 1194-1198, 2006.

[11] C. A. Schneider, W. S. Rasband, and K. W. Eliceiri, "NIH Image to ImageJ: 25 years of image analysis," Nature Methods, vol. 9, p. 671, 06/28/online 2012.

Chapter 6. Lattice parameter evolution during heating of Ti-45Al-7.5Nb-0.25/0.5C alloys under atmospheric and high pressures

6.1 Introduction

Based on the study microstructural evolution of polycrystalline Ti-Al alloys with the change of temperature ("Chapter 5. *In-situ* study of phase transitions in a selected Ti-Al alloys"), a further complicated research on lattice parameter evolution of these alloys under variant pressure and temperature, was launched. It is because that a new route for the processing of titanium aluminide components under high pressure has been proposed [1]. Since these forming processes operate at elevated temperature and pressure, it is imperative that the microstructural integrity of the work-pieces be maintained, especially by limiting grain growth during high-temperature processing and minimizing the development of internal stresses during forging operations. More importantly, at very high pressure (9.8 GPa), the science of phase transition in Ti-Al alloys is critical [2, 3] and explored carefully in this study.

Processing in the ($\alpha_2/\alpha + \gamma$) phase-field remains a challenge due to crystalline anisotropy and the presence of covalent bond. Appel *et al*. [4] pointed out the "crystal partitioning" effect [5, 6] can therefore lead to significant grain refinement of castings and significantly reduced texture (More details are described in section 2.1.1). The β-phase is highly isotropic and independent slip systems can operate during dynamic recovery as experimentally confirmed by Liss *et al.* [7] in an *in-situ* synchrotron X-ray study. The β-solidifying alloys being studied in the present program have a fine and homogenous microstructure and are therefore easier to forge than conventional ($\alpha_2/\alpha + \gamma$) alloys [4, 8, 9]. It is possible to stabilize the β-phase by the

addition of selected alloying elements, but it has recently been established that the β-phase can also be physically induced by the application of high hydrostatic pressure at high temperature. However, the question as to how this newly formed β-phase would affect the lattice strains in the α_2/α- and γ-phases has not been answered [10]. It is important to answer this question because the lattice strains have a determining influence on the mechanical properties of the product. Moreover, the evaluation of lattice parameters is a very sensitive measurement to determine phase transformations of various kinds [11-13] and can reveal segregation pathways in phase diagrams [14]. Therefore, in considering lattice parameter evolution as a central theme in this study, data from two earlier *in-situ* heating experiments, were re-visited in order to compare (i) a high-energy synchrotron radiation study on Ti-45Al-7.5Nb-0.5C under atmospheric pressure [15] with (ii) an energy-dispersive synchrotron X-ray diffraction experiment on Ti-45Al-7.5Nb-0.25C under high pressure at 9.6 GPa [10].

Figure 6.1(a) shows a section through the Ti-Al binary phase diagram [16], while a section through a Ti-Al-7.5 at. % Nb alloy, proposed by Chladil *et al*. [17] is shown in Figure 6.1(b). The alloy used in the present study is schematically shown by the vertical line at 45 at. % Al. It is important to note that this section through the phase diagram applies to atmospheric pressure and to our knowledge, the extent to which pressure changes the pertaining phase equilibria has not been determined as yet.

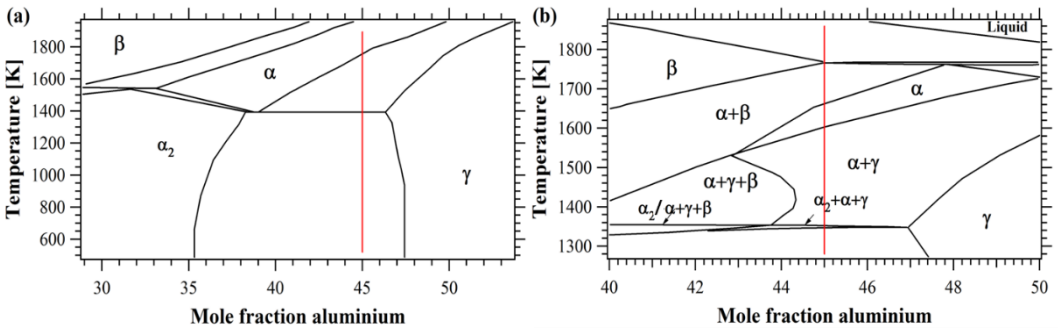

Figure 6.1 (a) Binary phase diagram of Ti-Al [16]; (b) Section through a proposed phase diagram of the Ti-Al-Nb alloy system for an alloy containing 7.5 at. % Nb [17].

Since a Ti-Al-Nb-C alloy is studied under conditions of severe-plastic deformation and high temperature, it is important to identify the most critical parameters that determine microstructural evolution and stability. One important variable is lattice parameter evolution, since for example, a change in the *c*/*a* ratio of the α-lattice has a determining influence on the pertaining slip and twinning deformation mechanisms. Moreover, changes in the lattice parameter impact on orientation relationships and have an influence on interphase stress development. In addition, the mechanism and morphology of phase transformations need to be taken into account since they play an important role in achieving microstructural stability.

Although the lattice parameter evolution plays a pivotal role in assessing the high-temperature behavior of titanium-aluminides, as argued above, only little information has been traced to date, with the notable exception of the earlier *in-situ* experiments by Shull *et al.* [18], then by Yeoh *et al.* [15] and more recently that of Liss *et al.* [10].

The very early work of Shull *et al.* in 1990 reports on the first *in-situ* investigation of titanium aluminides at high temperature, focusing on the experimental determination of phase fields, while lattice parameter evolution is traced. In 2007, Yeoh *et al.* [15] reported the changes occurring in the *c*/*a* ratio of the lattice parameters in a Ti-45Al-7.5Nb-0.5C alloy during heating at atmospheric pressure. She suggested that as far as X-ray analyses are concerned, a simplification should be made by assuming that the α_2- (ordered) and the α-phase (disordered) be regarded as a single phase since X-rays cannot clearly distinguish between an ordered and disordered structure.

Liss *et al*. [10] recently conducted an *in-situ* X-ray diffraction experiment on a Ti-45Al-

7.5Nb-0.25C alloy under high hydrostatic pressure. They studied the phase evolution of a Ti-45Al-7.5Nb-0.25C alloy as a function of time under high pressure and high temperature within a synchrotron X-ray source (SPring-8 beamline BL04B1, run number M1472). The *in-situ* diffactograms are displayed in Figure 6.2 which have been analyzed by the Rietveld method using MAUD (*Material Analysis Using Diffraction software* [19, 20]) for the evolution of phase fractions as a function of temperature, shown in Figure 6.3. Also shown are the phase fractions determined by Yeoh *et al.* [15] in a roughly similar alloy Ti-45Al-7.5Nb-0.5C, but under standard atmospheric conditions. The two alloys have been manufactured under identical conditions and the two *in-situ* experiments were conducted under normal atmospheric and high pressure respectively. However, it is important to note that carbon can have a significant influence on phase evolution in these alloys and for this reason care need to be taken in comparing the alloys containing 0.25 at. % C and 0.5 at. % C respectively. For example, the eutectoid temperature, T_{eu} , is increased by 20 K from 1453 K to 1473 K, but the respective γ-solvus, $T_{\gamma,solv}$, 1565 K and 1566 K respectively [21] remains essentially constant under atmospheric pressure. Notwithstanding these differences, the two alloys can be compared with respect to their respective pressure-induced behaviors. The *fcc*-based, ordered γ-phase of $L1_0$ structure, co-exists with an *hcp*-based, ordered α_2-phase of $D0_{19}$ structure at room temperature. Upon heating, the α_2-phase undergoes an inverse eutectoid order-disorder transition to form a fully disordered hexagonal α-phase at T_{eu}. The fraction of the γ-phase decreases upon heating and finally transforms fully into the disordered α-phase at $T_{\gamma,solv}$. Salient features when the Ti-45Al-7.5Nb-0.25C alloy is heated under a pressure of 9.6 GPa, are the appearance of the *bcc* β-phase in an ($\alpha/\alpha_2 + \beta + \gamma$) field and the dissolution of γ phase at $T_{\gamma,solv}$ to form ($\alpha + \beta$).

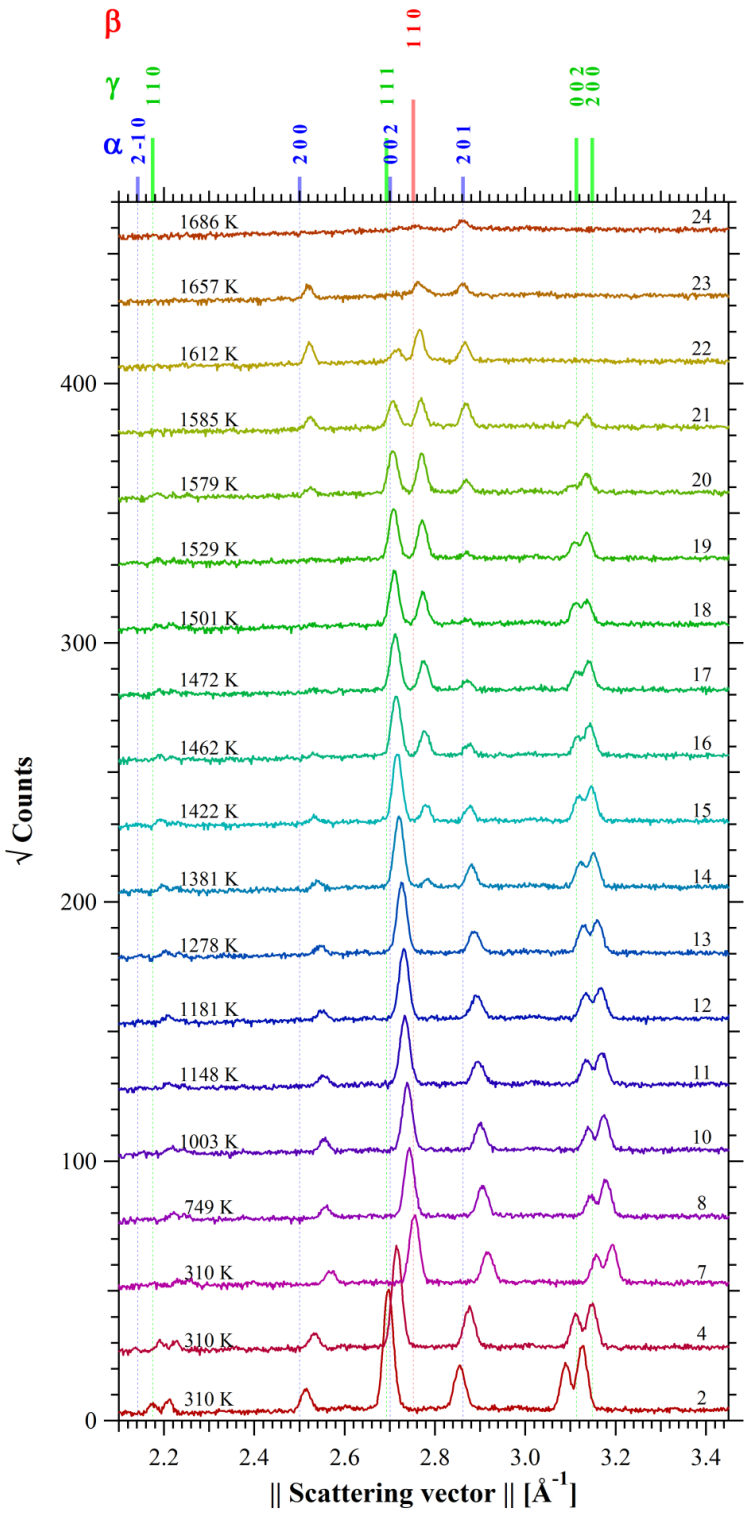

Figure 6.2 Measured diffraction patterns of a Ti-45Al-7.5Nb-0.25C alloy obtained under high pressure (9.6 GPa). Temperature tags are shown on the left and serial numbers on the right [10]. The first three patterns at 310 K were taken at pressures of 0, 3.2 and 9.6 GPa, respectively (based on [10] under CC-BY license).

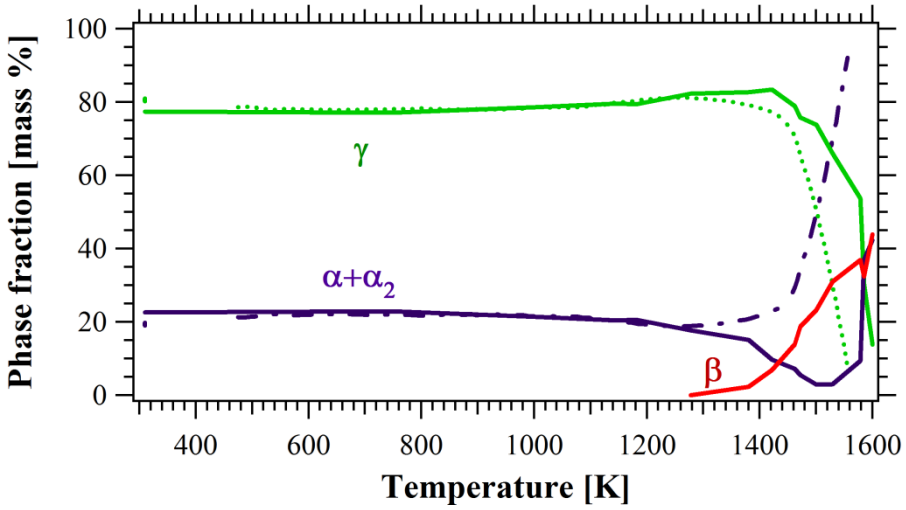

Figure 6.3 Phase evolution in a Ti-45Al-7.5Nb-0.25C alloy at a pressure of 9.6 GPa (continuous lines) (based on [10] under CC-BY license) compared with observations at standard atmospheric pressure (dotted lines) for a Ti-45Al-7.5Nb-0.5C alloy, replotted from Yeoh *et al.* [15].

Liss *et al.* [10] analyzed the lattice strain development in the Ti-45Al-7.5Nb-0.25C alloy at 310 K at three pressures, up to 9.6 GPa (series numbers 2, 4 and 7 in Figure 6.2). They calculated the changes in lattice parameter of the γ- and α_2/α-phases as a function of pressure at this temperature [10] and argued that at room temperature, the volume response to pressure is accommodated by the phase transformation $\gamma \rightarrow \alpha_2$, rather than by volumetric strain. They further determined some crystallographic aspects, specifically lattice strain and atomic order, at room temperature, but did not determine lattice strain evolution during heating at high pressure, which is subject of the current project. It is the dearth of information of this parameter, critical to processing at high temperature and pressure, which prompted this part of the present investigation.

The overarching aim of the present work was the re-visit of the experimental data of both experiments [10, 15] in order to compare the behavior of the selected alloys under atmospheric and high pressure respectively.

The specific aims were:

- to determine the lattice parameter evolution as a function of temperature at atmospheric pressure in the Ti-45Al-7.5Nb-0.5C alloy.

- to determine lattice parameter evolution as a function of temperature under high hydrostatic pressure in the Ti-45Al-7.5Nb-0.25C alloy.

It will be shown below that the experimentally determined lattice parameter evolutions occur in response to thermal expansion, alloy element segregation, order parameter and pressure. The specific trends and values will be decomposed based on an understanding of strain evolution with reference to the reported phase diagram at atmospheric pressure, before interpreting the evolution in the unknown system under high pressure. These new insights are opening new pathways to better understand structural transformations in the experimentally confined system. Such understanding is an essential element in optimizing the intended production techniques of titanium-aluminides since microstructural stability plays an important role in determining processing parameters.

6.2 Experiments

Lattice strain evolutions were calculated from the raw data of two earlier experiments:

- Yeoh *et al.* [15] conducted *in-situ* high-energy X-ray diffraction studies under proposal number MA-77 at the ID15B beamline at the ESRF in Grenoble using a two-dimensional detector. They ramped up a Ti-45Al-7.5Nb-0.5C alloy from room temperature to 1375 K at a rate of 5 K/min before ramping down to a rate of 2 K/min. Once a temperature of 1675 K was reached, it was maintained for 5 minutes before cooling down to room temperature at a rate of 5 K/min. All details of the experiment have been described by Yeoh *et al.* [15].

- Liss *et al.* [10] conducted *in-situ* X-ray diffraction studies at the BL04B1 beamline at the modern synchrotron source SPring-8 [22, 23] and a detailed account of the experimental procedures is to be found in their paper [10]. Because of the novelty in the field, it is pertinent to briefly refer to the most important aspects of the experiment. They used a Kawai-type multi-anvil press, SPEED-Mk.II, with a nominal maximum force of 15 MN. A pressure cell within an integrated resistance-heating furnace was designed in order to provide the capability of heating the specimen up to its melting point under a pressure of 9.6 GPa. Energy-dispersive X-ray diffraction with a beam size of $0.5 \times 0.7\ mm^2$ and a diffraction angle $2\theta = 5.9827°$ has been recorded by a 10 mm thick germanium solid-state detector. The setup is limited to an effective diffraction range of ~1.8 to 7.5 $Å^{-1}$. It is important to point out that a systematic experimental error in the pressure can creep in during the *in-situ* experiment due to pressure release at high temperature as a result of the softening of the anvil gasket material (see section 3.2.3).

Both single peak fitting and Rietveld refinement, using the MAUD program, were conducted to extract lattice parameters and phase fractions from the diffraction patterns obtained in these two experiments. The *Igor Pro 4* software (WaveMetrix, Lake Oswego, OR, USA) was then used to calculate the lattice strains and to perform curve fitting.

The two titanium-aluminides of nominal chemical composition Ti-45Al-7.5Nb-0.25/0.5C used in the present study were produced by the same metallographic preparaton procedures [24], as described in Chapter 5. Both alloys were characterized by Chladil *et al.* [1, 21] and the resulting microstructure at room temperature consists of a globular γ-phase and lamellar ($\alpha_2 + \gamma$) two-phase colonies [1].

While the experimental settings are described in the references above, it is pertinent to raise

an error estimate at this point, particularly to validate the later described lattice parameter fluctuations and features of the present manuscript. While the atmospheric pressure data in angle-dispersive setting appear as smooth curves, due to much faster and therefore finer sampling, the high-pressure data has been undertaken on temperature holding steps with larger step size, representing sometimes larger jumps between them, which could be interpreted as error fluctuations. Care has been taken by validating the realty of such jumps re-visiting the original data - i.e. looking out for changes of peak shape, overlapping etc. and by the two kinds of fitting analysis both Rietveld and single peak. We come up with the following estimate of error, demonstrating the trend of the features we discuss on lattice strain evolution:

- For the high-pressure setup [10] the energy calibration based on fluorescence lines of Mo, Pb, Au, Ag, Pt, Ta and Cu and single peak fitting (see below) has been calibrated to and accuracy of ~1E-4. Subsequently, the diffraction angle was calibrated using MgO and Au as standard materials at ambient conditions.

- At 1278 K, the single Gaussian fitted absolute peak positions for the [γ-111, α_2-201] reflections are [2.73, 2.89] $Å^{-1}$ (we reproduce only 3 digits in this text, however error propagation used full numerals) with an error of [5.49E-5, 1.8E-4] $Å^{-1}$ resulting in $\Delta G/G$ of [2.0E-5, 6.2E-5]. Similar results are obtained at 1612 K, also for the β-110 reflection with a value of $\Delta G/G$ = 3.9E-5.

- Moreover, we are interested in strain values rather than absolute values which propagates the errors and evaluates to double the $\Delta G/G$ uncertainties, resulting in about ~(1-2)E-4.

- Rietveld refinement reported inaccuracies of lattice parameter determinations as represented in the subsequent plots. They are mostly consistent with the error

estimation by single peak fitting, however Rietveld error bars diverge for the α_2/α-phase around 1500 K because of the weakness of some of their peaks.

Note moreover, physically meaningful errors may originate from drifts in temperature or pressure, and it will be discussed below. Significant drifts during a particular holding step were excluded, which would otherwise express in peak shape and broadening. Single-peak fitting of the α_2-201 reflection has been performed and confirms the trends with an error of ~3E-4, even in the range around 1500 K, allowing a qualitative interpretation of peak shifts due to various lattice variations, such as change of phase composition, disorder transformation etc. as will be discussed below.

6.3 Results

6.3.1 Lattice strains at standard atmospheric pressure

The evolving lattice strains were calculated by equation (1),

$$\varepsilon = \varepsilon_{hkl} = (G_0 - G)/G_0 \quad (1)$$

For a given reflection, G_0 are the reciprocal lattice vectors at 300 K and G are the measured values at increasing temperature. The lattice strain discussed below is not an absolute lattice strain but is merely the difference in strain with respect to a reference value at 300 K. Lattice strains of the Ti-45Al-7.5Nb-0.5C alloy at standard atmospheric pressure are shown in Figures 6.4 and 6.5 for the co-existing phases, α_2/α and γ, respectively. Both figures display an initial linear relationship between lattice strain and temperature which then evolves abnormally and anisotropically. Also shown is the average lattice strain, expressed as $\Delta V/3V$ of the atomic volume expansion ($\Delta V/V = 2\Delta a/a + \Delta c/c$), as a function of temperature. The

changes in lattice strain can be divided into four distinct temperature regions, which we discuss for each phase.

6.3.1.1 The α_2/α-phase

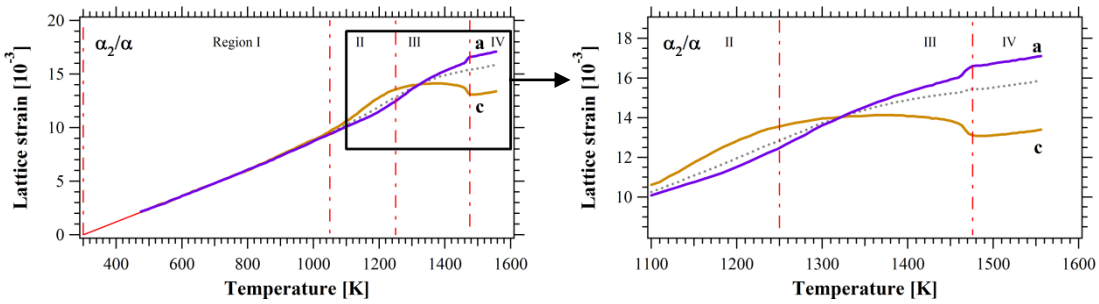

Figure 6.4 Dependence of the lattice strains in the α_2/α-phase along the a- and c-directions (purple and brown respectively) as well as 1/3 of volumetric expansion (dotted curve), as a function of temperature in a Ti-45Al-7.5Nb-0.5C alloy at standard atmospheric pressure.

In region I, strain evolution in both *a*- and *c*-directions is linear. In region II, the strains increase gradually to higher values than can be accounted for by linear thermal expansion alone. The lattice strain along the *a*-direction in region III increases more rapidly than in region II whereas it remains nearly constant along the *c*-direction, even under the influence of the counter-balanced thermal expansion. Region IV is characterized by a distinct kink in the strains of both lattice parameters at 1476 K [15], presumably as a result of the occurrence of the reverse eutectoid reaction $\alpha_2 \rightarrow \alpha$. Following these sudden changes, the strain increases gradually with an increase in temperature.

6.3.1.2 The γ-phase

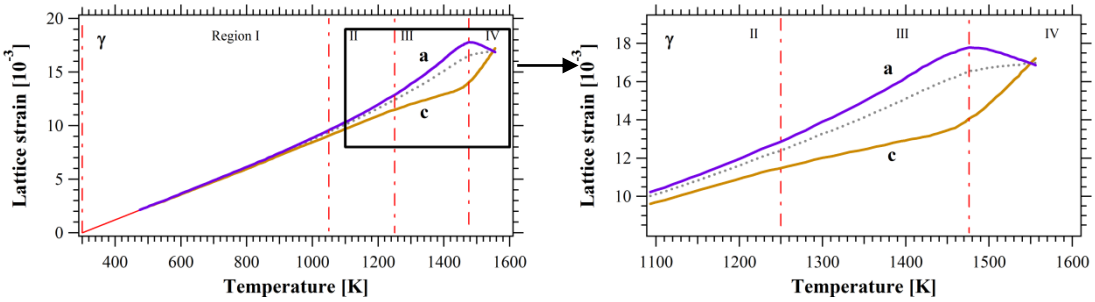

Figure 6.5 Lattice strains in the γ-phase along the *a*- and *c*-directions (purple and brown) as well as 1/3 of the volumetric expansion (dotted curve), as a function of temperature in a Ti-45Al-7.5Nb-0.5C alloy at standard atmospheric pressure.

The lattice strain evolution of the γ-phase is shown in Figure 6.5 in both the *a*- and *c*-directions, together with the weighted average (1/3 of the volumetric strain).

In region I, the strain evolution of the γ-phase is similar to that in the α_2/α-phase. In region II, the strain in both the *a*- and *c*-directions increases almost linearly since the dominant contributing factor to lattice strain is thermal expansion. In region III, the strain in the γ-phase along the *a*-direction increases up to T_{eu} whereas the strain in the *c*-direction increases to a lesser extent, developing significant anisotropy. In region IV, the strain in the *a*-direction decreases while the strain in the *c*-direction increases. The volumetric strain deviates only slightly from linearity and at the $T_{\gamma,solv}$ of 1565 K, all strain components meet as if they had expanded isotropically and linearly from room temperature.

6.3.2 Lattice strain at high pressure

The experimentally determined lattice strains of the α_2/α- and γ-phases are shown in Figures 6.6 and 6.7 for the Ti-45Al-7.5Nb-0.25C alloy under a pressure of 9.6 GPa. It is instructive to divide strain development into four regions.

Region I depicts the lattice strain evolution as a function of temperature in the range 300 K to

1003 K, where the α_2-phase has not yet reached thermodynamic equilibrium. Region II ranges from 1003 K to 1420 K ($T_{\gamma,max}$) and is divided into sub-regions II_a and II_b, separated by the appearance of the β-phase at 1350 K ($T_{\beta,start}$) [10]. Region III ranges from 1420 K to 1510 K (T_{eu}), while region IV covers the temperature range above 1510 K.

6.3.2.1 The α_2/α-phase

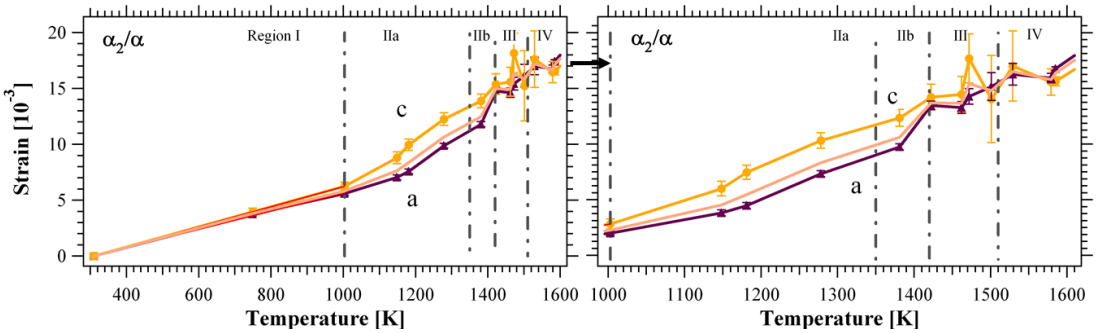

Figure 6.6 Lattice strains in the α_2/α-phase along *a*-(purple), *c*-(brown) directions and 1/3 of volumetric expansion (pink) as a function of temperature (K) for a Ti-45Al-7.5Nb-0.25C alloy at a nominal pressure of 9.6 GPa. The neighboring lattice strain points are connected by the straight line using "lines and markers" command in *Igor Pro 4*.

Figure 6.6 shows the lattice strain evolution of the α_2/α-phase along the *c*- and *a*-directions respectively. In region I, the lattice strain evolution is linear with respect to temperature. The strains along the *a*- and *c*-directions in region II increase more than those in region I. In region II_b, the slope of the strain-temperature curve along the *a*-direction is higher than that along the *c*-direction, indicating a decrease in the *c/a*-ratio. A significant increase in strain occurs at 1420 K (the $T_{\gamma,max}$). In region III, a maximum value of the lattice strain along *c*-direction is noticed at 1472 K. In region IV, the lattice strain increases in the *a*-direction while there is an erratic behavior in the *c*-direction.

6.3.2.2 The γ-phase

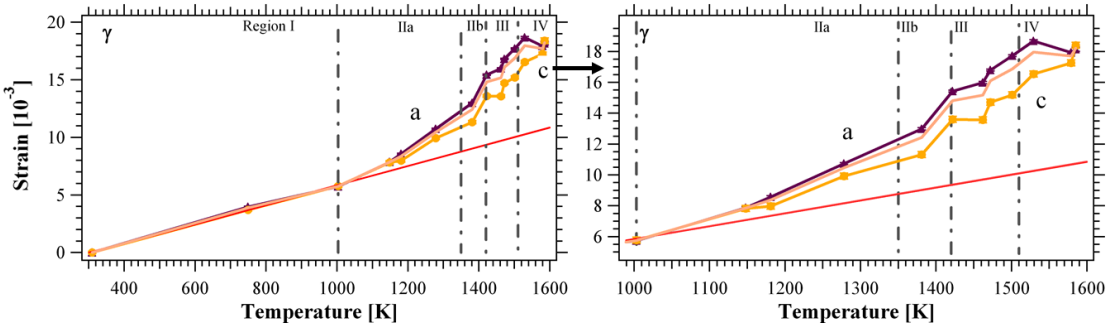

Figure 6.7 Lattice strain in the γ-phase along *a*- (purple), *c*- (brown) directions and 1/3 of volumetric expansion (pink curve) as a function of the temperature (K) for Ti-45Al-7.5Nb-0.25C at a nominal pressure of 9.6 GPa. The neighboring lattice strain points are connected by the straight line using "lines and markers" command in *Igor Pro 4*.

Figure 6.7 illustrates the lattice strain evolution of the γ-phase in the *a*- and *c*-directions, respectively. Noticeably, in region II_a, the strain increases more along the *a*-direction than in the *c*-direction, leading to a decrease of the *c/a*-ratio. In region II_b, the strain continues to increase but more so than in the previous region. In region III, the strain increases but not as steeply as in the region II_b. In region IV, the strain evolution trend is almost the same as under standard atmospheric pressure. The transformation temperatures T_{eu} and $T_{\gamma,solv}$ shift to higher temperatures at high pressure, evidenced by a comparison between Figures 6.5 and 6.7.

6.3.2.3 Experimental pressure release

During the experiments conducted at a hydrostatic pressure of 9.6 GPa, a progressive loss of sample pressure has been observed as a result of softening of the gaskets of the pressure cell at increasing temperature. Therefore, the sample pressure creeps down to about 6.9 ± 0.5 GPa over the time of the experiment, measured at 1473 K. This pressure loss of about 2.7 GPa has a marked effect on the absolute value of the measured crystal strain. In order to estimate the extent to which this pressure creep affects the quantitative values of the measured strain, the following analysis was conducted:

Experiments conducted at standard atmospheric pressure show that the volumetric lattice

expansion increases linearly with temperature as shown in Figures 6.4 and 6.5. However, when the experiments are conducted at high pressure, there is a significant deviation from linearity to larger strain values, as shown in Figures 6.6 and 6.7. This deviation is illustrated in Figure 6.7 where the red line shows the extrapolation of linear thermal expansion.

There is clearly a significant difference between this expected linear dependence of lattice strain development as a function of temperature and the experimentally observed volumetric values (pink curve). This deviation is most likely not due to differences in lattice strain, but is caused by thermally induced softening of the gaskets of the pressure cell as outlined above. Under atmospheric pressure, the linear extrapolation of thermal expansion meets closely the point of volumetric strain at $T_{\gamma,\mathrm{solv}}$, as shown in Figures 6.4 and 6.5. In order to assess this premise, the difference in strain was measured between the extrapolated linear thermal expansion and the average strain expressed by 1/3 volumetric strain (red and pink lines in Figure 6.7) at a temperature of 1579 K as 0.00702. Since the value of the bulk modulus is known, 152 GPa [10], the relation $\partial p = -K \cdot \partial V/V$ was used to calculate the pressure difference as 3.20 GPa. This calculated value of pressure release is in reasonable agreement with the experimentally measured decrease of 2.7 GPa in pressure measured following the heating cycle, thereby providing evidence that the observed deviation can indeed be attributed to the sample pressure release as a result of a leak in the seal of the pressure cell. The two pressure release values are particularly in good agreement taking into account that only the room temperature bulk modulus is available.

The values of strain shown in Figure 6.7 are therefore higher than the true values of lattice strain under 9.6 GPa by up to 25% and the isotropic lattice strain as a result of temperature change has to be estimated. However, the anisotropic part, as will be discussed later, is well

representative.

6.4 Discussions

In order to better understand how changes in lattice parameter influence microstructural evolution, account has to be taken of the factors contributing to such lattice strains. When the temperature increases, the strains in both crystallographic *a* and *c* directions increase, while an increase in the aluminium content in the respective phase results in a decrease in those strains. The order parameter is defined as $S = \frac{p-r}{1-r}$, where p is the probability that an atom resides in the ordered position r (The concept of the order parameter is discussed in more detail in the Appendix). The order parameter is a measure of the extent of anisotropic behavior: when either the α_2- or γ-phase develops an ordered structure, the strain along the *a*-direction decreases whereas that along the *c*-direction increases. A summary of the influence of the order parameter in the different temperature regions, is shown in Figures 6.8, 6.9, 6.11 and 6.13. It is to be noted that these figures only show the trend in strain (not the quantitative strain values).

6.4.1 Lattice strains at standard atmospheric pressure

Figure 6.8 shows how temperature, aluminium content and the order parameter affect strain evolution of the α_2/α-phase under standard atmospheric pressure. It is pertinent to discuss these observations:

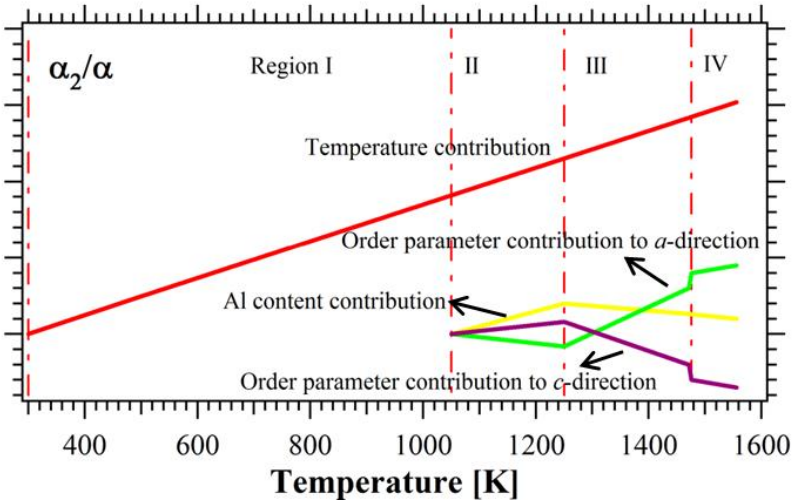

Figure 6.8 Factors contributing to lattice strain evolution in the α2/α-phase at standard atmospheric pressure.

Region I: lattice strain increases linearly with respect to temperature because the dominating contributing factor is thermal expansion, which, for most solids is proportional to the temperature change ΔT, with $\varepsilon_{thermal} = \eta \cdot \Delta T$ [25], where η is the linear thermal expansion coefficient. Region II: It is reasonable to assume that the high-temperature equilibrium concentration of aluminium has been 'frozen' into the alloy during manufacturing. This means that the aluminium concentration in α_2 is effectively higher than the equilibrium concentration at room temperature. With an increase in temperature, long-range diffusion of aluminium becomes possible, such that the α_2-phase is depleted in aluminium, effectively meaning that the titanium concentration in the α_2-phase increases. Higher concentrations of titanium lead to an increase in atomic volume [10] and hence, accounts for the observed increase in lattice strain as a function of temperature. Region III: The curvature of lattice strain evolution in the α_2/α-phase along the *a*- and the *c*-direction has different signs. This observation is ascribed to the occurrence of an order-disorder transformation (the order-disorder transformation is discussed in more detail in the appendix). Region IV: Both lattice strains ε_a and ε_c show a distinct, respectively positive and negative step change at the

boundary of regions (III) and (IV), coinciding with a sharp decrease in order parameter (see Figure A.2, Appendix A). It is important to note that the volume strain evolves smoothly, without a step-change. This observation provides evidence of the premise that the change of order does not affect the atomic volume, but only strain anisotropy.

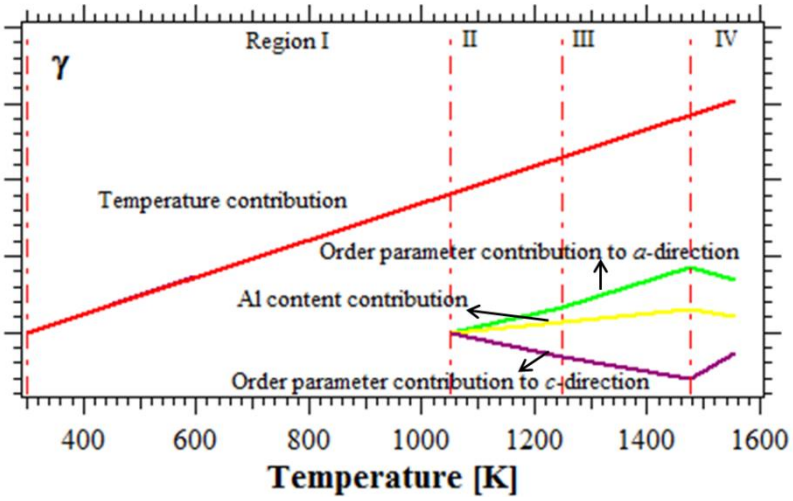

Figure 6.9 Factors contributing to lattice strain evolution in the γ-phase at atmospheric pressure.

Figure 6.9 shows how temperature, aluminium content and the order parameter affect strain evolution in the γ-phase at standard atmospheric pressure.

The thermal expansion is linear in region I along the *a*- and *c*- directions due to the linear temperature contribution. The small and anisotropic deviation from linearity in Region II is due to the extent to which aluminium contributes to the disordering of the TiAl-structure. It is observed that the lattice strain along the *a*-direction increases faster than along the *c*-direction, and since the *c*-dimension is larger than the *a*-dimension, the unit cell approaches more closely a *fcc* unit cell, that of a fully disordered γ-phase, revealing a higher degree of disorder and hence, a smaller order parameter. Witusiewicz *et al.* [26] have shown earlier that the aluminium concentration decreases well below stoichiometry as a function of temperature in this temperature range and that the lowest aluminium concentration in the γ-phase is

attained at 1476 K, contributing to chemical disorder. Above 1476 K (in region IV), the aluminium content in the partially ordered γ-phase increases, as shown in Figure 6.10(a). Yeoh *et al.* [15] have shown that the *c*/*a* ratio decreases sharply with increasing temperature in Region III as shown in Figure 6.10(b). Hence, the strain along the *a*-direction increases more than in the *c*-direction and the TiAl-structure becomes highly disordered. In region IV, the *c*/*a* ratio increases sharply as shown in Figure 6.10(b) and the fully ordered TiAl-structure is approximated, due to the highest ordering energy of the γ-phase, compared to all other Ti-Al configurations [27].

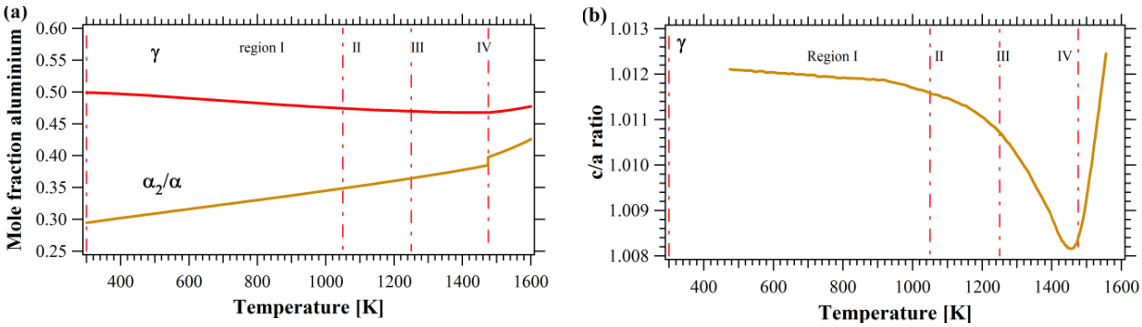

Figure 6.10: (a) Aluminium concentrations of the γ- and α_2/α-phases as a function of temperature as dereived from the phase diagram [26]; (b) The *c*/*a* ratio of the α_2/α-phase for a Ti-45Al-7.5Nb-0.5C alloy at standard atmospheric pressure [15].

6.4.2 Lattice strains at high pressure

Figure 6.11 shows the trend in the strain evolution by the respective contributions of temperature, aluminium content in the respective phases, order parameter and pressure in the different regions for the α_2/α-phase at a nominal pressure of 9.6 GPa. In order to avoid bias from the experimental pressure release, we calculate the anisotropic part of strain ($\Delta a/a - \Delta V/3V, \Delta c/c - \Delta V/3V$) as shown in Figure 6.12 for the α_2/α-phase. The main features of the strain evolution of the α_2/α-phase at 9.6 GPa are illustrated as follows:

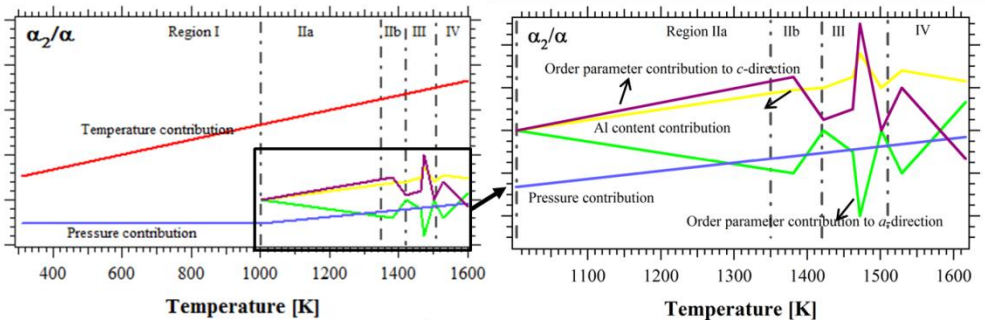

Figure 6.11 Contributors to strain evolution of the α_2/α-phase at nominal pressure of 9.6 GPa.

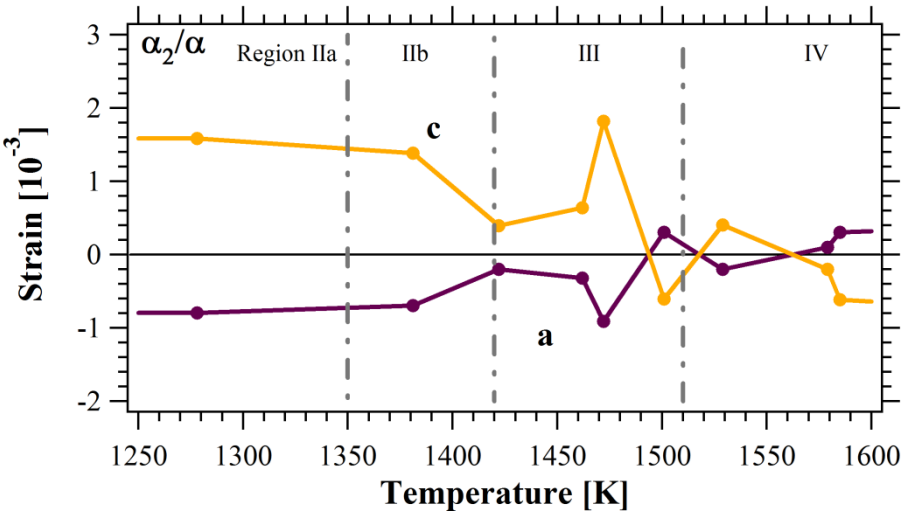

Figure 6.12 Anisotropic lattice strains of the α_2/α-phase along the *a*- (purple) and *c*- (brown) directions for the Ti-45Al-7.5Nb-0.25C alloy at 9.6 GPa. The neighboring lattice strain points are connected by the straight line using "lines and markers" command in *Igor Pro 4*.

In region II_b the anisotropic strain increases in the *a*-direction and decreases in the *c*-direction. These observations are attributed to the order-disorder transition in the α_2/α-phase. In region III, the β-phase exists. The strain evolution under a pressure of 9.6 GPa is in the opposite direction in the temperature range 1420 K to 1472 K than observed under standard atmospheric conditions at the beginning of region III (see Figure 6.4). There is a steep increase along the *c*-direction between 1462 K and 1472 K, corresponding to the increase of the β-phase fraction (see Figure 6.3). The β-phase in solid solution has a *bcc* structure and provides an opportunity for the co-existing α_2-phase to drive closer to stoichiometry and

order, increasing its *c*/*a* ratio. Moreover, under the assumption that β orders to β_o with a B2 structure, the latter would extract aluminium from α_2, again emphasizing that there is a higher degree of order in the latter. The transformation to β leads to a sharp decrease in the aluminium content of the supersaturated α_2/α-phase and hence, the α_2/α-phase becomes increasingly ordered. The change in the fraction of β-phase has a major influence on the aluminium concentration in the α_2/α-phase from region III onwards. These arguments explain why the trend of the anisotropic strain in the α_2/α-phase correlate well with the β-phase evolution. By contrast, the main contributor is a thermally driven $\alpha \rightarrow \alpha_2$ order-disorder transition in region III under standard atmospheric pressure. The maximum value of anisotropic strain along the *c*-direction at 1472 K is probably driven by the appearance of an ordered β_o-phase, leading to a lower aluminium content in the α_2/α-phase. Under a pressure of 9.6 GPa, 1510 K, is taken as eutectoid temperature, as was reported by Liss *et al.* [10]. It indicates that under high pressure the eutectoid temperature would be increased. On approach to 1510 K, the order-disorder transition $\alpha \rightarrow \alpha_2$ occurs, the order parameter of the α_2/α-phase decreases, which results in a significant increase in the strain in the α_2/α-phase along the *c*-direction. In region IV, up to 1529 K, the β-phase fraction increases sharply (Figure 6.3), leading to an increase along the *c*-direction and a decrease in *a*-direction in the α_2/α-phase, although this premise might be questioned, since there is some uncertainty about the accuracy of experimental measurements as indicated by the relatively large error bars. At higher temperature, the anisotropic strain along the *a*-direction increases while that along the *c*-direction decreases.

Figure 6.13 shows how temperature, aluminium content, order parameter and pressure contribute to strain evolution in the γ-phase at a nominal pressure of 9.6 GPa in the different

regions respectively. Because of this observed pressure loss, the anisotropic part of strain, ($\Delta a/a - \Delta V/3V$, $\Delta c/c - \Delta V/3V$) of the γ-phase is shown in Figure 6.14. The sample pressure is from 9.6 GPa to 6.9 GPa – a very similar order of magnitude which would not considerably change the phase transformation behavior. Moreover, this anisotropic part of lattice strain is subtracted by the pressure influence ($\Delta V/3V$), but relevant features with respect to order parameter are still valid in this part. The significant jumps in lattice parameter are linked to phase transformations and not to the experimental pressure release. The main features of the strain evolution in the γ-phase at a nominal pressure of 9.6 GPa are discussed below:

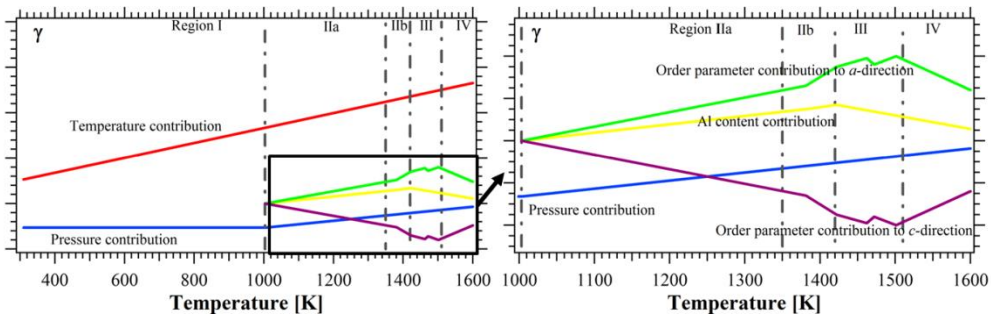

Figure 6.13 Contributors to strain evolution of the γ-phase at nominal pressure of 9.6 GPa.

In region III, the transition of γ → α → β + α [10] results in an increased aluminium content in the γ-phase, therefore, the strain increase is lower compared to atmospheric pressure. The kink at 1472 K is attributed to the order parameter increase as a result of the fact that the γ-phase fraction decreases sharply in the temperature range 1462 to 1472 K. In region IV, the trend in strain evolution is almost the same as at atmospheric pressure, since the main contributing factor is the order parameter.

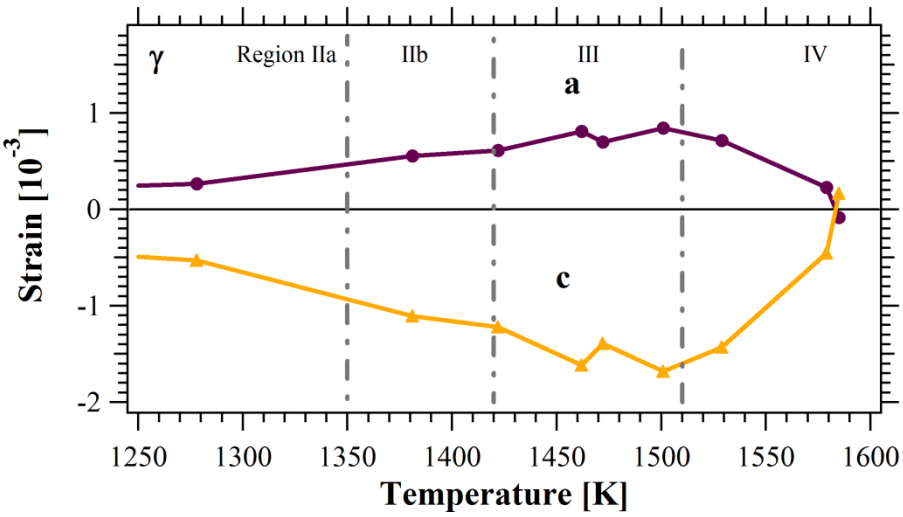

Figure 6.14 Dependence of the anisotropic lattice strain in the γ-phase along *a*- (purple), *c*- (brown) directions for Ti-45Al-7.5Nb-0.25C at 9.6 GPa. The neighboring lattice strain points are connected by the straight line using "lines and markers" command in *Igor Pro 4*.

6.4.3 Phase sequence at high pressure

Based on our experimental observations and the Rietveld analyses outlined above, a new version of the sequence of phase changes occurring in the Ti-Al-7.5Nb-0.25C alloy under a pressure of 9.6 GPa, is shown in Figure 6.15 in the region of the alloy composition (delineated by the area between the two vertical dotted lines). This is the first experimental evidence suggesting that during heating under high pressure the sequence of phase development is $\alpha_2+\gamma$, $\alpha_2/\alpha+\gamma$, $\alpha_2/\alpha+\gamma+\beta$, $\alpha+\gamma+\beta$, $\alpha+\beta$, $L+\alpha+\beta$, $L+\beta$ and liquid L. Compared to the phase diagram suggested by Chladil *et al*. [17], it is evident that the temperature range of the phase field $\alpha_2/\alpha+\gamma+\beta$ is extended under the influence of a pressure of 9.6 GPa.

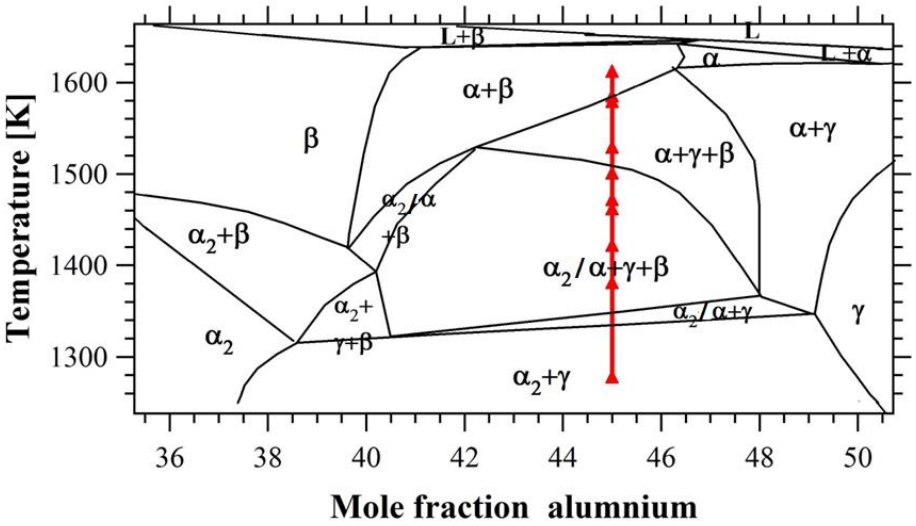

Figure 6.15 Proposed sequence of phase changes upon heating a Ti-Al-7.5 Nb-0.25C alloy under a pressure of 9.6 GPa. The red triangles are the experimental temperature, where the phase region are based on the calculations of this study from the diffraction measured by Liss *et al.* [10], superimposed on a section of a schematic diagram of the phase compositions in the Ti-Al-7.5Nb-0.25C system.

6.4.4 Comparison of the observations at low and high pressure

The quantitatively calculated contributions to strain evolution at standard atmospheric pressure are listed in Table 6.1.

Table 6.1 Contribution to strain evolution at standard atmospheric pressure.

Phase	Strain direction	Expansion coefficient η [10^{-6} K^{-1}]	Increasing Al content [10^{-6} mol^{-1}]	Atomic order S (0→1) [10^{-6}]
α_2/α	*a*	⇑ 12.075	⇓	⇓-695
	c	⇑ 12.047	⇓	⇑ 1390
	V/3	⇑ 12.066	⇓ -18959	⇔
γ	*a*	⇑ 12.412	⇓	⇓-4677*
	c	⇑ 11.847	⇓	⇑ 9420*
	V/3	⇑ 12.224	⇓-24079	⇔

* Computed with lattice parameter values of Beaven [28]

The linear thermal expansion coefficients are $\eta_a = 12.075 \cdot 10^{-6}\ K^{-1}$ and $\eta_c = 12.047 \cdot 10^{-6}\ K^{-1}$ for α_2/α-phase and $\eta_a = 12.412 \cdot 10^{-6}\ K^{-1}$ and $\eta_c = 11.847 \cdot 10^{-6}\ K^{-1}$ for γ-phase. They were extracted by fitting the curves of *a*- and *c*- directions in region I of Figures 4 and 5, since thermal expansion is proportional to the temperature change for most solids, $\varepsilon_{thermal} = \eta \cdot$

ΔT [25, 29]. In order to calculate the contribution of the aluminium content of the α_2/α-phase, the slope of the strain (Figure 6.4 and Figure 6.5) and the slope of the phase boundary lines (Figure 6.10(a)) in region IV were used since the thermal expansion and the aluminium content both contribute to volumetric strain evolution in this region. The contribution of aluminium to the lattice strains are $\partial\varepsilon/\partial C|_\alpha = -18959\cdot10^{-6}$ mol^{-1} and $\partial\varepsilon/\partial C|_\gamma = -24079\cdot10^{-6}$ mol^{-1} respectively, in good agreement with the values reported by Dubrovinskaia *et al.* [30]. It should be noted that the thermal expansion coefficient at high temperature will differ from the values obtained by diffraction, as further factors may contribute, such as the creation of lattice vacancies which do not change the lattice plane spacing but the length and volume of a specimen. The order parameter contributions are $\partial\varepsilon/\partial S_a = -695\cdot10^{-6}$ and $\partial\varepsilon/\partial S_c = 1390\cdot10^{-6}$ for the α_2/α-phase along *a*- and *c*- directions respectively. The experimental data points around the γ-solvus at 1476 K, were chosen to calculate $\partial\varepsilon/\partial S$ for each component. In Figure 6.4, the steps across these data are $0.45\cdot10^{-3}$ and $0.5\cdot10^{-3}$ for *a*- and *c*- directions respectively, which are recorded as $\Delta\varepsilon_a^M$ and $\Delta\varepsilon_c^M$ below. Considering that $\Delta\varepsilon_a^M$ and $\Delta\varepsilon_c^M$ are not only influenced by the order parameter, but also by volume expansion, these equations were modified as follows:

$$\Delta\varepsilon_a = \Delta\varepsilon_a^M - \Delta\varepsilon_v,$$

$$\Delta\varepsilon_c = \Delta\varepsilon_a^M - \Delta\varepsilon_v$$

where $\Delta\varepsilon_v$ represents the slope of the average expansion, i.e. 1/3 of the volume expansion curve. From Figure A.2, the slope of the order parameter (ΔS) across this step is 0.456, resulting in $\partial\varepsilon/\partial S_a = \Delta\varepsilon_a/\Delta S = -695\cdot10^{-6}$ and $\partial\varepsilon/\partial S_c = \Delta\varepsilon_c/\Delta S = 1390\cdot10^{-6}$. The order parameter of the γ-phase was estimated in a different way, since neither the order parameter

nor site occupation has been evaluated by Yeoh *et al.* [15]. The fully disordered γ-phase would be *fcc* with a *c*/*a* axis ratio of one, and the atomic volume is conserved during the order-disorder phase change. The lattice parameters of the stoichiometric alloy have been reported by Beaven and Pfullman [28] and extracted as a_{50} = 4.0176 Å and c_{50} = 4.0745 Å, for the fully ordered crystal structure.

$$a_{fcc} = \sqrt[3]{a_{50}{}^2 \times c_{50}}$$

leading to a_{fcc} = 4.03648 Å. When the crystal structure changes from a disordered (S = 0) to a fully ordered structure (S = 1), the influence of the structure parameter on strain development is calculated as $\partial\varepsilon/\partial S_a = (a_{50} - a_{fcc})/\, a_{fcc} = -4677 \cdot 10^{-6}$ and $\partial\varepsilon/\partial S_c = (c_{50} - a_{fcc})/a_{fcc} =$

$9420 \cdot 10^{-6}$, respectively.

Table 6.2 lists quantitative contributions to the strain evolutions at high pressure. The thermal expansion coefficients are calculated by linear curve fitting based on the strains in region I (Figures 6.6 and 6.7). They are $\eta_a = 8.126 \cdot 10^{-6}$ K^{-1}, $\eta_c = 9.030 \cdot 10^{-6}$ K^{-1} for the α_2/α-phase and $\eta_a = 8.371 \cdot 10^{-6}$ K^{-1}, $\eta_c = 8.359 \cdot 10^{-6}$ K^{-1} for γ-phase. The expansion coefficients are approximately 8×10^{-6} K^{-1} under a compressive pressure of 9.6 GPa whereas it is 12×10^{-6} K^{-1} at atmospheric pressure. Hence, a compressive pressure of 9.6 GPa decreases the expansion coefficient to 67% of the value at atmospheric pressure. An increase in the aluminium content in the respective phases would lead to a decrease in the strain along the *a*- and *c*- directions, as well as a decrease in the volumetric strain. The application of an applied compressive pressure caused the strain to decrease in both phases. Liss *et al.* [10] has already calculated the strain decrease in the α_2/α-phase per GPa is $2266 \cdot 10^{-6}$ along the *a*-direction and $2189 \cdot 10^{-6}$ along the *c*-direction from the same experimental data. The corresponding strain decrease in

the γ-phase is $2206 \cdot 10^{-6}$ along *a*-direction and $2293 \cdot 10^{-6}$ in the *c*-direction [10].

Table 6.2 Contributions to strain evolution at high pressure.

Phase	Strain direction	Expansion coefficient η [10^{-6} K^{-1}]	Increasing Al content	Pressure* [10^{-6} GPa^{-1}]
α_2/α	*a*	⇑ 8.126	⇓	⇓ 2266
	c	⇑ 9.030	⇓	⇓ 2189
	V	⇑ 8.427× 3	⇓	⇓ 2240 × 3
γ	*a*	⇑ 8.371	⇓	⇓ 2206
	c	⇑ 8.335	⇓	⇓ 2293
	V	⇑ 8.359× 3	⇓	⇓ 2235 × 3

*Calculations by Liss *et al.* [10]

6.5 Conclusions

Lattice strain evolution in a Ti-45Al-7.5Nb-0.5C and a Ti-45Al-7.5Nb-0.25C alloy were determined by *in-situ* experiments using high-energy X-rays at synchrotron storage rings. The temperature dependence of lattice strain evolution of the Ti-45Al-7.5Nb-0.5C alloy was studied at atmospheric pressure while the lattice strain evolution in a Ti-45Al-7.5Nb-0.25C was determined as a function of temperature under a compressive pressure of 9.6 GPa.

- Lattice strain evolution is determined by thermal expansion, changes in the aluminium content of the respective phases and the extent to which the respective phases are ordered under atmospheric pressure. Their interaction and respective quantitative values to lattice strain changes have been obtained, which provides valuable data to predict strain evolution in the future.

- Pressure has a determining influence on strain evolution in the alloys. A consequence of this finding is that the magnitude of the lattice strain can be manipulated by these four factors during manufacture. Hence, inter-granular stresses can be reliably predicted, minimized and controlled in order to manipulate the mechanical properties of candidate titanium aluminide alloys.

- The application of high pressure increases the eutectoid temperature T_{eu} and the temperature at which the transformation of the γ-phase is completed, $T_{\gamma,solv}$.

- The linear thermal expansion coefficient of the alloy investigated is about 1/3 (4×10^{-6} K^{-1}) lower under a pressure of 9.6 GPa, than under standard atmospheric pressure.

- Based on the experimental observations, a new version of the sequence of phase changes occurring at high pressure is proposed and illustrated with reference to a schematic phase

diagram. This portion of the phase diagram shows that under high pressure, the (α_2/α + γ + β) phase field is stabilized over a wide range of temperature.

- Lattice strains can be used to indicate the occurrence of phase transformations and changes in composition, which are otherwise difficult to determine.
- The *c*/*a* ratio of both the α_2/α- and γ- phases provides valuable insight into the extent to which these phases are ordered (as assessed by the order parameter).
- A discontinuity in the *c*/*a* ratio is an indication of the order-disorder transition $\alpha_2 \rightarrow \alpha$.

The present findings are of generic importance with respect to lattice parameter evaluation and are relevant to a multitude of intermetallic systems.

6.6 Reference

[1] Chladil, H.F., et al., Experimental studies and thermodynamic simulation of phase transformations in high Nb containing γ-TiAl based alloys. International Journal of Materials Research, 2007. **98**(11): p. 1131-1137.

[2] Li X.-S. e. al, "Structural and Thermodynamic Properties of TiAl intermetallics under High Pressure," Commun. Theor. Phys., 2012. 57: p. 141.

[3] Zhang, C., Hou, H., Zhao, Y., Yang, X. and Guo, Y., First-principles study on structural, elastic and thermal properties of γ-TiAl and α 2-Ti3Al phases in TiAl-based alloy under high pressure. International Journal of Modern Physics B, 2017. **31**(11): p.1750079.

[4] Appel, F., J.D.H. Paul, and M. Oehring, Gamma titanium aluminide alloys: science and technology. 2011: John Wiley & Sons.

[5] Khan, K., et al., Development of third generation castable gamma titanium aluminides: role of solidification paths. 1997.

[6] Jin, Y., et al., Microstructure refinement of cast TiAl alloys by β solidification. Scripta Materialia, 2004. **51**(2): p. 113-117.

[7] Liss, K.-D., et al., In situ study of dynamic recrystallization and hot deformation behavior of a multiphase titanium aluminide alloy. Journal of Applied Physics, 2009. **106**(11): p. 113526.

[8] Clemens, H. and S. Mayer, Design, processing, microstructure, properties, and applications of advanced intermetallic TiAl alloys. Advanced Engineering Materials, 2013. **15**(4): p. 191-215.

[9] Clemens, H., et al. Advanced β-Solidifying Titanium Aluminides–Development Status and Perspectives. in MRS Proceedings. 2013. Cambridge Univ Press.

[10] Liss, K.-D., et al., Hydrostatic Compression Behavior and High-Pressure Stabilized β-Phase in γ-Based Titanium Aluminide Intermetallics. Metals, 2016. **6**(7): p. 165.

[11] Tapan Chatterji, K.-D.L., and Thomas Tschentscher, Anomalous Thermal Expansion Due to Magnetism in EuAs3 and MnS2. ESRF Highlights, 1997.

[12] Chatterji, T., et al., The ground state of NaV2O5. Solid state communications, 1998. 108(1): p. 23-26.

[13] Liss, K.-D., et al., High-energy X-rays: a tool for advanced bulk investigations in materials science and physics. Textures and Microstructures, 2003. **35**(3-4): p. 219-252.

[14] Yan, K., et al., In Situ Characterization of Lattice Structure Evolution during Phase Transformation of Zr‐2.5 Nb. Advanced Engineering Materials, 2011. **13**(9): p. 882-886.

[15] Yeoh, L.A., et al., In situ high-energy X-ray diffraction study and quantitative phase analysis in the α+ γ phase field of titanium aluminides. Scripta Materialia, 2007. **57**(12): p. 1145-1148.

[16] Schuster, J.C. and M. Palm, Reassessment of the binary aluminum-titanium phase diagram. Journal of phase equilibria and diffusion, 2006. **27**(3): p. 255-277.

[17] Chladil, H.F., et al., Experimental Studies of Phase Transformations in a Carbon Containing Ti‐45Al‐7.5 Nb Alloy and Related Thermodynamic Simulations. Advanced Engineering Materials, 2005. **7**(12): p. 1131-1134.

[18] Shull, R.D. and J.P. Cline, High temperature X-ray diffractometry of Ti-Al alloys, in Materials Chemistry at High Temperatures. 1990, Springer. p. 95-117.

[19] Lutterotti, L., Total pattern fitting for the combined size–strain–stress–texture determination in thin film diffraction. Nuclear Instruments and Methods in Physics Research Section B: Beam Interactions with Materials and Atoms, 2010. **268**(3): p. 334-340.

[20] Lutterotti, L., S. Matthies, and H. Wenk. MAUD (Material Analysis Using Diffraction): a user friendly Java program for Rietveld texture analysis and more. in Proceeding of the twelfth international conference on textures of materials (ICOTOM-12). 1999. NRC Research Press Ottowa, Canada.

[21] Chladil, H., et al., Phase transformations in high niobium and carbon containing γ-TiAl based alloys. Intermetallics, 2006. **14**(10): p. 1194-1198.

[22] Higo, Y.T.a.Y., BL04B1: In situ observation of high pressure phase change of simple material. Sep. 2007 Spring-8, Kouto, Kyogo, Janpan, Tutorial 4.

[23] Katsura, T., et al., A large-volume high-pressure and high-temperature apparatus for in situ X-ray observation,'SPEED-Mk. II'. Physics of the Earth and Planetary Interiors, 2004. **143**: p. 497-506.

[24] Gerling, R., H. Clemens, and F.P. Schimansky, Powder Metallurgical Processing of Intermetallic Gamma Titanium Aluminides. Advanced Engineering Materials, 2004. **6**(1-2): p. 23-38.

[25] Abe, F., T.-U. Kern, and R. Viswanathan, Creep-resistant steels. 2008: Elsevier.

[26] Witusiewicz, V., et al., The Al–B–Nb–Ti system: IV. Experimental study and thermodynamic re-evaluation of the binary Al–Nb and ternary Al–Nb–Ti systems. Journal of Alloys and Compounds, 2009. **472**(1): p. 133-161.

[27] Asta, M., D. de Fontaine, and M. Van Schilfgaarde, First-principles study of phase stability of Ti–Al intermetallic compounds. Journal of materials research, 1993. **8**(10): p. 2554-2568.

[28] Beaven, P. and T. Pfullmann, Stoichiometry effects in TiAl and TiAlCr alloys. Journal of materials science & technology, 1994. **10**(5): p. 321-330.

[29] Bauchau, O.A. and J.I. Craig, Structural analysis: with applications to aerospace structures. Vol. 163. 2009: Springer Science & Business Media.

[30] Dubrovinskaia, N., et al., Absence of a pressure-induced structural phase transition in Ti 3 Al up to 25 GPa. Physical Review B, 2000. **63**(2): p. 024106.

Chapter 7. Phase transformation and structure evolution of a Ti-45Al-7.5Nb alloy processed by high-pressure torsion

7.1 Introduction

It is interesting to find the changes in phase transformations and a three phase-region when the selected Ti-Al alloys is exposed to high pressure during heating, detailed in Chapter 6. It is thus interesting to examine what will happen if the Ti-Al alloys are exposed to sever plastic deformation such as high pressure torsion. Although niobium alloyed, γ-based Ti-Al alloys (TNB) exhibit excellent specific strength and ductility [1-3], they are however brittle at room temperature. They consist of an *fcc*-based, ordered γ-phase, TiAl, of $L1_0$ structure and space group 123 of P 4/m m m and an *hcp*-based, ordered α_2-phase, Ti_3Al, of $D0_{19}$ structure and space group 194 of P 6_3/m m c, which can further disorder to *hcp* a-Ti solid solution of same space group. The design of a processing route that will further improve the plasticity and ductility of these TNB alloys remains a challenge to researchers and engineers. One possible approach to overcome this inherent brittle behaviour is to reduce the grain size [4]. Processing by the application of severe plastic deformation is one suggested approaches aimed at effective grain refinement [5]. Among the numerous severe processing deformation techniques, high-pressure torsion (HPT) is recognized as an effective grain refinement tool and the principles on which this technique is based, are well documented elsewhere [6]. Accordingly, earlier research has demonstrated that HPT processing can reduce the grain size of Ti-Al alloys to the micrometer or even nanometer scale [7-9]. By reference to the well-known Hall-Petch relation [10], the yield strength will increase accordingly, although it has to be borne in mind that this relationship breaks down at very small grain sizes. In addition,

material with a nano-sized grain structure is likely to display superior plastic behavior, which prompted an assessment of the mechanical properties of selected HPT-processed titanium aluminides in the present study. In earlier investigations, mechanical properties were assessed by Vickers micro-hardness measurements [9], while other researchers employed compression tests on micro-pillars [11] and nano-indentation measurements [12].

In addition to grain refinement, different research groups have provided convincing evidence of phase evolution in the course of high-pressure torsion processing of Ti-Al alloys [7-9]. However, the details of the relevant phase changes occurring during processing are still a matter of debate and the role strain is playing, has not been resolved as yet. Korznikov *et al.* [7] reported that the γ-phase in HPT-treated Ti-Al alloys transforms into disordered states. Moreover, a fraction of the γ-phase transforms into α-phase, with a hexagonal close packed crystal structure. Kazantseva *et al.* [8] observed that the phase transformation occurs in Ti_3Al intermetallic compounds (α_2-phase) by a shear mechanism under the application of high pressure. Conversely, Srinivasarao *et al.* [9] recently argued that high-pressure torsion does not produce an order/disorder phase transition in a γ-based Ti-Al alloy. Liss *et al.* [13] reported that a partial transformation of $\gamma \rightarrow \alpha_2/\alpha$ occurs under the influence of high pressure at room temperature despite the increase of volume per atom, driven by a large ordering energy in the γ-phase [14]. In a previous study, Han *et al.* [12], in which we used conventional X-ray diffraction analysis, pointed to a tendency towards the phase transformation $\gamma \rightarrow \alpha_2/\alpha$ in a Ti-45Nb-7.5Nb (at. %) alloy following HPT processing. However, the significance and the nature of this proposed phase change has not yet been established. Moreover, various apparently contradicting observations reveal the complexity of phase transitions in HPT-treated Ti-Al alloys. The fact that HPT processing produces

highly anisotropic and inhomogeneous specimens needs to be taken into account for texture and mechanical testing on the severely deformed bulk materials [15, 16].

X-ray and neutron diffraction techniques are commonly used to determine the phase composition and other crystallographic aspects in alloys, but for Cu-K_α X-ray diffraction, the absorption length and is usually about 10 μm, which is much shorter when compared to HEXRD and neutrons. Hence, this feature can be utilized to characterize different depths in a specimen upon layer-by-layer removal. However, it is difficult to distinguish between the ordered α_2- and the disordered α-phase by X-ray diffraction. The weak superstructure reflections and a low α_2-phase fraction can hardly be distinguished from the background and statistical noise. On the contrary, neutron diffraction techniques pose advantages in the detection of order/disorder phase transitions, demonstrated by Watson *et al.* [17] as well as Kabra *et al.* [18], and recently reviewed by Liss [19]. The deep attenuation length of neutron diffraction enables bulk averaging by deep penetration of the neutrons and fast measurements [20-24]. For example, Watson *et al.* and Kabra *et al.* observed the order-disorder transition $\alpha_2 \rightarrow \alpha$ in Ti-43.9Al-4Nb-1Mo-0.1B (at. %) and Ti-44Al-7Mo (at. %) alloys by *in-situ* neutron diffraction experiments during heating cycles [17, 18]. By Cu-K_α X-ray diffraction techniques, we can determine compositional differences and phase fractions as a function of depth in a sample, by selective sectioning, while neutron diffraction allows for the detection of order/disorder phase transitions. Hence, these two techniques can be used in a complementary fashion to extract valuable crystallographic information [20].

The uncertainty about the exact mechanisms of the pertaining phase transformation and the concomitant induced microstructure during the HPT process in γ-based Ti-Al alloys prompted this study. Quantum beam techniques [25] such as X-ray and neutron diffraction

were used to detect and quantify the crystallographic changes, thus clarifying the sequence of phase transformations and the pertaining micro-structural evolution as a function of the extent of deformation. In addition, scanning electron microscopy (SEM) and Electron Backscatter Diffraction (EBSD) revealed further information on the pertaining microstructural development and finally, the increase in hardness as a result of grain refinement was assessed by Vickers micro-hardness measurements.

7.2 Experimental details

The Ti-45Al-7.5Nb alloy used in this investigation was produced through a powder metallurgical route, introduced in section 3.1.2. The powders were prepared by gas atomization, and then hot isostatically pressed at 200 MPa at a temperature of 1553 K for 2 h [2]. An HPT facility [26, 27] (Figure 7.1a) was used to process the as-received alloys, more details of which is described in above section 3.1.3. The sample disk is placed onto the lower anvil and then moved upwards until the disk was contained within the depressions of the two anvil surfaces. Each anvil has a circular depression of 0.25 mm in depth and 10 mm in diameter thereby providing a quasi-constrained state during processing [6]. A compressive force of 480 kN is applied to impose a pressure of 6 GPa onto the sample. Disk samples are strained in torsion for 5 and 10 turns respectively and are identified as follows (see Table 1):

- 0-0: The as-received material;
- 6-0: Sample subjected to a pressure of 6 GPa without torsional deformation;
- 6-5 and 6-10: Samples subjected to 5 and 10 turns of torsional strain under a pressure of 6 GPa, respectively.

Table 7.1 Sample designation and processing parameters.

Sample	pressure [GPa]	torsion [turns]	Comments
0-0	0	0	as-received
6-0	6	0	pressurized
6-5	6	5	HPT processed
6-10	6	10	HPT processed

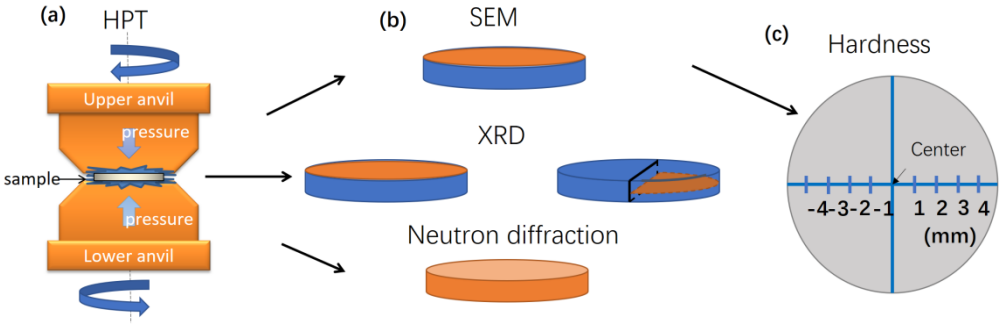

Figure 7.1 Experimental processing of the Ti-Al alloys.

(a) Schematic illustration of HPT processing of the Ti-Al alloy;

(b) Different slices were used for morphology and structure characterization using both XRD and neutron diffraction;

(c) Hardness measurements.

The morphology, phase and texture of HPT-processed samples were assessed as shown in Figure 7.1(b). The microstructure of the disk surface was examined using SEM (JEOL NeoScope JCM-7001). The possibility of phase transitions during HPT processing was studied by using Cu-K_α XRD with a wavelengths (λ_x) of 1.5418 Å and wave-vector (k_x) of 4.0752 $Å^{-1}$ at both the University of Wollongong, Australia and Hanyang University, Korea. The focusing sizes are 1 mm × 10 mm and 0.4 mm × 12 mm (longitudinal × transverse), respectively, both covering the disk diameter, thereby obtaing an average over the entire radial distribution.

X-ray diffraction (XRD) examinations were carried out both at the surface of the entire disk and the unveiled half mid-section (coloured in red in Figure 7.1(b)). Moreover, neutron diffraction was used to study the possible order/disorder transition during HPT processing in

the Ti-Al alloy. Neutron diffraction was conducted on the high intensity neutron diffractometer WOMBAT [21], introduced in above section 3.2.5.1. A Ge-311 monochromator selected an incident beam wavelength λ_n = 2.419 Å with corresponding wave number $k_n = 2.598\ \text{Å}^{-1}$. The specimen-integrated crystallographic preferred orientation (texture) was measured in four-circle set-up employing right-handed Busing-Levy convention [28] at the WOMBAT neutron diffractometer. The samples 6-5 and 6-10 were rotated in tilt angle χ [29-31] of the sample from 0° to 90° in steps of 15° and around the ϕ-axis [29-31] by 360° in 73 steps of 4.9315°. Such odd number of steps allows for the probing of additional pole figure coverage as the Friedel symmetry is bypassed. The diffraction rings recorded by a 2-dimensional, cylindrical detector were sectored into three sectors in the detector azimuth η [29-31] of 5.25° each. The changes in hardness of the Ti-Al alloy following high-pressure torsion were determined by micro-hardness measurements. These measurements were made along the diameter on a polished plane close to the surface of each disk at positions, 1 mm apart as illustrated in Figure 7.1(c), using a LECO M-400-H1 Vickers micro-hardness instrument with 100 g (0.98 N) loading and 12 seconds of indentation time.

7.3 Results and discussions

7.3.1 Microstructure

Back scattered SEM images of the as-received sample edges following HPT processing are depicted in Figure 7.2(a-d). In Figure 7.2(a), the dark gray areas represent the γ-phase while the bright regions show the α_2-phase. The structure consists of a duplex microstructure containing equiaxed γ-phase with an average size of ~10 μm and parallel platelets of the γ- and α_2 -phases (the lamellar structure), which presumably formed at the eutectoid temperature T_{eu} [32, 33]. The dark γ-phase and the bright α_2/α-phase still exist as a duplex structure

following HPT processing for 5 and 10 turns (Figure 7.2(b-d)). Bending of the lamellae occurred along the shear direction by torsional straining around the peripheries of the disks. Comparison of the lamellar spacing of the α_2-phase in the as-received condition (Figure 7.2(a)) with that of the deformed specimens (Figure 7.2(b-c)) provides convincing experimental evidence that HPT processing produces significant microstructural refinement. In some areas at the edge of sample 6-10, extreme grain refinement occurred, as shown in Figure 7.2(d), which is assumed to stem from originally large fully lamellar colony grain outliers and needs further investigation.

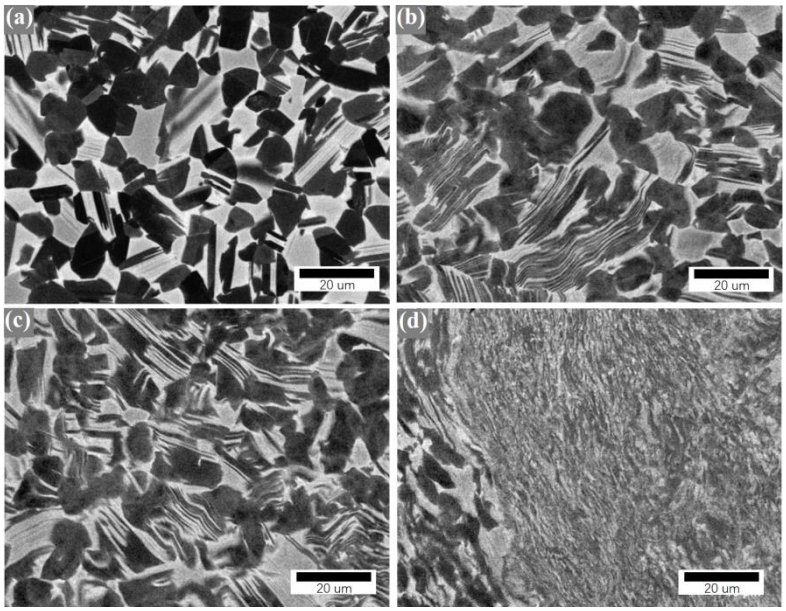

Figure 7.2 Microstructure of (a) the as-received sample; and near the disk edges of samples following HPT: (b) 6 GPa and 5 high-torsion turns; (c-d) 6 GPa and 10 high-torsion turns.

7.3.2 Phase transformations during HPT processing

The X-ray attenuation length is 8.36 μm at 45° incidence based on the assumption that the density is 3860 kg/m^3 and the weighted mass attenuation coefficient of the Ti-45Al-7.5Nb alloy is 10.95 m^2/kg (NIST database) [34]. Hence, X-ray diffraction can be used to average over a large specimen radius and characterize the average plastic strain within a thin layer

below the measurement surface. The X-ray diffractograms obtained at the surface and the median layers of the samples following different HPT processing steps are compared in Figure 7.3(a). In this figure, the diffraction profiles with darker colour refer to the surface plane and the brighter colour to the median disk surface at each HPT step. The peaks of each sample were indexed by the Crystallographic Information File (CIF, #1545053 and #1545054 for the γ- and α_2 –phases respectively) of the Crystallography Open Database [34] provided by Liss *et al.* [13]. The patterns of the as-received samples, which are denoted as 'no treatment' in Figure 7.3, consist of the peaks from the α_2/α- and γ-phases, thereby agreeing well with the SEM backscattering observations, as shown in Figure 7.2(a). Using the MAUD Rietveld analysis package [35], the phase fractions of the α_2/α- and γ-phases in the as-received samples at both the surface and the median layers were calculated as ~30 at. % and 70 at. %, respectively. Note our notation α_2/α for an ensemble of the ordered α_2 and disordered α phase, since X-rays cannot make a clear distinction between the two.

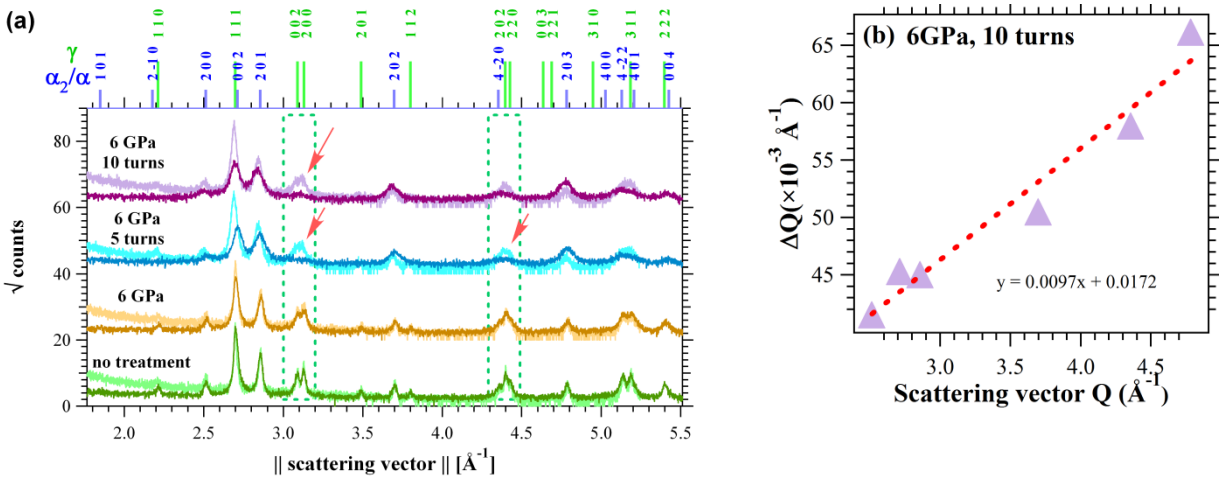

Figure 7.3 (a) The XRD patterns of the samples before and after different HPT processes. The XRD patterns at surface and median layers of the disks were denoted as dark and light lines, respectively. (b) Williamson-Hall analysis for α/α_2 at median layers of sample 6-10. The dashed line was fitted to data of each sample using equation (1).

Salient features of the patterns obtained as a function of processing, are peak broadening and the evolution of the peak intensities. Increasing torsional deformation caused broadening of

the X-ray diffraction peaks shown in Figure 7.3(a), indicating that the grains are being refined by deformation processing. By adopting an *isotropic* model where peak broadening is simplified, as being independent of the different *hkl* directions [36, 37], the shape of the peak is described as a function of *size and strain* in MAUD [35]. The diffraction coherent crystallite size of the α_2/α-phase were 124, 92, 72 and 29 nm for samples 0-0, 6-0, 6-5 and 6-10, respectively, thereby providing convincing evidence that high-pressure torsion progressively reduces the crystallite size.

Following HPT processing, the grains are so small that it is impossible to measure the exact grain sizes from the SEM pictures shown in Figure 7.2. In order to obtain a better estimate of the crystallite size, the Williamson-Hall method was employed to verify the crystallite size and micro-strain in the median section of sample 6-10. The Williamson-Hall method assumes that a combination of size and strain contributes to the total breadth of a Bragg peak [38, 39]. In this model, strain-induced peak broadening is assumed to result from crystal imperfections and distortion, expressed as $\varepsilon = \Delta Q/Q$. It is assumed that the grain size spreads homogeneously in reciprocal space by $\Delta Q = K \cdot 2\pi/\mathrm{D}$, where K is a shape factor equal to 0.94 [40]. Then, the full width at half-maxium (ΔQ) is:

$$\Delta Q = (2\pi/\mathrm{D}) \cdot K + \varepsilon Q \quad (1)$$

Using equation (1), the fitted ΔQ as a function of reciprocal space coordinate Q is depicted in Figure 7.3(b). Using the intercept of 0.0172 $Å^{-1}$, the X-ray coherent crystallite size of the α_2/α-phase is estimated as 34 nm. Moreover, the slope provides evidence of the existence of a highly stressed microstructure with an elastic strain of 0.0097. Such strain broadening is an overall average over the sampled volume, which can result from inter-granular stresses,

interacting on the scale of the grain size as a local property, and from integration over a residual stress field, which would vary and hence, shift the peaks as a function of location.

By using a nano-indentation technique, Han *et al*. determined the Young's modulus of this material as 145 GPa and the yield strength as 2.35 GPa following 10 turns by HPT [12]. With this modulus and a measured strain of 0.0097, a residual stress of 1.41 GPa is estimated. This value represents 61 % of the reported yield point of this alloy and hence, a small external stress of only ~0.94 GPa is required to overcome the yield stress. Moreover, since the specimens are inhomogeneous, stress concentrations can be much higher and easily lead to crack formation and in the extreme, to mechanical failure.

By single peak fitting with a *Guassian* function at the surface-near layer, it transpires that the peak area of α/α_2-phase increases with processing, e.g. the α_2/α-202 peak area varies from 0.933 [counts $Å^{-1}$] in sample 6-0 to 2.676 [counts $Å^{-1}$] in sample 6-10. Similar trends are observed on the other main α_2/α peaks while the intensities of γ peaks largely shrink, providing convincing evidence that deformation by HPT increases the fraction of the α_2/α-phase at the expense of γ. Such behavior strongly underlines the notion that the disordered γ-phase transformation is driven by the high ordering energy of close-packed Ti-Al configurations [13,14].

It is important to note that the stress and strain distributions in the processed disks are far from being uniform, neither in the radial direction, expected by the principles of HPT [41], nor in the through-thickness direction as shown by the different hardness value [42]. For this reason, X-ray diffraction profiles taken at the macroscopic surface and the median section of the sample disks are expected to be different. Specifically, the present results indicate that the HPT-induced torsional plastic strain is higher at the sample surface than at the median section.

Consequently, phase constituents would be different at the sample surface and at the median section as shown by a comparison between the purple and blue curves for the 6-5 and 6-10 samples as indicated by red arrows in Figure 7.3(a). The diffraction peaks of the γ-phase measured at the sample surface show progressively reduced intensity following torsion for 5 HPT turns and they eventually disappear with an increasing number of turns. Conversely the γ-phase peaks obtained from the mid-sections of the samples (lines with lighter colour in Figure 7.3(a)) are still present and largely broadened. The important conclusion from these observations is that the difference in the extent of severe plastic deformation from the centre to the perimeter of a disk in this torsional experiment also influences the extent of the $\gamma \rightarrow \alpha$ phase transition. It is therefore not surprising that some researchers observed this phase transition [7] and others did not [9]. It evidently depends on where in (or on) the specimen the phase fraction is determined.

Earlier research on two-phase materials, duplex stainless steel [43-47] and a Cu-Ag alloy [48] demonstrated that the HPT disks reveal unusual flow patterns involving double swirls and local vortices. The presence of swirls and vortices produced by HPT was explained by modelling the development of instabilities as a result of non-symmetrical shear and compressive stresses, especially when inevitable anvil misalignments increase [49]. These studies were conducted on the arbitrary-sectioned planes parallel to the HPT disk surfaces, but Kulagin *et al.* [50] have recently shown that shear is surface-parallel near the surface only. They have shown that turbulent flow may occur in the bulk volume, resulting in rolling of vortices with localized areas of higher and reduced shear, as schematically shown Figure 7.4. Hence, severe plastic deformation occurs at or near the surface layers contacting the anvils, while inhomogeneous straining deep in the bulk (or disk thickness) eventually rolls off in a

vortex-like manner. The result is that less transformed material is located next to highly deformed material in shear zones, leading to the observed differences between the diffractograms obtained from the near-surface region and the central layer respectively. These differences are attributed to the presence of two co-existing phases, which respond differently to torque in the shear-field of the matrix. The core of the vortices would experience less torsional shear [49] thus plastic deformation by HPT, while the interaction zone between neighbouring vortices suffers from enhanced severe plastic deformation. Therefore, the surface layer exhibits overall and homogeneously severe plastic deformation, while the bulk can contain highly as well as less severely plastically deformed regions. These observations in addition to taking into account the X-ray diffractograms, lead to the conclusion that the γ-phase is highly suppressed by severe plastic deformation. Considering that the γ-phase has the highest ordering energy of all Ti-Al intermetallic configurations [51]**,** it would rather transform into the α_2/α-phase upon the severe plastic deformation. Such transformation between the *fcc*- and the *hcp*- based phases occurs primarily displacively by changing the stacking sequence from ABCABC to ABABAB while no long-range diffusion occurs at the given temperature. Because the stoichiometry of the γ-phase (TiAl) is different from α_2 (Ti_3Al), the latter is supposed to be highly disordered. Similar disorder-driven $\gamma \rightarrow \alpha$ transformation has been observed upon the application of hydrostatic pressure even though the transformation-induced volume per atom increases and counterbalances the pressure-induced volume decrease [13].

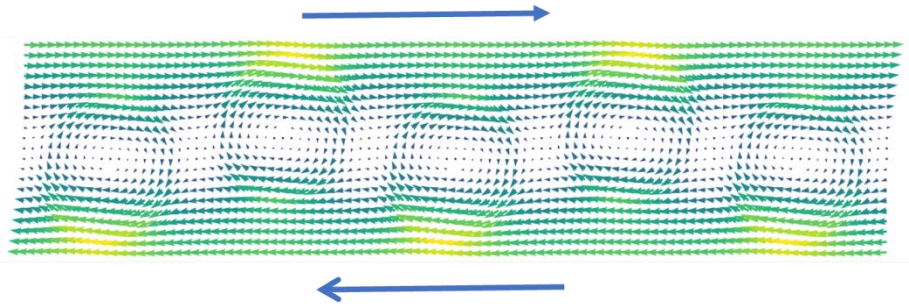

Figure 7.4 Sketch of turbulent flow: Simple applied shear at the confined surfaces leads to a pure shear deformation thereunder while vortices can form, rolling in the bulk and separating shear zones (bands) from less deformed material, supported by evidence of Kulagin *et.al* [50].

Whereas X-rays have an attenuation length of only 10 µm, neutrons can penetrate much deeper and as a result, make it possible to obtain bulk information integrated over the entire specimen. It is peculiar that in the composition of the alloy under investigation, the disordered phases are close to a neutron scattering null matrix [19, 52]. Thus, only peaks from the ordered α_2- and γ-phases can be detected during neutron scattering experiments. The height of the superstructure peaks depends not only on the phase fraction, but also on the order parameter of each phase. Figure 7.5(a) compares the neutron diffractograms of different samples before and after HPT processing. It shows that the diffraction peaks of both the α_2-phase and the γ-phase broaden with increasing applied deformation strain by compression and concurrent torsion. Consistent with the X-ray evidence, the broadening of the neutron diffraction peaks indicates that the grains have been refined as a result of the high applied plastic strains.

The γ-001 diffraction peak, representing intermetallic order, is prominent and has a high intensity in the neutron diffraction pattern as indicated by a light green-dot box in Figure 7.5(a), but it is almost non-existent in the X-ray diffractograms, which are shown in Figure 7.3. By contrast, the γ-111 peak as well as the g-002/200 peaks have strong intensity in X-ray

diffraction, Figure 7.3, whereas they are almost invisible to neutrons, as indicated by the green dotted box in Figure 7.5. This observation is fundamentally important because it allows a distinction to be made between ordered and disordered crystals structures through neutron diffraction experiments.

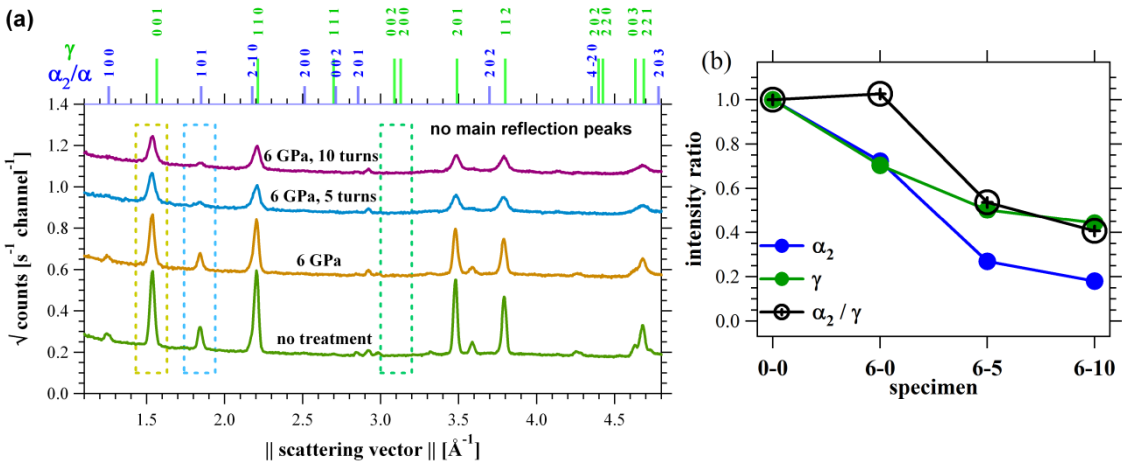

Figure 7.5 (a) Neutron diffractograms of samples 0-0b, 6-0b, 6-5b and 6-10b using the WOMBAT instrument. Neutron diffraction intensity ratios of the γ-001 and the α_2 -101 superstructure reflections normalized to the starting condition 0-0, and (b) their ratios.

Specifically, an estimate of the total phase fractions can be made by X-ray diffraction analysis, while the extent to which a phase is ordered can be determined through the integrated neutron intensities (the area underneath a specific peak, for example the γ-001 peak). By single peak fitting using the Igor Pro 4 software, the relative areas underneath the γ-001 peak of samples 0-0, 6-0, 6-5, 6-10 were calculated as 0.013359, 0.009407, 0.006720 and 0.005923, respectively. The clear implication of this finding is that the fraction of the ordered γ-phase decreases with increasing applied strain through HPT processing. The relative areas underneath the α_2-101 peaks of samples 0-0, 6-0, 6-5 and 6-10 as indicated by the blue box in Figure 7.5(a) were 0.003534, 0.002497, 0.000932 and 0.0006232, hence showing the same trend. Neutron diffraction intensity ratios of the γ-001 and the α_2-101

superstructure reflections were normalized with reference to the starting condition 0-0, and these ratios are shown in Figure 7.5(b). This peak area analysis shows that the fraction of the ordered α_2-phase decreases sharply following HPT processing. By comparison, the X-ray analysis indicated that the application of severe plastic deformation that led to an increase in the fraction of the α/α_2-phase. Therefore, comparison between the neutron and X-ray diffraction data leads to the conclusion that the ordered α_2-phase transforms into the disordered α-phase upon the application of severe plastic deformation through HPT. This finding has important implications in the manufacturing of Ti-Al alloys since the disordered phase exhibits better ductility than the ordered phase.

The X-ray diffraction patterns shown in Figure 7.3 demonstrate that the γ-phase disappears and only the α/α_2-phase is present on the surface of samples 6-5 and 6-10., where measurements were made at the local volume or limited layers parallel to the surface planes. On the other hand, the neutron diffractograms shown in Figure 7.5(a) indicate that the bulk samples of 6-5 and 6-10 contain almost no ordered α_2-phase. Therefore, the sequence of phase transformations on the surface of the samples following HPT is $(\alpha_2 + \gamma) \rightarrow (\alpha + \gamma) \rightarrow \alpha$. Conversely, the existence of both α/α_2-phase and γ-phase X-ray peaks at the half mid-section of samples 6-5 and 6-10 (weaker lines in Figure 7.3) indicate that this phase transition is not fully completed at the median layer of the disk-shaped sample. Therefore, the extent to which phase transformations occur within HPT samples depends on the exact position within the sample.

7.3.3 Texture

In addition to the important aspects of microstructural development and phase evolution resulting from severe plastic deformation, it is of the essence to determine the effect of such

processing on crystal orientation. To this end, a four-circle neutron diffraction set-up was used to assess texture development integrated over the bulk. Figure 7.6 shows the pole figures for the {001}- and {110}-lattice planes of the γ-phase for samples 6-5 (a,b) and 6-10 (c,d) respectively. Also shown is a schematic diagram of the preferred γ-crystal orientations (e). In both the torsionally-strained samples, a pronounced γ-110 type fiber texture is observed: most of the {110} plane normals align along the cylinder axis of the sample while the {001} lattice plane normals are predominantly perpendicular to the cylindrical axis of the disk, as illustrated in Figure 7.6(e). This axial symmetry is the result of the axial-symmetry by compression straining and radial symmetry by torsional straining during HPT processing, when averaged over the entire specimen.

Bartels *et al.* [20, 53] found a strongly modified cube texture in a γ-titanium aluminide in a rolling experiment, meaning that the crystallographic *c*-axis of the γ-phase is aligned with the transverse direction, which is perpendicular to both the shear and compression directions in a rolling process. In the case of torsional deformation, such as the case in the present investigation, any disk element at some radius from the center experiences well-defined shear and compressive straining, the transverse direction pointing radial, coinciding with the observed *c*-axis distribution (strictly speaking, the c^* plane normal). Therefore, it is expected that a local rolling texture would be present if the position was resolved enough; however, sample averaging delivers the axial symmetry.

Compared to Figures 7.6(a) and Figure 7.6(c), the intensity is equalised at the periphery of the pole figures, meaning that greater symmetry in the crystallographic orientations is achieved by 5 turns by HPT processing. It is also worth noting that the maximum texture intensity is relatively low and decreases even further with an increase in torsional

deformation to 10 turns. Deformation by crystallographic slip would result in strong texture maxima. However, texture is fairly weak in the present case, indicating that the main deformation mechanism changes from slip to grain boundary sliding as the grains are refined

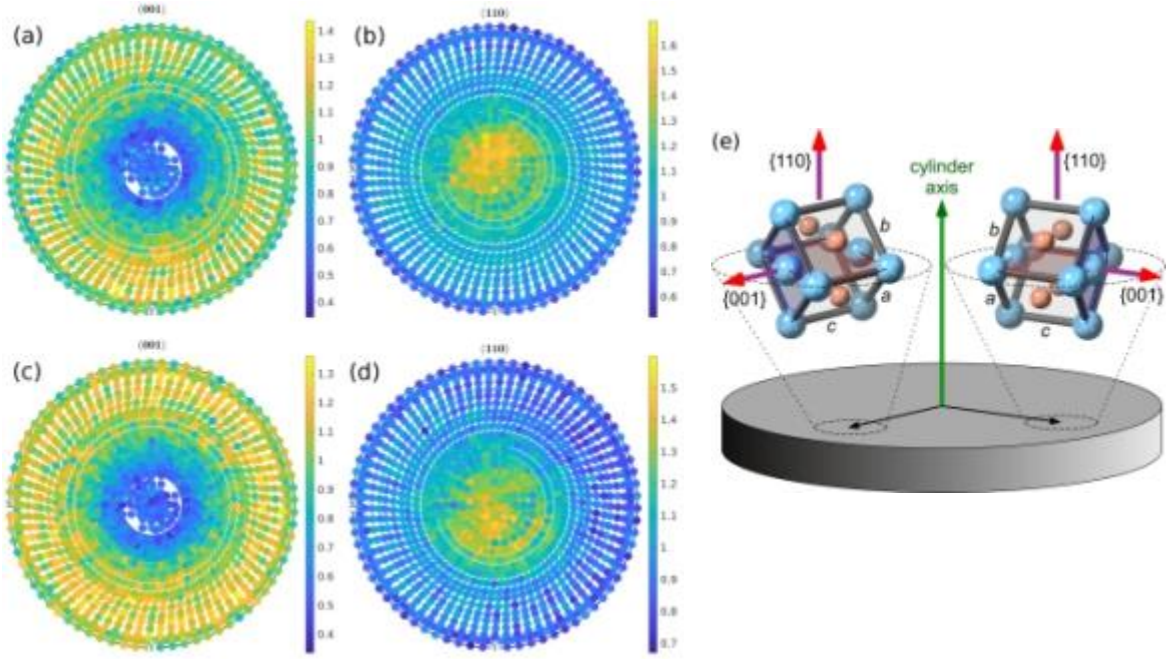

Figure 7.6 Experimentally determined bulk-integrated exture of the γ-phase in the Ti-45Al-7.5Nb alloy after HPT process: 001-pole figure of sample 6-5 (a) and 6-10 (c); 110-pole figure of sample 6-5 (b) and 6-10 (d); and the preferred orientation of γ-phase using sample coordinate (e).

to the nanometer scale [54]**.** The important implication of this observation is that the weak texture is consistent with orientation randomization by the rolling of grains and vortices in a turbulent bulk flow as argued above in the section on X-ray diffraction. Thus, as opposed to deformation by dislocation slip, where grain rotation is terminated upon reaching a stable orientation with a zero Schmidt factor, particle rolling and grain boundary sliding continuously re-orient grains, thereby randomizing their orientations. These conclusions reached by consideration of the present texture analysis, are in excellent agreement with the conclusions reached in an earlier micro-mechanical study using a nano-indentation. In that study, the role of grain boundary sliding as a deformation mechanism was assessed by

observing the increased strain rate sensitivity in a γ-based titanium aluminide following HPT processing [13]. Moreover, a recent review summarizing the available data on ultrafine-grained materials processed by severe plastic deformation, pointed to a consistent trend of increasing strain rate sensitivity by reducing the grain size [55].

7.3.4 Microhardness measurement

Figure 7.7 shows the experimentally determined micro-hardness values of samples 0-0, 6-0, 6-5 and 6-10. The shear strain applied is given by equation (2) below [56, 57].

$$\gamma = \frac{2\pi N \cdot r}{h} \tag{2}$$

N is the number of torsion turns, r is the radius of the disk and h is the disk thickness. Equation (2) shows that the shear strain is a maximum at the edge of the disk and is zero at the centre where $r = 0$.

The hardness variations demonstrate an increase from 308 H_v to 337 H_v following the application of a compression force of 6 GPa without torsion straining. Because the compression induced phase change from γ to α_2/α [13] occurs displacively, stacking faults and ultrafine lamella hinder dislocation movement and thus increase the hardness. Furthermore, the slight increase in hardness at the disk center of the disk and periphery is often observed at the compressive stage in the HPT procedure due to metal flow in a quasi-constrained manner [58]. Consistent with the trend in strain as shown in equation (2), the measured hardness increases from the center to the edge as a result of HPT processing (samples 6-5 and 6-10 in Figure 7.7). The hardness increases to 337 H_v following the application of a compression force of 6 GPa without the application of torsion. This increase in hardness is attributed to displacive phase changes upon pressure loading, suggesting a high

density of planar faults resulting in ultrafine lamellae on a nanometer scale. Specifically after 5 turns and 10 turns of torsion under a pressure of 6 GPa, the hardness increases to 480 and 510 H_v at the centre and to 604 H_v at the edges of the disks, respectively. The maximum hardness at the outer edge of the disk, achieved by intensive grain refinement after 5 turns is twice as high as in the annealed condition.

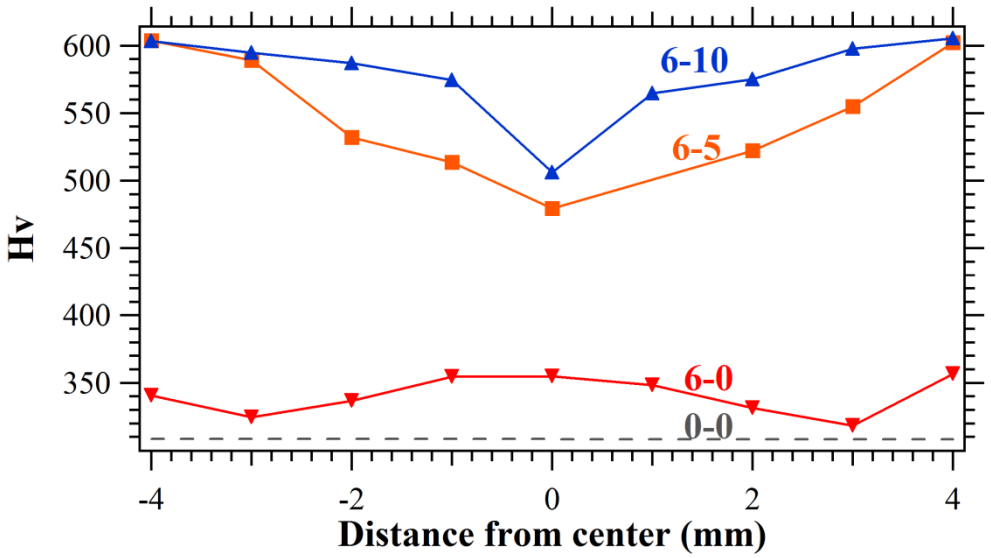

Figure 7.7 Vickers micro-hardness with distance from the centre of the disks after processing by HPT under 0, 5 and 10 revolutions of torsion at 6GPa.

The present hardness measurements taken close to the disk surface indicates that the hardness increase occurred in the absence of microstructural recovery [59]. An earlier review of hardness evolution models has shown that this particular hardness behaviour is typical of materials processed at homologous temperatures below ~0.3 by HPT processing [42], which is the case in the present study for the γ-based titanium aluminide. Conversely, earlier hardness measurements have shown that the saturated hardness is reached throughout the disk diameter even after 5 turns by HPT processing when testing at the mid-height of the disk [12]. This difference in the hardness behaviour at different measuring planes in the through-

thickness direction was first observed in magnesium alloys [60-63] while it was not observed in pure aluminium due to the fast microstructural recovery during processing [60, 63]. The heterogeneous distribution of hardness was observed in the through-thickness direction of steel [46, 64-66], commercial purity copper [67], pure silver [68], and titanium alloy [69] disks following HPT processing. Moreover, a recent experiment clearly demonstrated the presence of a heterogeneous grain size distribution in a HPT-processed interstitial-free steel in the through-thickness direction, which led to a gradient in the microstructure [70]. These observed hardness heterogeneities have been attributed to flow localization and strain gradation: the former depends on the nature of the strain hardening of the material and the latter is due to the lateral friction between the sample and the anvil depression walls [71, 72]. The present study demonstrates, for the first time, that heterogeneity exists not only in microstructure and mechanical properties, but also in order/disorder transformations and phase transformations within a bulk sample subjected to severe plastic deformation applied by high-pressure torsion.

7.4 Summary and conclusions

This thesis combined advanced X-ray and neutron diffraction methods with complementary microstructural analysis and hardness measurements for a comprehensive study of Ti-45Al-7.5Nb intermetallics, correlating crystallographic transformations with mechanical properties and microstructure.

The application of severe plastic deformation to a Ti-45Al-7.5Nb alloy in the form of high-pressure torsion results in the modification of a number of important microstructural features and hardness.

- The coherent crystallite size of the α_2/α-phase is refined to 34 nm as the result of the application of high compressive pressure (6 GPa) and torsion (10 turns).
- The effect of severe plastic deformation at the near-surface region is much more pronounced than in the median layer, indicating heterogeneity and shear zones with higher plastic strain at the surface.
- The sequence of phase transformations at the surface is: $(\alpha_2 + \gamma) \rightarrow (\alpha + \gamma) \rightarrow \alpha$.
- This sequence of events is not fully realized at the median layer of the thin disk.
- An order-disorder phase transition occurs during high-pressure torsional deformation.
- Following high-pressure torsion processing, a {110} type of fibre texture is formed in the γ-phase, integrated over the bulk.
- The hardness is enhanced, increasing from 308 H_v to a maximum of 605 H_v.
- High residual stresses remain in the room-temperature processed material with values close to the yield strength limit, making the processed specimen susceptible to brittle failure.

The combination of X-ray analysis and neutron diffraction techniques in the present investigation paves the way for the extension of the present study of Ti-Al intermetallics to other alloy systems where order/disorder phase transitions occur.

7.5 References

[1] H. Chladil, H. Clemens, H. Leitner, A. Bartels, R. Gerling, F.-P. Schimansky, S. Kremmer, Phase transformations in high niobium and carbon containing γ-TiAl based alloys, Intermetallics, vol.14, pp. 1194-1198, 2016.

[2] H.F. Chladil, H. Clemens, G.A. Zickler, M. Takeyama, E. Kozeschnik, A. Bartels, T. Buslaps, R. Gerling, S. Kremmer, L. Yeoh, Experimental studies and thermodynamic

simulation of phase transformations in high Nb containing γ-TiAl based alloys, International Journal of Materials Research, vol. 98, pp. 1131-1137, 2007.

[3] F. Appel, M. Oehring, J. Paul, A novel in situ composite structure in TiAl alloys, Materials Science and Engineering: A, vol.493, pp. 232-236, 2008.

[4] F. Froes, C. Suryanarayana, G.-H. Chen, A. Frefer, G.R. Hyde, Nanostructure processing for titanium-based materials, JOM Journal of the Minerals, Metals and Materials Society, vol. 44, pp. 26-29, 1992.

[5] R.Z. Valiev, T.G. Langdon, Principles of equal-channel angular pressing as a processing tool for grain refinement, Progress in Materials Science, vol. 51, 881-981, 2006.

[6] R.B. Figueiredo, P.R. Cetlin, T.G. Langdon, Using finite element modeling to examine the flow processes in quasi-constrained high-pressure torsion, Materials Science and Engineering: A, vol. 528, pp. 8198-8204, 2011.

[7] A. Korznikov, O. Dimitrov, G. Korznikova, J. Dallas, A. Quivy, R. Valiev, A. Mukherjee, Nanocrystalline structure and phase transformation of the intermetallic compound TiAl processed by severe plastic deformation, Nanostructured materials, vol. 11, pp. 17-23, 1999.

[8] N. Kazantseva, N. Mushnikov, A. Popov, P. Terent'ev, V. Pilyugin, Severe plastic deformation and hydrogenation of the titanium aluminides, Journal of Alloys and Compounds, vol. 509, pp. 9307-9311, 2011.

[9] B. Srinivasarao, A. Zhilyaev, R. Muñoz-Moreno, M. Pérez-Prado, Effect of high pressure torsion on the microstructure evolution of a gamma Ti–45Al–2Nb–2Mn–0.8 vol% TiB2 alloy, Journal of Materials Science, vol. 48, pp. 4599-4605, 2013.

[10] N. Hansen, Hall–Petch relation and boundary strengthening, Scr. Mater., vol. 51, pp. 801-806, 2004.

[11] K. Edalati, S. Toh, H. Iwaoka, M. Watanabe, Z. Horita, D. Kashioka, K. Kishida, H. Inui, Ultrahigh strength and high plasticity in TiAl intermetallics with bimodal grain structure and nanotwins, Scr. Mater., vol. 67, pp. 814-817, 2012.

[12] J.-K. Han, X. Li, R. Dippenaar, K.-D. Liss, M. Kawasaki, Microscopic plastic response in a bulk nano-structured TiAl intermetallic compound processed by high-pressure torsion, Materials Science and Engineering: A, vol. 714, pp. 84-92, 2018.

[13] K.-D. Liss, K.-I. Funakoshi, R. Dippenaar, Y. Higo, A. Shiro, M. Reid, H. Suzuki, T. Shobu, K. Akita, Hydrostatic Compression Behavior and High-Pressure Stabilized β-Phase in γ-Based Titanium Aluminide Intermetallics, Metals, vol. 6, pp. 165, 2016.

[14] M. Asta, D. de Fontaine, M. Van Schilfgaarde, First-principles study of phase stability of Ti–Al intermetallic compounds, Journal of materials research, vol. 8, pp. 2554-2568, 1993.

[15] O. Bouaziz, Y. Brechet, J.D. Embury, Heterogeneous and architectured materials: a possible strategy for design of structural materials, Advanced Engineering Materials, vol. 10, pp. 24-36, 2008.

[16] H.-J. Lee, S.K. Lee, K.H. Jung, G.A. Lee, B. Ahn, M. Kawasaki, T.G. Langdon, Evolution in hardness and texture of a ZK60A magnesium alloy processed by high-pressure torsion, Materials Science and Engineering: A, vol. 630 pp. 90-98, 2015.

[17] I.J. Watson, K.D. Liss, H. Clemens, W. Wallgram, T. Schmoelzer, T.C. Hansen, M. Reid, In Situ Characterization of a Nb and Mo Containing γ - TiAl Based Alloy Using Neutron Diffraction and High - Temperature Microscopy, Advanced engineering materials, vol.11, pp. 932-937, 2009.

[18] S. Kabra, K. Yan, S. Mayer, T. Schmoelzer, M. Reid, R. Dippenaar, H. Clemens, K.-D. Liss, Phase transition and ordering behavior of ternary Ti–Al–Mo alloys using in-situ neutron diffraction, International Journal of Materials Research, vol. 102, pp. 697-702, 2011.

[19] K.-D. Liss, Metals Challenged by Neutron and Synchrotron Radiation, Metals, vol. 7, pp. 266, 2017.

[20] K.-D. Liss, A. Bartels, A. Schreyer, H. Clemens, High-energy X-rays: a tool for advanced bulk investigations in materials science and physics, Textures and Microstructures, vol. 35, pp. 219-252, 2003.

[21] G.E. Bacon, K. Lonsdale, Neutron diffraction, Reports on Progress in Physics, vol. 16, pp. 1, 1953.

[22] W. Reimers, A.R. Kaysser-Pyzalla, A. Schreyer, H. Clemens, Neutrons and synchrotron radiation in engineering materials science: from fundamentals to material and component characterization, John Wiley & Sons, 2008.

[23] X – ray and Neutron Diffraction of TiAl Alloys, 2015.

[24] T. Schmoelzer, K.-D. Liss, G.A. Zickler, I.J. Watson, L.M. Droessler, W. Wallgram, T. Buslaps, A. Studer, H. Clemens, Phase fractions, transition and ordering temperatures in TiAl–Nb–Mo alloys: An in-and ex-situ study, Intermetallics, vol. 18, pp. 1544-1552, 2010.

[25] K.-D. Liss, Quantum Beam Science—Applications to Probe or Influence Matter and Materials, Quantum Beam Science, vol. 1, pp. 1, 2017.

[26] M. Kawasaki, J.-I. Jang, Micro-Mechanical Response of an Al-Mg Hybrid System Synthesized by High-Pressure Torsion, Materials, vol. 10, pp. 596, 2017.

[27] A. Vorhauer and R. Pippan, "On the homogeneity of deformation by high pressure torsion," Scripta Materialia, vol. 51, pp. 921-925, 2004.

[28] W.R. Busing, H.A. Levy, Angle calculations for 3-and 4-circle X-ray and neutron diffractometers, Acta Crystallographica, vol. 22, pp. 457-464, 1967.

[29] D. Chateigner, Combined Analysis, 2010.

[30] J. Grasslin, L.B. McCusker, C. Baerlocher, F. Gozzo, B. Schmitt, L. Lutterotti, Advances in exploiting preferred orientation in the structure analysis of polycrystalline materials, Journal of Applied Crystallography, vol. 46, pp. 173-180, 2012.

[31] H.-R. Wenk, Neutron diffraction texture analysis, Reviews in mineralogy and geochemistry, vol. 63, pp. 399-426, 2006.

[32] F. Appel, R. Wagner, Microstructure and deformation of two-phase γ-titanium aluminides, Materials Science and Engineering: R: Reports, vol. 22, pp. 187-268, 1998.

[33] R. Ramanujan, Phase transformations in γ based titanium aluminides, International Materials Reviews, vol. 45, pp. 217-240, 2000.

[34] S. Gražulis, A. Daškevič, A. Merkys, D. Chateigner, L. Lutterotti, M. Quirós, N.R. Serebryanaya, P. Moeck, R.T. Downs, A. Le Bail, Crystallography Open Database (COD): an open-access collection of crystal structures and platform for world-wide collaboration, Nucleic Acids Research, vol. 40, pp. 420-427, 2012

[35] L. Lutterotti, S. Matthies, H. Wenk, MAUD (Material Analysis Using Diffraction): a user friendly Java program for Rietveld texture analysis and more, Proceeding of the twelfth international conference on textures of materials (ICOTOM-12), NRC Research Press Ottowa, Canada, pp. 1599. 1999

[36] I. Lonardelli, Deformation mechanisms in bulk nanostructured aluminum obtained after cryomilling and consolidation by spark plasma sintering, University of Trento, 2010.

[37] D. Balzar, N. Audebrand, M. Daymond, A. Fitch, A. Hewat, J. Langford, A. Le Bail, D. Louër, O. Masson, C. McCowan, Size-strain line-broadening analysis of the ceria round-robin sample, Journal of Applied Crystallography, vol. 37, pp. 911-924, 2004

[38] G. Williamson, W. Hall, X-ray line broadening from filed aluminium and wolfram, Acta metallurgica, vol. 1, pp. 22-31, 1953.

[39] E.J. Mittemeijer, U. Welzel, The "state of the art" of the diffraction analysis of crystallite size and lattice strain, Zeitschrift für Kristallographie International journal for structural, physical, and chemical aspects of crystalline materials, vol. 223, pp. 552-560, 2008.

[40] A. Patterson, The Scherrer formula for X-ray particle size determination, Physical review, vol. 56, pp. 978, 1939.

[41] A.P. Zhilyaev, T.G. Langdon, Using high-pressure torsion for metal processing: Fundamentals and applications, Progress in Materials Science, vol. 53, pp. 893-979, 2008.

[42] M. Kawasaki, Different models of hardness evolution in ultrafine-grained materials processed by high-pressure torsion, Journal of Materials Science, vol. 49, pp. 18-34, 2014.

[43] Y. Cao, M. Kawasaki, Y. Wang, S. Alhajeri, X. Liao, W. Zheng, S. Ringer, Y. Zhu, T. Langdon, Unusual macroscopic shearing patterns observed in metals processed by high-pressure torsion, Journal of materials science, vol. 45, pp. 4545-4553, 2010.

[44] Y. Cao, Y. Wang, R. Figueiredo, L. Chang, X. Liao, M. Kawasaki, W. Zheng, S. Ringer, T. Langdon, Y. Zhu, Three-dimensional shear-strain patterns induced by high-pressure torsion and their impact on hardness evolution, Acta Materialia, vol. 59, pp. 3903-3914. 2011.

[45] Y. Cao, Y. Wang, S. Alhajeri, X. Liao, W. Zheng, S. Ringer, T. Langdon, Y. Zhu, A visualization of shear strain in processing by high-pressure torsion, Journal of materials science, vol. 45, pp. 765, 2010

[46] Y. Huang, M. Kawasaki, T.G. Langdon, An investigation of flow patterns and hardness distributions using different anvil alignments in high-pressure torsion, Journal of Materials Science, vol. 48, pp. 4533-4542, 2013.

[47] Y. Huang, M. Kawasaki, T.G. Langdon, Influence of Anvil Alignment on Shearing Patterns in High‐Pressure Torsion, Advanced Engineering Materials, vol. 15, pp. 747-755, 2013.

[48] Y. Tian, X. An, S. Wu, Z. Zhang, R.B. Figueiredo, N. Gao, T. Langdon, Direct observations of microstructural evolution in a two-phase Cu–Ag alloy processed by high-pressure torsion, Scr. Mater., vol. 63, pp. 65-68, 2010.

[49] Y. Huang, M. Kawasaki, T.G. Langdon, An evaluation of the shearing patterns introduced by different anvil alignments in high-pressure torsion, Journal of materials science, vol. 49, pp. 3146-3157, 2014.

[50] R. Kulagin, Y. Beygelzimer, Y. Ivanisenko, A. Mazilkin, H. Hahn, High Pressure Torsion: from Laminar Flow to Turbulence, IOP Conference Series: Materials Science and Engineering, IOP Publishing, pp. 012045. 2017

[51] J. Zou, C.L. Fu, M.H. Yoo, Phase stability of intermetallics in the Al‐Ti system: A first-principles total-energy investigation, Intermetallics, vol. 3, pp. 265-269, 1995.

[52] T. Okuchi, A. Hoshikawa, T. Ishigaki, Forge-Hardened TiZr Null-Matrix Alloy for Neutron Scattering under Extreme Conditions, Metals, vol. 5, pp. 2340-2350, 2015.

[53] A. Bartels, H. Kestler, H. Clemens, Deformation behavior of differently processed γ-titanium aluminides, Materials Science and Engineering: A, vol. 329, pp.153-162, 2002.

[54] M. Pérez-Prado, G. González-Doncel, O. Ruano, T. McNelley, Texture analysis of the transition from slip to grain boundary sliding in a discontinuously recrystallized superplastic aluminum alloy, Acta materialia, vol. 49, pp. 2259-2268, 2001.

[55] M. Kawasaki, B. Ahn, P. Kumar, J.i. Jang, T.G. Langdon, Nano‐and Micro‐Mechanical Properties of Ultrafine‐Grained Materials Processed by Severe Plastic Deformation Techniques, Advanced Engineering Materials, vol. 19, 2017.

[56] R. Valiev, Y.V. Ivanisenko, E. Rauch, B. Baudelet, Structure and deformaton behaviour of Armco iron subjected to severe plastic deformation, Acta Materialia, vol. 44, pp. 4705-4712, 1996.

[57] F. Wetscher, A. Vorhauer, R. Stock, R. Pippan, Structural refinement of low alloyed steels during severe plastic deformation, Materials Science and Engineering: A, vol. 387, pp. 809-816, 2004.

[58] Y. Song, E.Y. Yoon, D.J. Lee, J.H. Lee, H.S. Kim, Mechanical properties of copper after compression stage of high-pressure torsion, Materials Science and Engineering: A, vol. 528, pp. 4840-4844, 2011.

[59] M. Kawasaki, B. Ahn, T.G. Langdon, Significance of strain reversals in a two-phase alloy processed by high-pressure torsion, Materials Science and Engineering: A, vol. 527, pp. 7008-7016, 2010.

[60] M. Kawasaki, R.B. Figueiredo, T.G. Langdon, An investigation of hardness homogeneity throughout disks processed by high-pressure torsion, Acta Materialia, vol. 59, pp. 308-316, 2011.

[61] R.B. Figueiredo, M.T.P. Aguilar, P.R. Cetlin, T.G. Langdon, Deformation heterogeneity on the cross-sectional planes of a magnesium alloy processed by high-pressure torsion, Metallurgical and Materials Transactions A, vol. 42, pp. 3013-3021, 2011.

[62] R.B. Figueiredo, T.G. Langdon, Development of structural heterogeneities in a magnesium alloy processed by high-pressure torsion, Materials Science and Engineering: A, vol. 528, pp. 4500-4506, 2011.

[63] M. Kawasaki, R.B. Figueiredo, T.G. Langdon, Twenty-five years of severe plastic deformation: recent developments in evaluating the degree of homogeneity through the thickness of disks processed by high-pressure torsion, Journal of Materials Science, vol. 47, pp. 7719-7725, 2012.

[64] A. Hohenwarter, A. Bachmaier, B. Gludovatz, S. Scheriau, R. Pippan, Technical parameters affecting grain refinement by high pressure torsion, International Journal of Materials Research, vol. 100, pp. 1653-1661, 2009.

[65] Y. Song, W. Wang, D. Gao, E.Y. Yoon, D.J. Lee, C.S. Lee, H.S. Kim, Hardness and microstructure of interstitial free steels in the early stage of high-pressure torsion, Journal of materials science, vol. 48, pp. 4698-4704, 2013.

[66] M.S. Matoso, R.B. Figueiredo, M. Kawasaki, D.B. Santos, T.G. Langdon, Processing a twinning-induced plasticity steel by high-pressure torsion, Scr. Mater., vol. 67, pp. 649-652, 2012.

[67] H.J. Jeong, E.Y. Yoon, D.J. Lee, N.J. Kim, S. Lee, H.S. Kim, Nanoindentation analysis for local properties of ultrafine grained copper processed by high pressure torsion, Journal of Materials Science, vol. 47, pp. 7828-7834, 2012.

[68] Z. Hegedűs, J. Gubicza, M. Kawasaki, N.Q. Chinh, J.L. Lábár, T.G. Langdon, Stability of the ultrafine-grained microstructure in silver processed by ECAP and HPT, Journal of Materials Science, vol. 48, pp. 4637-4645, 2013.

[69] M. Nakai, M. Niinomi, J. Hieda, H. Yilmazer, Y. Todaka, Heterogeneous grain refinement of biomedical Ti–29Nb–13Ta–4.6Zr alloy through high-pressure torsion, Scientia Iranica, vol. 20, pp. 1067-1070, 2013.

[70] J.Y. Kang, J.G. Kim, H.W. Park, H.S. Kim, Multiscale architectured materials with composition and grain size gradients manufactured using high-pressure torsion, Scientific reports, vol. 6, pp. 26590, 2016.

[71] R.B. Figueiredo, G.C. de Faria, P.R. Cetlin, T.G. Langdon, Three-dimensional analysis of plastic flow during high-pressure torsion, Journal of Materials Science, vol. 48, pp. 4524-4532, 2013.

[72] R.B. Figueiredo, M.T.P. Aguilar, P.R. Cetlin, T.G. Langdon, Analysis of plastic flow during high-pressure torsion, Journal of Materials Science, vol. 47, pp. 7807-7814, 2012.

Chapter 8. Conclusions, Summary and Future Work

8.1 Summary

This thesis provides a comprehensive study of the phase and microstructural evolution in selected γ-based Ti-Al alloys under extreme conditions by the use of advanced characterization techniques. *In-situ* experiments were conducted using high-energy diffraction techniques in synchrotrons, advanced neutron diffraction techniques and high-temperature laser-scanning confocal microscopy. In addition, high-pressure torsion techniques were used to impose severe plastic deformation with a view to decrease the grain size.

8.2 Conclusions

The main outcomes of this study are:

(1) New perspectives have been gained of the phase and microstructural changes of a single lamellar colony during heat treatment;
(2) The equilibrium α-transus temperature of a Ti-45Al-7.5Nb-0.5C alloy has been determined;
(3) The influence of high hydrostatic pressure on microstructural development in selected alloys has been determined;
(4) The influence of severe plastic deformation through the application of high pressure torsion has been determined.

In Chapter 4, details of the lamellar structure in Ti-Al alloys and the phase evolution during selected heat treatments of single crystals of a Ti-Al (polysynthetically twinned, PST crystals) alloy have been revealed. For the first time, *in-situ* neutron diffraction techniques were used

to study the structure of PST crystals. By the aid of supporting detailed EBSD studies, accurate arrangements of γ-variants were determined: in each lath of a PST crystal, each γ-subset contains three equivalent γ-variants. When the temperature is increased to 1648 K, well above the α-transus, a short-range-order atomic structure persisted in the single α-phase. The following sequence of events is suggested based on the experimental findings:

- Upon heating, a single lamellar colony (α_2 + γ) transforms into a single grain of the α-phase with a short-range-order structure.
- Upon holding at this temperature, new α-grains form, presumably by recrystallization due to initial lattice distortions.
- On subsequent cooling, the γ-phase nucleates on prior α-grain boundaries.
- Upon further cooling, an eutectoid reaction occurs, forming a fully lamellar structure (α_2 + γ) with both phases having an ordered crystal structure.

The outcomes of a microstructural investigation of an industrially important γ-based Ti-Al poly-crystalline alloy with composition Ti-45Al-7.5Nb-0.5C are presented in Chapter 5. *In-situ* observations in a high-temperature laser-scanning confocal microscope were combined with a differential analysis technique within the microscope so that bulk behavior could be determined at the same time as observations are made on the specimen surface. By this newly developed experimental technique, it was possible to study the effect of undercooling on nucleation events:

- Increased undercooling led to a significant reduction in grain size. Cooling rates between 25 K/min to 400 K/min led to a decrease in grain size from 174 to 129 μm in a Ti-45Al-7.5Nb-0.5C alloy.
- In addition, the α-transus temperature in this alloy was determined above 1520 K.

The outcomes of an *in-situ,* high-energy X-ray study and an energy-dispersive synchrotron study devoted to the analysis of lattice strain evolution in a Ti-45Al-7.5Nb-0.5/0.25C alloy under atmospheric pressure and high pressure are reported in Chapter 6.

- The total lattice strain of the Ti-45Al-7.5Nb-0.5C alloy under atmospheric pressure is semi-quantitatively attributed to three main factors based on Rietveld analysis: thermal expansion, the aluminum content of the respective phases and the extent to which the respective phases are ordered.
- Lattice strain development at high temperature and under high pressure of a similar γ-based Ti-Al alloy with composition a Ti-45Al-7.5Nb-0.25C is compared to that of the Ti-45Al-7.5Nb-0.5C alloy.
- Pressure has been identified as a fourth factor determining lattice strain evolution.
- The ($\alpha_2/\alpha + \gamma + \beta$) three-phase field is stable over a wide range of temperature (about 1350-1500 K) under conditions of high hydrostatic pressure.

These findings are important because it is now possible to predict, minimize and control inter-granular stresses in the industrial manufacturing of these γ-based Ti-Al alloys and hence, to enhance their mechanical properties.

Outcomes of a study for the influence of severe plastic deformation, imposed by a high pressure torsion technique, on the microstructural development of a Ti-45Al-7.5Nb alloy are reported in Chapter 7.

- The role of high compressive pressure (6 GPa) and torsion (10 turns) on the phase and microstructural evolution was investigated by *in-situ* neutron scattering and X-ray diffraction techniques.

- The high-pressure torsionally-induced shear strain is much larger at the surface of a thin disk-shaped specimen than at the median layer due to the presence of shear zones with swirls and vortices produced by HPT.
- As a consequence, the sequence of mechanically induced phase transformations at the surface is: $(\alpha_2 + \gamma) \rightarrow (\alpha + \gamma) \rightarrow \alpha$. This sequence of events is not fully realized at the median layer of the thin disk.
- An order-disorder transition occurs during high-pressure torsional deformation.
- These results cast light on the controversies in the literature with respect to phase transitions under conditions of severe plastic deformation. The exact nature of these events evidently depends on where on (or in) the specimen the phase fraction is determined.
- The bulk X-ray coherent crystallite size of the alloy is refined to 34 nm.
- Following high-pressure torsion processing, a (110) type of fiber texture is formed in the γ-phase and the hardness is increased form 308 H_v to a maximum of 605 H_v on the surface of the disk-shaped sample.
- High residual stresses remain in the room-temperature processed material with values close to the yield strength limit.

8.3 Future work

In this thesis, the phase transformation and microstructural evolution of γ-based Ti-Al alloys under high temperature, high pressure or HPT have been studied in detail. However, there are still a number of outstanding issues worthy of future study.

In Chapter 4, the HTLSCM and *in-situ* neutron experiments reveal the microstructural evolution of PST crystals, showing how a single colony becomes a multi-colony structure

during heat treatment. However, the mechanism of the thermal instability of the lamellar structure in PST crystals with the unstable composition Ti-47.5Al, has not been studied as yet. It is worth investigating the reasons for the instability of lamellar colonies in order to grow perfect large bulk of PST crystals.

In Chapter 6, an attempt was made to quantify the influence of the four factors (aluminium content, order parameter, pressure, and thermal coefficient) on lattice strain development. However, there are too many variants to enable a fully quantitative determination. It is suggested that in future, the energy-dispersive studies of the Ti-Al alloys be conducted with only high pressure as a variable, at a given temperature. Also, it would be useful to study Ti-Al alloys with different compositions. Such investigations will not only lead to a comprehensive equation of state, but also the development of a more complete phase diagram as a function of pressure.

In Chapter 7, we only focused on the homogeneity at different planes of Ti-45Al-7.5Nb disks processed by high pressure torsion along the thickness direction. It will be very interesting to study the phase changes in HPT treated Ti-45Al-7.5Nb disks, with HEXRD in order to obtain higher spatial resolution and to determine stresses, composition, order parameter and texture as a function of position. Whereas information is available to improve mechanical properties at room temperature, similar information at high temperature is lacking and *in-situ* heating experiments would be attractive.

Appendices

Appendix 1

The concept of an order-parameter was introduced by Bragg and William [1]. They defined an order parameter S as follows:

$$S = \frac{p-r}{1-r} \qquad \text{Eq. (A.1)}$$

where p is the probability that an atom resides in an ordered position r. For example, if an aluminium atom remains in its ordered position (the red sites depicted in Figure A.1) and no other atoms occupy these positions, the value of p is 1. r is the fraction of aluminium atoms residing in a fully ordered lattice. The structure of a fully ordered lattice α_2-Ti_3Al is shown in Figure A.1. Aluminium atoms occupy 25% of the lattice positions, which means that r has a value of 0.25.

The order-disorder transition refers to the case where aluminium and titanium atoms in the crystal lattice randomly interchange anti-sites. For example, titanium atoms have the possibility of residing in red positions.

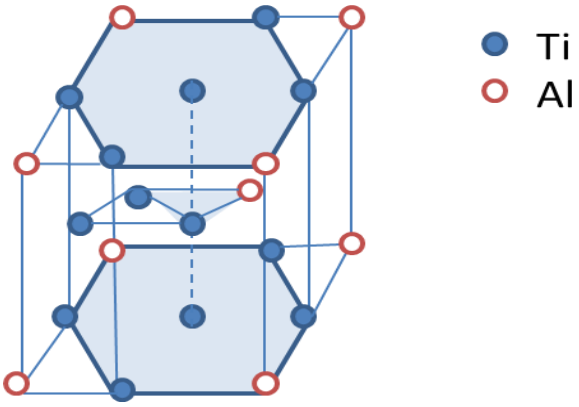

Figure A.1 The structure of ordered lattice α_2 phase (Ti_3Al)

Figure A.2 shows the order parameter (S) for the α_2/α-phase, calculated from the site occupancies reported by Yeoh *et al*. [2] (without taking into account the change in aluminium concentration). The sharp decrease in order parameter coincides with the sudden change in the lattice strain shown in Figure 6.5. This observation indicates that a higher *c*/*a* ratio reflects a more ordered structure. It is instructive to compare the occurrence of this sudden change in order parameter to changes in the *c*/*a*-ratio of the α_2/α-phase as a function of temperature, as shown in Figure A.3. The order parameter changes in the same fashion as the *c*/*a* ratio in the α_2/α-phase and hence, it seems reasonable to use the *c*/*a* ratio as a measure of the degree to which the α_2/α-phase is ordered.

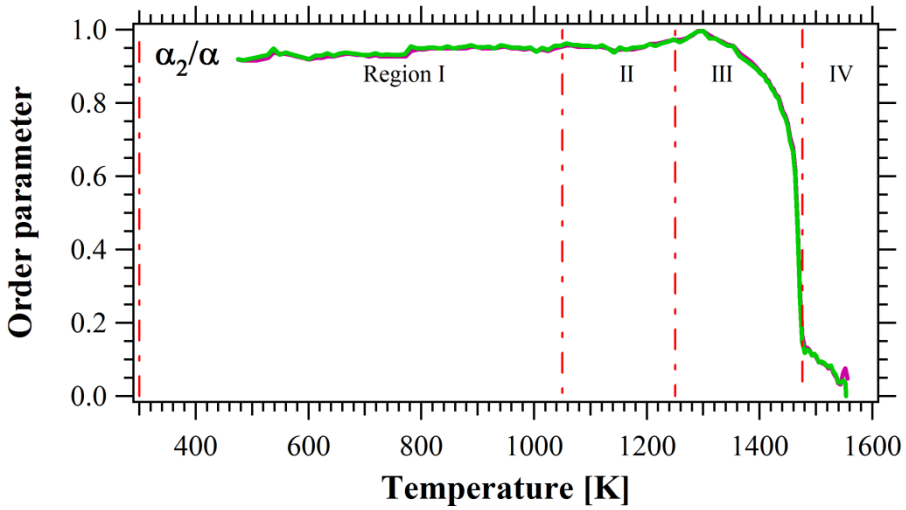

Figure A.2 The order parameter S for the α_2/α-phase at atmospheric pressure [2].

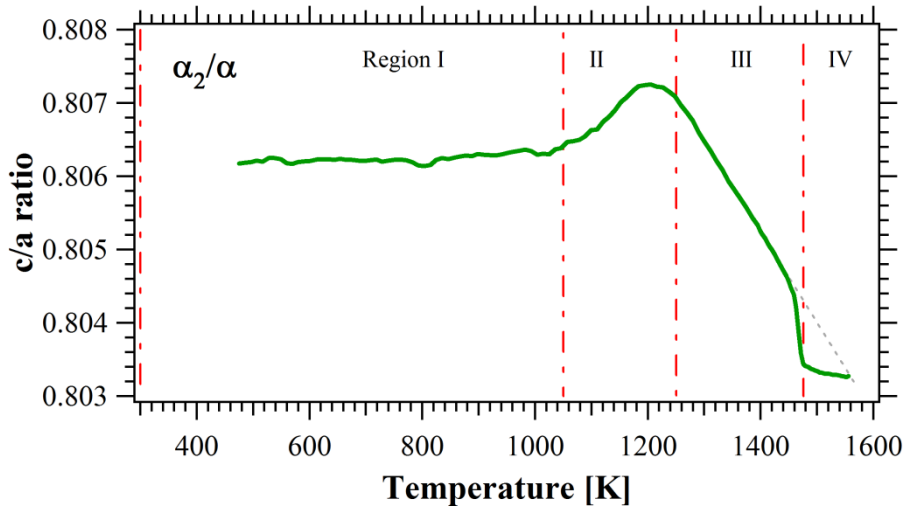

Figure A.3 The *c*/*a* ratio of the α_2/α-phase for a Ti-45Al-7.5Nb-0.5C alloy at atmospheric pressure [2].

Reference

[1] W.L. Bragg, and E.J. Williams, The effect of thermal agitation on atomic arrangement in alloys. Proceedings of the Royal Society of London. Series A, Containing Papers of a Mathematical and Physical Character, vol. 145, pp. 699-730,1934.

[2] L.A. Yeoh, et al., In situ high-energy X-ray diffraction study and quantitative phase analysis in the α+ γ phase field of titanium aluminides. Scripta Materialia, vol. 57, pp. 1145-1148, 2007.

Appendix 2: List of publications

[1] **X. Li**, R. Dippenaar, A. Shiro, T. Shobu, Y. Higo, M. Reid, H. Suzuki, K. Akita, K. I. Funakoshi, K.-D. Liss, "Lattice parameter evolution during heating of Ti-45Al-7.5Nb-0.25/0.5C alloys under atmospheric and high pressures" Intermetallics, vol. 102, pp. 120-131, 2018.

[2] **X. Li**, R. J. Dippenaar, J.-K. Han, M. Kawasaki, and K.-D. Liss, "Phase transformation and structure evolution of a Ti-45Al-7.5Nb alloy processed by high-pressure torsion," Journal of Alloys and Compounds, vol. 787, pp. 1149-1157, 2019.

[3] C. Shen, K.-D. Liss, M. Reid, Z. Pan, Y. Ma, **X. Li,** H. Li "In-situ neutron diffraction characterization on the phase evolution of γ-TiAl alloy fabricated during the wire-arc additive manufacturing process" Journal of Alloys and Compounds, vol 778, pp. 280-287, 2019

[4] J.-K. Han, **X. Li**, R. Dippenaar, K.-D. Liss, and M. Kawasaki, "Microscopic plastic response in a bulk nano-structured TiAl intermetallic compound processed by high-pressure torsion," Materials Science and Engineering: A, vol. 714, pp. 84-92, 2018.

[5] Z. Lu, **X. Li**, and L. Zhang, "Thermodynamic Description of Al-Si-Mg-Ce Quaternary System in Al-Rich Corner and Its Experimental Validation," Journal of Phase Equilibria and Diffusion, vol. 39, pp. 57-67, 2018.

[6] C. Shen, K.-D. Liss, Z. Pan, Z. Wang, **X. Li**, and H. Li, "Thermal cycling of Fe3Al based iron aluminide during the wire-arc additive manufacturing process: An in-situ neutron diffraction study," Intermetallics, vol. 92, pp. 101-107, 2018.

Appendix 3: Awards

[1] International Postgraduate Tuition Award (IPTA), 2014-2018, University of Wollongong;

[2] China Scholarship Council (CSC), 2014-2018;

[3] ANSTO Top-up Scholarship, 2016-2018;

[4] Matching Scholarship, 2018, University of Wollongong.